Gate reflectometry as readout and spectroscopy tool for silicon spin qubits

Rami Ezzouch

THÈSE

Pour obtenir le grade de

DOCTEUR DE L'UNIVERSITÉ GRENOBLE ALPES

Spécialité : NANOPHYSIQUE

Arrêté ministériel : 25 mai 2016

Présentée par

Rami EZZOUCH

Thèse dirigée par **Silvano DE FRANCESCHI**

préparée au sein du **Laboratoire PHotonique, ELectronique et Ingéniérie QuantiqueS**
dans **l'École Doctorale Physique**

Réflectométrie de grille comme outil de lecture et de spectroscopie pour les qubits de spin en silicium

Gate reflectometry as readout and spectroscopy tool for silicon spin qubits

Thèse soutenue publiquement le **9 juin 2021**,
devant le jury composé de :

Monsieur Silvano DE FRANCESCHI
DIRECTEUR DE RECHERCHE, CEA Grenoble, Directeur de thèse
Monsieur Takis Kontos
DIRECTEUR DE RECHERCHE, Laboratoire Pierre Aigrain, Ecole Normale Supérieure, Rapporteur
Monsieur John Julian Larrarte Morton
PROFESSEUR, London Centre for Nanotechnology, UCL, Rapporteur
Monsieur Pasquale Scarlino
DIRECTEUR DE RECHERCHE, Hybrid Quantum Circuits Laboratory, Institute of Physics, EPFL Lausanne, Examinateur
Monsieur Xavier Waintal
DIRECTEUR DE RECHERCHE, IRIG/DEPHY/PHELIQS/GT, CEA Grenoble, Examinateur
Monsieur Hervé Courtois
PROFESSEUR, Quantum Nano-Electronics and Spectroscopy, Institut Néel, Président

To my parents, the central pillar of my success.
To my family, who have always been there for me.
To my darling, who borne with me the weight of this thesis.
To my friends, who shared laughter and sorrow.
To anyone who contributed in shaping the person I am today.

Abstract

Owing to ever increasing gate fidelities and to a potential transferability to industrial CMOS technology, silicon spin qubits have become a compelling option in the strive for quantum computation. However, hole spin qubits in silicon remain a barely explored hosting platform as compared to their electron counterpart. Hole spins carry some attractive properties: for instance, strong spin-orbit coupling enables fast coherent spin rotations using a radio-frequency electric field; also, we expect long coherence times due to the absence of contact hyperfine interaction. In this thesis, we conduct experiments on p-type silicon-nanowire devices to take advantage of the above mentioned properties.

In order to pave the way for large-scale quantum processors, the development of scalable qubit readout schemes involving a minimal device overhead is a compelling step. Here we report the implementation of gate-coupled RF reflectometry for the dispersive readout of a fully functional hole spin qubit device. We use a p-type double-gate transistor made using industry-standard silicon technology. The first gate confines a hole quantum dot encoding the spin qubit, the second one a helper dot enabling readout. The qubit state is measured through the phase response of a lumped-element resonator to spin-selective interdot tunneling. The demonstrated qubit readout scheme requires no coupling to a Fermi reservoir, thereby offering a compact and potentially scalable solution whose operation may be extended above 1 K.

In a scalable architecture, each spin qubit will have to be finely tuned and its operating conditions accurately determined. In this prospect, spectroscopic tools compatible with a scalable device layout are of primary importance. Here we report a two-tone spectroscopy technique providing access to the spin-dependent energy-level spectrum of a hole double quantum dot defined in a split-gate silicon device. A first GHz-frequency tone drives electric-dipole spin resonance enabled by the valence-band spin-orbit coupling. A second lower-frequency tone (≈ 500 MHz) allows for dispersive readout via rf-gate reflectometry. We compare the measured dispersive response to the linear response calculated in an extended Jaynes-Cummings model and we obtain characteristic parameters such as g-factors and tunnel/spin-orbit couplings for both even and odd occupation.

Résumé

En raison de la fidélité croissante des grilles et de la transférabilité potentielle à la technologie CMOS industrielle, les qubits de spin en silicium sont devenus une option incontournable dans la course pour le calcul quantique. Cependant, les qubits de spin de trous dans le silicium reste une plate-forme d'hébergement à peine explorée par rapport à leurs homologues d'électrons. Les spins de trous ont des propriétés intéressantes : par exemple, un fort couplage spin-orbite permet des rotations de spin cohérentes rapides en utilisant un champ électrique radiofréquence ; aussi, on s'attend à de longs temps de cohérence dus à l'absence d'interaction hyperfine de contact. Dans cette thèse, nous menons des expériences sur des dispositifs à nanofils de silicium de type p pour tirer parti des propriétés mentionnés ci-dessus.

Afin d'ouvrir la voie à des processeurs quantiques à grande échelle, le développement de schémas de lecture de qubit évolutifs impliquant une surcharge minimale du dispositif est une étape convaincante. Nous rapportons ici la mise en œuvre de la réflectométrie RF couplée par grille pour la lecture dispersive d'un dispositif de qubit de spin de trou entièrement fonctionnel. Nous utilisons un transistor à double grille de type p fabriqué à l'aide de la technologie silicium au standard industriel. La première grille confine un ilot quantique de trou codant le qubit de spin, la seconde un ilot auxiliaire permettant la lecture. L'état du qubit est mesuré par la réponse de phase d'un résonateur à éléments localisés à un effet tunnel interdot sélectif en spin. Le schéma de lecture de qubit démontré ne nécessite aucun couplage à un réservoir de Fermi, offrant ainsi une solution compacte et potentiellement évolutive dont le fonctionnement peut être étendu au-dessus de 1 K.

Dans une architecture évolutive, chaque qubit de spin devra être finement réglé et ses conditions de fonctionnement déterminées avec précision. Dans cette perspective, les outils spectroscopiques compatibles avec une disposition évolutive des appareils sont d'une importance primordiale. Nous rapportons ici une technique de spectroscopie à deux tons donnant accès au spectre de niveau d'énergie dépendant du spin d'un double ilot quantique à trous défini dans un dispositif de silicium à grille divisée. Une première tonalité de fréquence GHz entraîne la résonance de spin dipolaire électrique activée par le couplage spin-orbite en bande de valence. Une deuxième tonalité de fréquence inférieure ($\approx 500\,\mathrm{MHz}$) permet une lecture dispersive via la réflectométrie à grille RF. Nous comparons la réponse dispersive mesurée à la réponse linéaire calculée dans un modèle Jaynes-Cummings étendu et nous obtenons des paramètres caractéristiques tels que les facteurs g et les couplages tunnel/spin-orbite pour une occupation paire et impaire.

Acknowledgements

Many would say that a Ph.D. thesis is a wild ride, but in my case, it was a smooth journey. This was possible thanks to the efforts of a surrounding team, always present in the moment of need to whom, I will forever be grateful.

I would like first to thank my advisor Dr. Silvano De Franceschi. Not only he enabled me in the pursuit of subjects in which I found great interest, he always took the time to gently explain the ambiguous concepts and to answer my questions (sometimes stupid I recall) while carefully respecting my autonomous character. Benefiting from his experience and deep understanding of physics was really a privilege for me.

A special thank goes also to Dr. Romain Maurand and Dr. Alessandro Crippa for supervising me. They took me under their wings, made me familiar with the complex experimental setup and borne high doses of my foolish errors. I enjoyed our discussions, debates, and arguments about the experimental results interpretation and physics concepts. Romain has a special gift vulgarising complex concepts that I much appreciated and leaned on so often. I learned so much from him.

From time to time, I was assisted by Dr. Xavier Jehl, a great experimentalist whose feedback I always relished. Many thanks for his help.

I had the chance during the last year of my Ph.D. thesis to work with Dr. Simon Zihlmann. I was extremely pleased by this partnership. Thank you Simon for helping me with Triton experiments.

It goes without saying that without the LETI devices and the constant effort of the LETI team in making them better by the day, this thesis would have not been possible. I am much obliged for them and for anyone that contributed in developing and improving the samples I used.

I want to thank Dr. Xavier Waintal for his help with the development of the Video Mode measurement technique and the post-processing of its results. His ideas shaped the post-processing algorithms and made them very efficient.

The list of people to acknowledge is long, specially if I want to include all the members of the LATEQS team. I am deeply grateful to each one of you for the time we had together the last four years. Thanks to anyone who contributed to this Ph.D. thesis and I failed to mention.

A special thought goes to Marc Sanquer, the godfather of the quantum silicon project in Grenoble, who recently left us. He always greeted me with a big smile and happily answered my questions. Rest in peace and may god have mercy on your soul.

In the end, I am grateful for the members of the jury for taking the time to carefully review this work and attending my Ph.D. defence.

Contents

List of Figures

List of Tables

Acronyms

QD quantum dot
DQD double quantum dot
ICT interdot charge transition
VM video mode
CVM coarse video mode
CMOS complementary metal oxide semiconductor
SOI silicon-on-insulator
NW-FET nanowire field-effect transistor
RF radio frequency
QPC quantum point contact
SET single electron transistor
SHT single hole transistor
ZI Zurich Instruments
UHF-LI ultra high frequency lock-in
SNR signal to noise ratio
FFT fast Fourier transform
DTR data transfer rate
DBSCAN density-based spatial clustering of applications with noise
FWHM full width at half maximum
RAM random access memory
MOSFET metal-oxide-semiconductor field-effect transistor
2DEG two dimensional electron gas
PSB Pauli spin bloackade
EDSR electric dipole spin resonance
ESR electron spin resonance
g-TMR g-tensor magnetic resonance
IZ-EDSR iso-Zeeman electric dipole spin resonance (EDSR)
DAC digital analog converter
PCB printed circuit board
AWG arbitrary wave generator
DMM digital multi-meter
NPLC number of power line cycles
SEM scanning electron micrograph

Introduction

I used to wonder how it comes about that the electron is negative. Negative-positive, these are perfectly symmetric in physics. There is no reason whatever to prefer one to the other. Then why is the electron negative? I thought about this for a long time and at last all I could think was "It won the fight!"

Albert EINSTEIN

Contents

Quantum computing is attracting a great deal of interest, as we are reaching the limits in progress of transistor-based processors and is regarded as the Holy Grail of quantum technologies. With the end of Moore's law approaching, quantum computing has emerged as one of the most prominent post-Moore paradigms raising the interest of top microelectronic firms toward exploring new computing paradigms. By relying on the use of some specific properties of quantum systems, one could make an unusual type of a processing unit, a quantum processor. Even though research and applications of quantum computing are still in their infancy, the promises of this revolutionary computing concept have recently led to the rapid growth of governmental and private funding in this emerging field.

0.1 Quantum computing

The concept of a quantum computer was proposed in the beginning of the eighties and it has been since a subject of studies. In a famous speech, Richard Feynman argued [36] that quantum phenomena as chemical reactions could be better simulated by means of quantum processors. Since then, quantum computation has been an active area of research. However, it was only in 1994 that Peter Shor gave [126] a proposition of an algorithm enabling to factorize a large integer, way bigger than those affordable by the most powerful computing unit

on earth, using a quantum computer. This application may seem as a minor application to quantum computing but it has heavy consequences as most of cryptography systems rely on integer factorization and the inability of a mere computer to factorize a large integer.

Quantum technologies rely on the fundamental principles of superposition and entanglement. These aspects of quantum mechanics have so far been exploited in areas such as metrology and magnetometry. Nevertheless, their applications remain at the basic level and their full potential is yet demonstrated. The road toward quantum computing is a long one and it involves many milestones whose achievement is conditioned to the level of control and maturity of the unit cells forming a quantum processor. Fig. 0.1 shows an expected timeline of quantum technologies detailing the main underlying phases and steps.

Major firms around the world, noticed the significant progress at the research level in this field and started to invest on quantum technology since few years. For instance, Lockheed Martin created two research centers in collaboration with the University of South California and the University of Maryland, IBM is conducting research on quantum computing as well as on low temperature superconducting electronics, Microsoft created its Station-Q laboratory and went on the path of topological quantum computing, Google stepped into the game by investing on the X-mon superconducting qubit concept, and Intel signed a 10-year partnership with Qutech aiming to foster advance in both semiconductor- and superconductor-based quantum computing.

Quantum bits, also commonly referred to as qubits, are the elementary building blocks of a quantum computer. They can be seen as the quantum analog of classical bits. Their physical realizations can be regarded as the quantum counterparts of conventional transistors. A field-effect transistor an be either "ON" (*i.e.* conducting) or "OFF" (*i.e.* insulating), thereby offering a natural physical realization of digital logic. In contrast to that, a qubit can be simultaneously in a quantum superposition of its two basis states, say $|0\rangle$ and $|1\rangle$. Fig. 0.2 shows the geometric representation of a qubit state, which can be written in the following form:

$$|\psi\rangle = \cos\frac{\theta}{2}|0\rangle + e^{i\varphi}\sin\frac{\theta}{2}|1\rangle \tag{1}$$

with $\cos^2\theta/2$ and $\sin^2\theta/2$ the probabilities of finding the states $|0\rangle$ and $|1\rangle$, respectively, and φ a phase parameter.

A system of two qubits would be represented by a linear superposition of four states: $|00\rangle$, $|10\rangle$, $|01\rangle$ and $|11\rangle$, and in general, a system of N qubits would result in a superposition of 2^N states. This gives rise to a naturally built-in parallelism that could be implemented to reach exceptional computational powers well beyond those of the most powerful classical computer.

Due to interactions with the external environment, a quantum system will be subject to noise and thus decoherence. This translates into a characteristic time scale on which a quantum system can retain a given coherent superposition of states. Thus, a distinction should be made between physical qubits (faulty implementation) and a logical qubits (faultless). The latter, which is the one used to estimate the computing power of a quantum processor, requires a combination of a certain number of physical qubits depending on their fidelity, *i.e.* how accurate they are. The higher the individual fidelity, the less physical qubits are needed to form a logical qubit. With error rates of 0.1 % on physical qubits, a single logical qubit requires thousands of physical qubits [38]. The realization of a fault-less computation is theoretically possible thanks to quantum error correction algorithms, *e.g.* in the so-called surface codes [38, 140, 3].

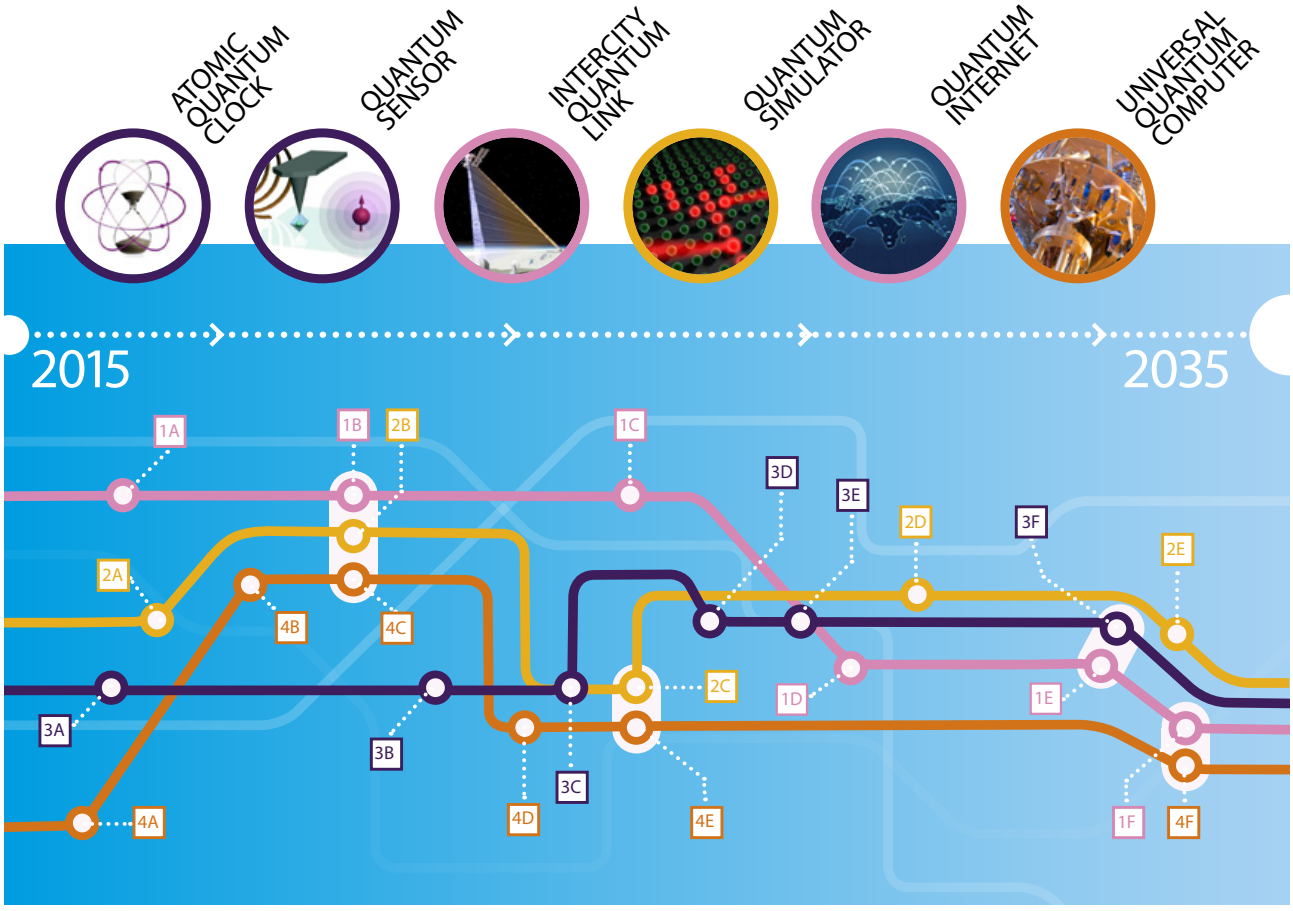

1. Communication | 2. Simulators | 3. Sensors | 4. Computers

0 – 5 years

- A Core technology of quantum repeaters
- B Secure point-to-point quantum links

- A Simulator of motion of electrons in materials
- B New algorithms for quantum simulators and networks

- A Quantum sensors for niche applications (incl. gravity and magnetic sensors for health care, geosurvey and security)
- B More precise atomic clocks for synchronisation of future smart networks, incl. energy grids

- A Operation of a logical qubit protected by error correction or topologically
- B New algorithms for quantum computers
- C Small quantum processor executing technologically relevant algorithms

5 – 10 years

- C Quantum networks between distant cities
- D Quantum credit cards

- C Development and design of new complex materials
- D Versatile simulator of quantum magnetism and electricity

- C Quantum sensors for larger volume applications including automotive, construction
- D Handheld quantum navigation devices

- D Solving chemistry and materials science problems with special purpose quantum computer > 100 physical qubit

> 10 years

- E Quantum repeaters with cryptography and eavesdropping detection
- F Secure Europe-wide internet merging quantum and classical communication

- E Simulators of quantum dynamics and chemical reaction mechanisms to support drug design

- E Gravity imaging devices based on gravity sensors
- F Integrate quantum sensors with consumer applications including mobile devices

- E Integration of quantum circuit and cryogenic classical control hardware
- F General purpose quantum computers exceed computational power of classical computers

Figure 0.1 – **Quantum technologies timeline and future prospects.** Taken from [24].

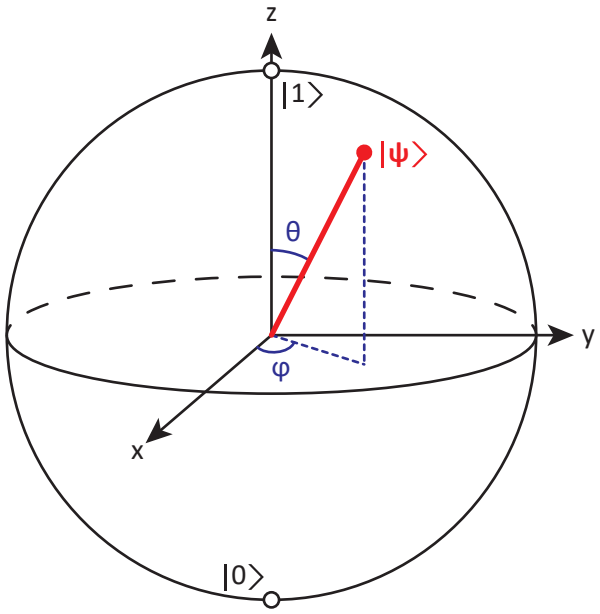

Figure 0.2 – **Bloch sphere representation of a qubit state.** The qubit quantum state $|\psi\rangle$ could take any value on the Bloch sphere as a result of the superposition of $|0\rangle$ and $|1\rangle$ states. It is characterized by the spherical parameters θ and φ.

Seeing the important number of physical qubits necessary for a functioning quantum processor, scaling, one of the DiVincenzo criteria [30], takes a fundamental place in the conception of qubit platforms. Implementations of qubits vary and one can find a multitude of physical platforms, *e.g.* superconducting qubits [21], trapped ions [10], photonic qubits [74] and semiconductor qubits [18]. And despite the fact that no clear implementation is yet to be universally adopted as the most suitable for a quantum computer, there is a growing attention towards silicon-based spin qubits which is motivated by the large-scale manufacturing capabilities of the semiconductor industry.

0.2 Semiconductor qubits

Semiconductor qubits offer a distinctive potential for high density integration on a large scale originating from the mature nanofabrication technologies of the semiconductor industry. They span from systems operated in dilutions fridges at millikelvin temperatures to ones fully functional at room temperature. A few major implementations can be cited, namely, color centers [63], shallow dopants [114], and gate-defined quantum dots [112, 69].

Single spins localized in gate defined quantum dots have been recognized as a promising platform for quantum computation early on [84] and the recent years have witnessed remarkable progress in their development [112, 79, 31, 146]. While it is possible to use the charge degree of freedom to encode quantum information, a charge qubit is highly affected by electrical noise, making it fall short to achieve the required high coherence levels and unlikely to be considered as a state encoding.

In a seminal proposal [84], Loss and DiVincenzo put forward the idea of using the spin of localized electrons as the physical system encoding an elementary bit of quantum information. As a physical realization, these authors referred to gate-defined quantum dots hosting individ-

ual electrons. Along a similar idea, Kane proposed [67] a qubit implementation in silicon based on the nuclear spins of phosphorous dopants. The first spin qubits were realized in quantum dots electrostatically defined in GaAs-based heterostructure embedding a high-mobility two-dimensional electron gas [75, 112]. Further experimental work, however, demonstrated that an electron spin in GaAs loses its coherence very fast (around 10 ns) due to the hyperfine coupling with the nuclear spins of the hosting crystal. This short coherence time has limited the development of GaAs spin qubits.

In contrast to GaAs, the most abundant isotope of silicon, ^{28}Si, has zero nuclear spin, resulting in no hyperfine interaction. Even though natural silicon hosts 4.7 % of the only stable isotope containing a non zero nuclear spin ^{29}Si, this percentage can be highly reduced by isotopic purification. The first silicon spin qubit was reported by a team of researchers at the University of South Wales in 2012 consisting of an electron spin bound to a phosphorous dopant [113]. Lately, there has been an increasing focus on silicon-based realizations [69, 89, 115, 130, 45].

Access to isotopically enriched ^{28}Si has enabled the achievement of very long spin coherence times for both nuclear and electron spins [137, 96, 152]. In addition, two-qubit gates with increasing high fidelities were demonstrated in electrostatically defined electron double quantum dots [138, 155, 145, 57]. Leveraging the well-established silicon technology may enable facing the scalability challenge, and initiatives to explore this opportunity are on the way including one led by the Quantum Silicon team in Grenoble [58].

0.3 Hole qubits

While further improvements in single- and two-qubit gates can be expected, growing research efforts are now being directed to the realization of scalable arrays of coupled qubits [136, 83, 65, 154, 135]. The steady evolution towards increasing the number of qubits has triggered the quest for a compact control and read-out architecture. Considering qubit control, all electrical qubit driving appears as a clear asset in dense quantum dot arrays.

A microwave excitation applied to a gate electrode drives Rabi oscillations of electron/hole pseudospins via the EDSR mechanism originating from intrinsic or artificial spin-orbit coupling. This has been shown in III-V semiconductors [103, 109] and in group IV semiconductors, such as silicon [69, 89, 152, 27, 26] and germanium [146, 51, 50, 52, 119, 40]. Other than the intrinsic mixing of the quantum-mechanical spin with the quantum orbital angular momentum (spin-orbit interaction), the p-type symmetry of the wave function frees the holes from the contact hyperfine interaction leaving only a generally weaker residual dipolar interaction [37].

Following some first experimental demonstrations of hole spin qubits in silicon [89, 27, 26], there is a strong need to characterize and explore these qubits. Not only do hole spin qubits allow for a dense integration of qubits [52] while preserving individual addressability [89, 81], but there is plenty of physics in the interplay of orbital and spin degree of freedom to be explored and understood.

0.4 Thesis outline

In Chap. 1, the theoretical background relevant to the experiments conducted during this thesis is introduced. Concepts such as quantum dots, spin to charge conversion, electric dipole spin resonance and reflectometry are discussed.
Chap. 2 presents the nanodevices used in the scope of this thesis as well as the underlying technologies and steps used to fabricate them. Additionally, it details the downstream procedures of fabrication taking place after the reception of the said samples.
The experimental setup that lead to this thesis results and its characterisation are put forward in Chap. 3. Our team's vision on how to implement the reflectometry readout on qubit devices can be captured in this part of the manuscript.
Chap. 4 retraces the steps of a recently published work [26] demonstrating gate-reflectometry dispersive readout and coherent control of a hole spin qubit in silicon.
In order to remedy the long acquisition times associated with reflectometry measurements that require high resolutions, Chap. 5 offers an approach to considerably reduce the dispersive measurements times by cutting back on communication times with the instruments while maintaining an acceptable noise and feature signal levels.
An other published work [35] that is presently at the reviewing phase is included in Chap. 6 where a two-tone microwave spectroscopy technique dispersively probed is carried out on silicon hole double quantum dot allowing its spectrum reconstruction.
This manuscript ends with a conclusion and an outlook on possible upcoming research that could benefit from the results of this thesis. It includes also a glimpse into a recently started experiment on a new generation of multi-gate qubit devices.

Takeaway messages:

- Quantum computing is a new paradigm based on the use of quantum mechanical properties of two-level quantum systems, namely the superposition of states and entanglement.
- The building block of a quantum processor is called a qubit, short for quantum bit, which is the quantum equivalent of the transistor in digital electronics.
- Silicon spin qubits offer a distinctive potential for high density integration leveraging the mature semiconductor industry and long coherence times.
- Holes in silicon allow for all electrical driving due to their intrinsic spin-orbit coupling. They do not suffer from the contact hyperfine interaction making their pseudospin state an attractive choice for quantum information encoding.

Chapter 1

Spin qubits: readout and manipulation

> The best that most of us can hope to achieve in physics is simply to misunderstand at a deeper level.
>
> Wolfgang PAULI

Contents

This chapter introduces the theoretical concepts necessary for the discussion of the experimental results presented further in this thesis. It provides an introductory level background while detailed aspects of the treated subjects could be found in the provided references throughout the chapter or in reviews [134, 47].

1.1 Quantum dots

1.1.1 Single quantum dots

Quantum dots (QDs) are man-made nanostructures that can be filled either with electrons or holes [47]. A dot is electrically connected to Fermi reservoirs through tunnel barriers so that

charges can be exchanged. It is also capacitively coupled to one or more gate electrodes acting on its electrostatic potential as shown in Fig. 1.1.

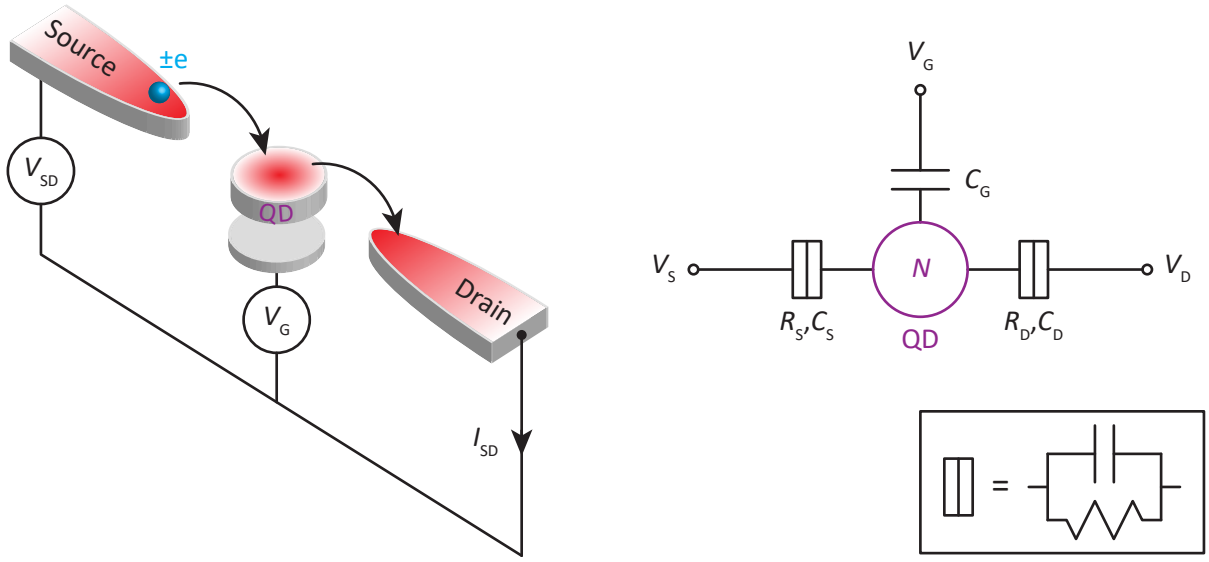

Figure 1.1 – **Simple schematic of a lateral geometry QD and equivalent network of tunnel resistors and capacitors.** The dot exchanges charges with the source and drain reservoirs through tunnel barriers, resulting in a current I_{SD} depending on the source-drain bias voltage V_{SD} and the gate voltage V_G.

QDs are dominated by two main effects:

— the Coulomb repulsion between holes/electrons leading to Coulomb blockade. Consequently, adding a hole/electron to the QD costs energy.

— the 3D confinement leading to quantum effects and a discrete energy spectrum.

In order to understand transport through a QD, we need first to briefly mention the constant interaction model [77] and adopt a simple representation of a single QD shown in Fig. 1.1. This latter is based on two assumptions. First, Coulomb interactions in the QD as well as the interactions between the charges in the dot and those in the environment are a function of a single constant capacitance $C = C_S + C_G + C_D$. Secondly, the energy level spectrum of the QD is independent of the number of charges in the dot.

Using this model, we can now introduce the total energy $U(N)$ of a QD with N holes/electrons in the ground state as:

$$U(N) = \frac{(\pm e(N - N_0) + C_S V_S + C_D V_D + C_G V_G)^2}{2C} + \sum_{n=1}^{N} E_n(B), \tag{1.1}$$

where e is the elementary charge, $N_0|e|$ is the charge in the dot compensating for the background charge made by the impurities in the structure, B is the applied magnetic field and $E_n(B)$ is the energy of an occupied level. The electrochemical potential $\mu(N)$ of the QD can be defined afterwards as:

$$\mu(N) \equiv U(N) - U(N-1). \tag{1.2}$$

At low-bias voltage (the potential difference between the source and the drain), charge transport is only possible whenever the electrochemical potential of the dot is inside the bias window, *i.e.* $\mu_S \geq \mu(N) \geq \mu_D$, where $\mu_{S(D)}$ is the electrochemical potential of the source (drain). Coulomb blockade occurs whenever this condition is not met and could be lifted by tweaking the electrochemical potential of the dot using the voltage applied to the gate electrode. Fig. 1.2 shows examples of level alignments and the expected current through the dot as a function of the gate voltage for a hole transport case. The magnitude of the observed current flowing through the QD depends on the tunnel rates between the source and the QD (Γ_S), and between the QD and the drain (Γ_D). The voltage difference between two consecutive peaks gives access to the energy value E_{add} necessary to add an electron to the dot also called addition energy:

$$E_{add}(N) = \mu(N+1) - \mu(N). \tag{1.3}$$

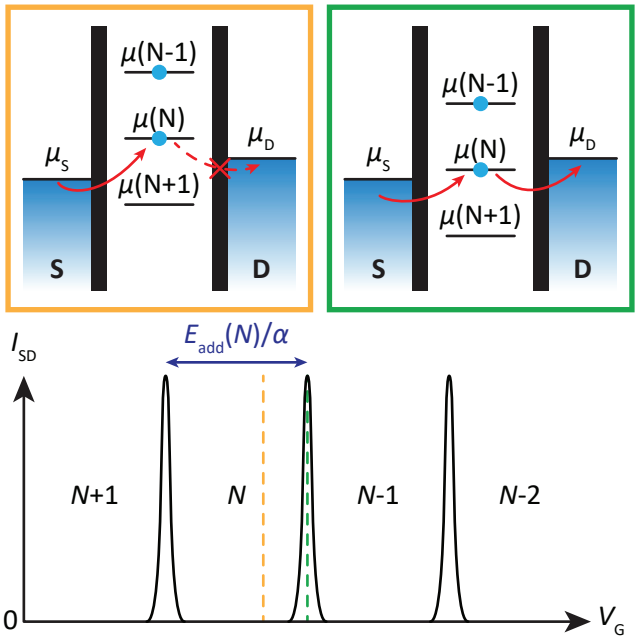

Figure 1.2 – **Transport and energy levels alignment of a hole QD in the low bias regime.** Qualitative plot of the current I_{SD} flowing through the QD as a function of the gate voltage V_G (bottom) and corresponding schematic diagrams of the electrochemical potentials at the marked gate voltages (top). The addition energy $E_{add}(N)$ is marked for the N^{th} transition and α stands for the lever-arm coupling of the gate to the dot.

In the case of a high bias regime, multiple energy levels may contribute to the charge tunneling. When V_{SD} is high enough to include excited states besides the ground state, the charge finds more than possible a path to tunnel through the dot leading therefore to a variation in the measured current allowing energy spectroscopy of the excited states [47].

1.1.2 Double quantum dots

The basic concepts introduced to discuss hole transport through a single QD can be applied to the more complex case of two QDs in series. A schematic representation of a lateral geometry double quantum dot (DQD) as well as an equivalent network of tunnel resistors and capacitors is given in Fig. 1.3.

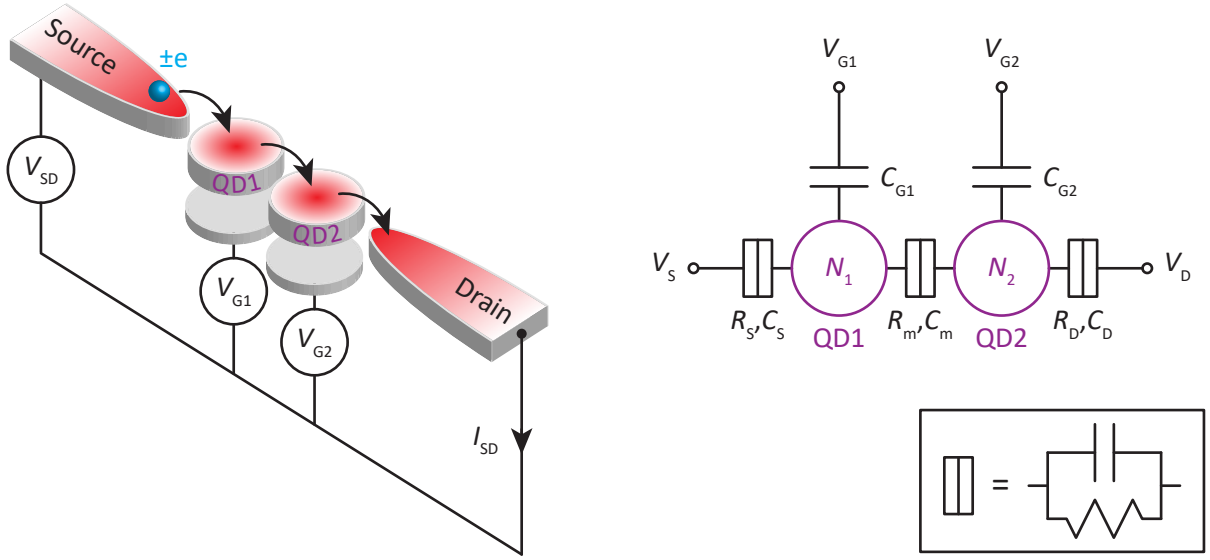

Figure 1.3 – **Simple schematic of a lateral geometry DQD and equivalent network of tunnel resistors and capacitors** The dots exchange charges mutually and with the source and drain reservoirs through tunnel barriers, creating a current I_{SD} depending on the source-drain bias voltage V_{SD} and the gates voltages V_{G1} and V_{G2}.

Using this representation and following the constant interaction model, the interactions for the first and the second QD are characterized respectively by the capacitances $C_1 = C_S + C_{G1} + C_m$ and $C_2 = C_m + C_{G1} + C_D$. The two dots are coupled to each other by a tunnel resistor R_m and a capacitor C_m. This latter coupling capacitance plays a major role on the shape of the stability diagram since the energy levels of a dot depend now on the number of charges on the other dot, hence the new definition of the electrochemical potentials:

$$\begin{aligned} \mu_1(N_1, N_2) &\equiv U_1(N_1, N_2) - U_1(N_1 - 1, N_2), \\ \mu_2(N_1, N_2) &\equiv U_2(N_1, N_2) - U_2(N_1, N_2 - 1), \end{aligned} \tag{1.4}$$

where the electrochemical potential $\mu_{1(2)}(N_1, N_2)$ is the energy necessary to add the $N^{th}_{1(2)}$ charge to QD1(2) while maintaining $N_{2(1)}$ charges on the other dot.

By marking the transitions corresponding to $\mu_1(N_1, N_2) = \mu_S$ (dot-lead), $\mu_2(N_1, N_2) = \mu_D$ (dot-lead) and $\mu_1(N_1, N_2) = \mu_2(N_1 - 1, N_2 + 1)$ (interdot charge transition (ICT)), and varying the dots fillings N_1 and N_2 as a function of gate voltages V_{G1} and V_{G2}, the stability diagram of a DQD can be established. Fig. 1.4 puts forward two schematic stability diagrams of a hole double quantum dot system with a moderate C_m in the case of no source-drain bias and in a low bias regime.

C_m shapes the dot-lead transitions slopes in a stability diagram. If $C_m \to 0$ (decoupled dots), the honeycomb pattern becomes a square pattern and ICTs vanish. In the opposite extreme case where the mutual capacitance becomes dominant ($C_m/C_{1(2)} \to 1$), the transitions to reservoirs merge into a single line and the distance between triple points is maximal. This results in a single dot behaviour.

If we start increasing the bias, as said previously, many energy levels can be contained in the bias window allowing the charge to have more than one possible path. This results in the

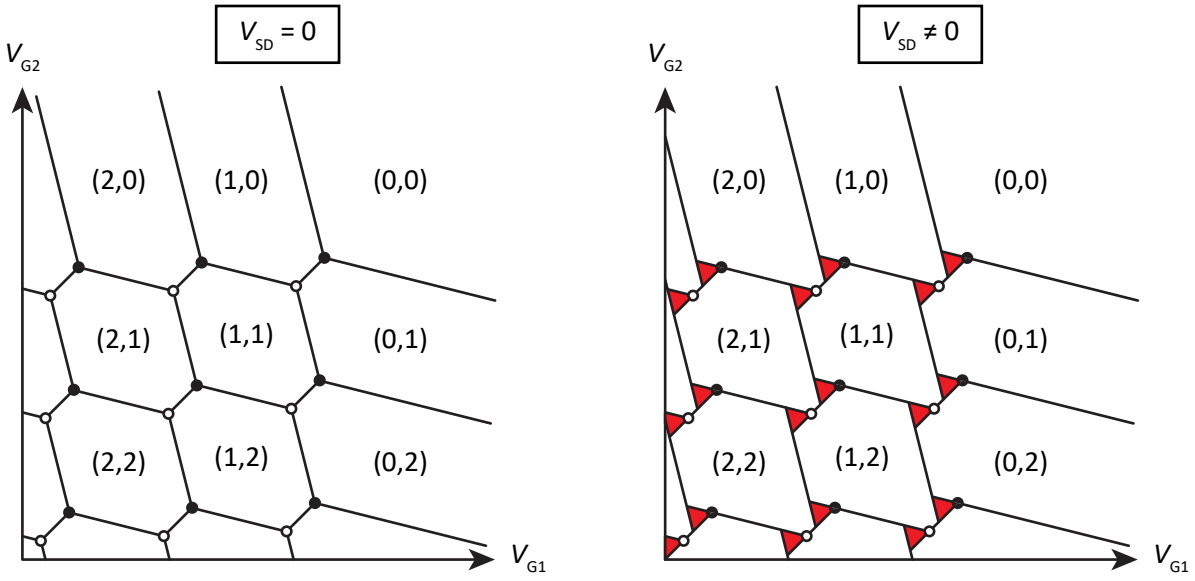

Figure 1.4 – **Schematic stability diagrams of a hole DQD system for different bias voltages.** In the zero bias case (left), lines with negative slopes mark dot-lead transitions, and those with positive slopes, ICTs. The boundaries of interdot lines are called triple points and are marked by ∘ (hole transfer process) and • (electron transfer process). In this case, current is present on the triple points. When the source drain voltage is nonzero (right), in addition to all previous elements, bias triangles form. In a series configuration, the source-drain current flows (and is measurable) only inside the bias triangles filled with red. (N_1, N_2) denotes the charge filling of the DQD where $N_{1(2)}$ is the number of holes present in QD1(2).

appearance of so-called bias triangles presented in the right panel of Fig. 1.4.

1.1.3 Spin states and energy diagram of a double quantum dot

Up until this point, we considered only the charge component of a hole/electron. And while this aspect could explain many experimental findings, it cannot capture the full picture since a hole/electron carries also a spin. As a result, dot-lead and interdot tunnelling events can be affected in certain spin configurations.

In pursuit of simplification, we always consider that pairs of holes occupy progressively the spin degenerate QD levels. As a result, the DQD system either carries a spin 1/2 if the charge configuration is odd (total number of charges present in the system is odd), or a spin 0 for an even charge configuration. Depending on this charge configuration, we present the spin states of the dots and their energy diagrams.

Odd charge configuration

If we consider a left (right) charge state $|\mathrm{L}\rangle$ ($|\mathrm{R}\rangle$) where the hole/electron is fully located on the left (right) QD, and at the same time, take into account the spin component of the particle (either $|\downarrow\rangle$ or $|\uparrow\rangle$), we end up with four energy states for the DQD: $|\mathrm{L}\downarrow\rangle$, $|\mathrm{L}\uparrow\rangle$, $|\mathrm{R}\downarrow\rangle$ and $|\mathrm{R}\uparrow\rangle$. In order to compute the energies of these, we adopt the following Hamiltonian:

$$\mathcal{H}_{\mathrm{odd}} = \mathcal{H}_0^{\mathrm{odd}} + \mathcal{H}_{\mathrm{SO}}^{\mathrm{odd}} + \mathcal{H}_{\mathrm{Z}}^{\mathrm{odd}}, \tag{1.5}$$

where $\mathcal{H}_0^{\mathrm{odd}}$ includes the tunnelling between states with same spin orientation, $\mathcal{H}_{\mathrm{SO}}^{\mathrm{odd}}$ the coupling between states with different spin and orbital components by cause of spin-orbit coupling and $\mathcal{H}_{\mathrm{Z}}^{\mathrm{odd}}$ the Zeeman splittings in the presence of an external magnetic field B. Using the charge and spin Pauli operators (τ and σ, respectively), the detailed expressions of these three terms are [97]:

$$\begin{aligned}\mathcal{H}_0^{\mathrm{odd}} &= \frac{\varepsilon}{2}\tau_z + t\tau_x \\ &= \frac{\varepsilon}{2}(|\mathrm{L}\downarrow\rangle\langle\mathrm{L}\downarrow| + |\mathrm{L}\uparrow\rangle\langle\mathrm{L}\uparrow| - |\mathrm{R}\downarrow\rangle\langle\mathrm{R}\downarrow| - |\mathrm{R}\uparrow\rangle\langle\mathrm{R}\uparrow|) \\ &+ t(|\mathrm{L}\downarrow\rangle\langle\mathrm{R}\downarrow| + |\mathrm{R}\downarrow\rangle\langle\mathrm{L}\downarrow| + |\mathrm{L}\uparrow\rangle\langle\mathrm{R}\uparrow| + |\mathrm{R}\uparrow\rangle\langle\mathrm{L}\uparrow|),\end{aligned} \tag{1.6}$$

$$\begin{aligned}\mathcal{H}_{\mathrm{SO}}^{\mathrm{odd}} &= t_{\mathrm{SO}}\tau_y\sigma_y \\ &= t_{\mathrm{SO}}(|\mathrm{L}\uparrow\rangle\langle\mathrm{R}\downarrow| + |\mathrm{R}\downarrow\rangle\langle\mathrm{L}\uparrow| - |\mathrm{L}\downarrow\rangle\langle\mathrm{R}\uparrow| - |\mathrm{R}\uparrow\rangle\langle\mathrm{L}\downarrow|),\end{aligned} \tag{1.7}$$

$$\begin{aligned}\mathcal{H}_{\mathrm{Z}}^{\mathrm{odd}} &= \frac{1}{2}g_{\mathrm{L/R}}\mu_{\mathrm{B}}B\sigma_z \\ &= \frac{1}{2}g_{\mathrm{L}}\mu_{\mathrm{B}}B(|\mathrm{L}\uparrow\rangle\langle\mathrm{L}\uparrow| - |\mathrm{L}\downarrow\rangle\langle\mathrm{L}\downarrow|) \\ &+ \frac{1}{2}g_{\mathrm{R}}\mu_{\mathrm{B}}B(|\mathrm{R}\uparrow\rangle\langle\mathrm{R}\uparrow| - |\mathrm{R}\downarrow\rangle\langle\mathrm{R}\downarrow|),\end{aligned} \tag{1.8}$$

where ε is the energy detuning between the two QDs, t the tunnel coupling, t_{SO} the spin-flip tunnel coupling due to spin-orbit coupling, $g_{\mathrm{L(R)}}$ the Landé g-factor of the left (right) dot and μ_{B} the Bohr magneton.

Putting together all the elements from Eqs. (1.5) to (1.8), we could write the matrix representation of the $\mathcal{H}_{\text{odd}}$ Hamiltonian:

$$\mathcal{H}_{\text{odd}} = \begin{pmatrix} \frac{\varepsilon}{2} - \frac{1}{2}g_{\text{L}}\mu_{\text{B}}B & 0 & t & -t_{\text{SO}} \\ 0 & \frac{\varepsilon}{2} + \frac{1}{2}g_{\text{L}}\mu_{\text{B}}B & t_{\text{SO}} & t \\ t & t_{\text{SO}} & -\frac{\varepsilon}{2} - \frac{1}{2}g_{\text{R}}\mu_{\text{B}}B & 0 \\ -t_{\text{SO}} & t & 0 & -\frac{\varepsilon}{2} + \frac{1}{2}g_{\text{R}}\mu_{\text{B}}B \end{pmatrix}. \tag{1.9}$$

By numerically solving the above Hamiltonian (Eq. (1.9)), we obtain the energies (eigenvalues of the Hamiltonian) as a function of detuning energy. Fig. 1.5 shows the simulation interface that allows us to have the energy diagram depending on t_{SO}, t, g_{L}, g_{R} and B parameters. These parameters are made into interactive sliders that allow for real time update of the energy levels.

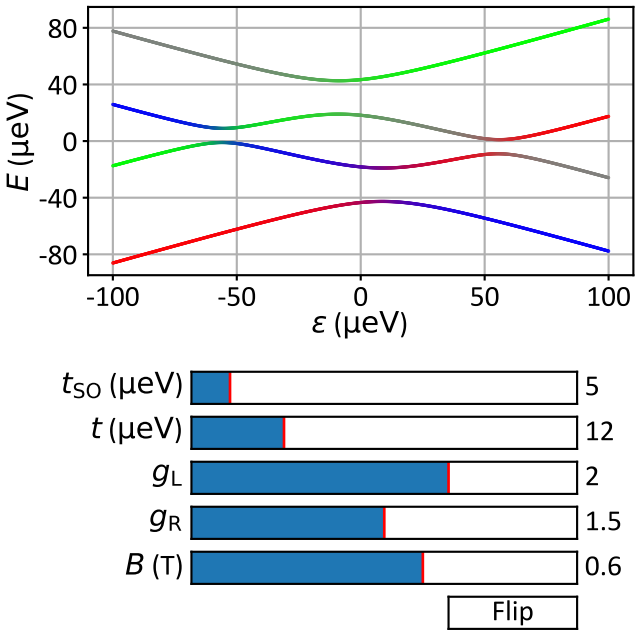

Figure 1.5 – **Energy diagram simulation of a DQD for an odd charge configuration.** At the bottom, the interactive sliders of the t_{SO}, t, g_{L}, g_{R} and B parameters allow for real time update of the energy levels.

The simulation python code is included in Appendix A.1. Just copy-paste and have fun!

Even charge configuration

The landscape of spin states in a DQD changes completely when dealing with an even charge configuration. Two holes in the same dot always form a spin singlet (total spin number $S = 0$) as the ground state in zero external magnetic field [47]. The following excited states are triplet states (total spin number $S = 1$) where one hole occupies a higher orbital. We find ourselves with five energy states:

$$\begin{cases} \text{S}(1,1) = \frac{1}{\sqrt{2}}(|\downarrow\uparrow\rangle - |\uparrow\downarrow\rangle) \\ \text{T}_{-}(1,1) = |\downarrow\downarrow\rangle \\ \text{T}_{0}(1,1) = \frac{1}{\sqrt{2}}(|\downarrow\uparrow\rangle + |\uparrow\downarrow\rangle) \\ \text{T}_{+}(1,1) = |\uparrow\uparrow\rangle \\ \text{S}(0,2) \end{cases}$$

where (N_1, N_2) denotes the charge filling of the DQD and $N_{1(2)}$ is the number of holes present in QD1(2).

This basis stays valid at finite magnetic field for electrons. But when dealing with holes, and due to the fact that the g-factors are different for each QD, the spin states behave differently and S(1,1) and T_0(1,1) are no longer eigenstates. A new basis of states $|\downarrow\downarrow\rangle$, $|\uparrow\downarrow\rangle$, $|\downarrow\uparrow\rangle$ and $|\uparrow\uparrow\rangle$ provides a better approximation of the DQD eigenstates in the (1,1) charge configuration. In this basis, the DQD Hamiltonian can be written as:

$$\mathcal{H}_{\text{even}} = \begin{pmatrix} \frac{\varepsilon}{2} - \Sigma g \mu_B B & 0 & 0 & 0 & t_{SO} \\ 0 & \frac{\varepsilon}{2} - \Delta g \mu_B B & 0 & 0 & t \\ 0 & 0 & \frac{\varepsilon}{2} + \Delta g \mu_B B & 0 & t \\ 0 & 0 & 0 & \frac{\varepsilon}{2} + \Sigma g \mu_B B & t_{SO} \\ t_{SO} & t & t & t_{SO} & -\frac{\varepsilon}{2} \end{pmatrix}, \tag{1.10}$$

where $\Delta g = g_1 - g_2$, $\Sigma g = g_1 + g_2$ and $g_{1(2)}$ the Landé g-factor of QD1(2).

As done previously, a simulation allows us to have the energy diagram of the even charge configuration as a function of the t_{SO}, t, g_1, g_2 and B parameters as illustrated in Fig. 1.6. The code for this case is also included in Appendix A.2.

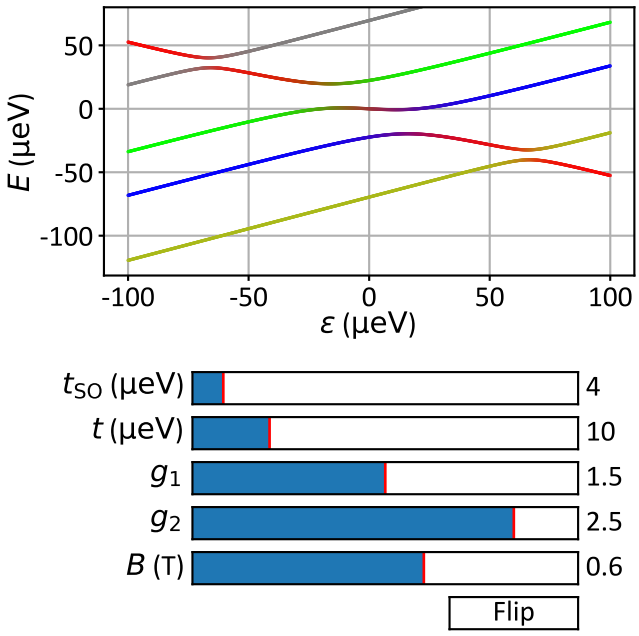

Figure 1.6 – **Energy diagram simulation of a DQD for an even charge configuration.** At the bottom, the interactive sliders of the t_{SO}, t, g_1, g_2 and B parameters allow for real time update of the energy levels.

1.2 Spin to charge conversion

In a spin qubit, the spin state encodes the quantum information that needs to be read or manipulated. But measuring the magnetic moment of a single particle (either electron or hole) is a very hard task since it is very small. To that extent, we need a quantity that could

be mapped to the spin state and, at the same time, more accessible measurement wise. The charge state fulfills both these requirements and spin to charge conversion was suggested to complement computation with quantum dots in Loss and Di Vincenzo proposal [84].

Many schemes for spin to charge conversion followed [67, 33, 34, 39, 46, 61]. But we focus in this section particularly on two schemes: the energy selective technique and a method based on Pauli spin blockade. For historical reasons, we present them for the case of electrons, but they can be applied also to holes which are the focus of this thesis.

1.2.1 'Elzerman' technique for spin readout

The spin readout discussed here, commonly referred to as 'Elzerman' readout [33], relies on a spin-to-charge conversion by energy-selective tunneling. It requires the QD hosting the spin qubit to be tunnel coupled to a Fermi reservoir. Following the application of an external static magnetic field B, the degeneracy between the spin up state $|\uparrow\rangle$ and a spin down state $|\downarrow\rangle$ is lifted, the Zeeman splitting energy being:

$$E_{\mathrm{Z}} = g\mu_{\mathrm{B}}B, \tag{1.11}$$

where g is the Landé factor. If E_{Z} is larger than the thermal energy, then it is possible to readout the spin state by adjusting the energy of the up and down spin states such that they lie below and above the Fermi energy of the reservoir, respectively. Fig. 1.7 displays the steps to achieve such process.

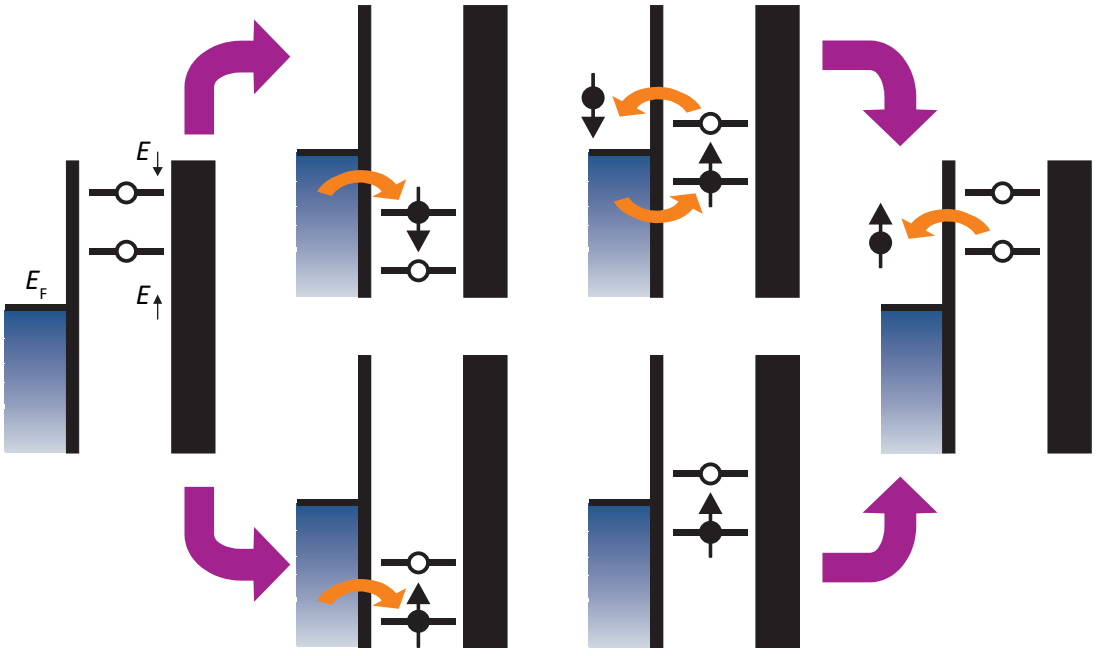

Figure 1.7 – **Spin to charge conversion 'Elzerman' scheme.** The quantum dot, subject to an external magnetic field, undergoes successively starting from left a loading stage, a readout stage and an emptying stage. Black vertical lines illustrate tunnel barriers and the gradient blue boxes indicate the Fermi sea of the reservoir. Taken from [33].

The 'Elzerman' sequence could be divided into three stages:

— **Emptying:** the cycle begins with an empty QD where both the spin up energy level $E_\uparrow$ and spin down energy level $E_\downarrow$ are lifted above the Fermi level E_F. The electron encoding tunnels out of the QD into the Fermi reservoir.

— **Loading:** by pulsing on the gate voltage controlling the chemical potential of the dot, both $E_\uparrow$ and $E_\downarrow$ are lowered below the Fermi energy for a waiting time t_{wait}. An electron with a randomly oriented spin is loaded into the QD. The spin down (up) scenario is shown in the upper (lower) part of the diagram in Fig. 1.7.

— **Readout:** after the gate pulse QD energy levels are set to the readout position such as E_F lies in between $E_\uparrow$ and $E_\downarrow$. If the loaded electron spin is pointing up, its energy level is below that of the Fermi sea and thus it remains on the QD. While in the other case, if the spin in pointing down, its energy is higher than E_F and a tunneling event towards the reservoir occurs. Right after losing a spin-down electron the QD is repopulated with a spin-up electron. The charge measurement is acheived by means of a charge sensor.

The 'Elzerman' sequence above offers a way to measure the spin relaxation time T_1. If a loaded spin down electron is maintained in the loading step long enough, it will end up relaxing to the less energetic spin up state. Ergo, by following the spin down fraction of the measured state as a function of the waiting time t_{wait}, an exponential decay should be observed from which the characteristic spin relaxation time can be extracted.

Since the first proof of concept implementation [33] in GaAs QDs probed by a quantum point contact (QPC), many groups around the world reproduced this experiment and adapted it for their specific qubit device implementation from which we could mention silicon electron qubits made by a depleted two dimensional electron gas (2DEG), probed by a single electron transistor (SET) [94] and Ge hut wire hole qubits probed by radio frequency (RF) reflectometry carried out on a single hole transistor (SHT) [143, 144].

The 'Elzerman' scheme offers some considerable advantages such as a robust measurable signal enabling single-shot readout, a simple initialization in the fundamental state and the possibility to be performed on a single spin. It remains widely adopted in the community. Nonetheless, it carries some drawbacks. The need for a charge detector and for a reservoir, where the density of states shouldn't be structured, makes it hardly scalable. Besides, 'Elzerman' readout requires low operating temperatures and rather high external magnetic fields (so that the Zeeman splitting exceeds the temperature broadening). The electron tunnel rates need also to be fast compared to the spin relaxation time but slow enough compared to the readout bandwidth. Moreover, the measurement of the quantum state is fully destructive as the electron in the excited spin state tunnels out of the dot and is replaced by another one with an opposite spin orientation.

1.2.2 Pauli spin blockade

The phenomenon of Pauli spin bloackade (PSB) was first observed in current transport through a vertical DQD [104]. It was shown that interdot tunneling involving a transition from a (1,1) to a (0,2) charge state is suppressed when the (1,1) state is a spin triplet. In this case, since the (0,2) state is a spin singlet, the interdot transition does not conserve spin, which makes it unfavorable in the absence of spin-flip mechanisms. This is a direct consequence of the Pauli exclusion principle stating that two particles occupying the same orbital must have opposite spins.

As a result, PSB generally occurs in "even ↔ even" interdot transitions. Experimentally, it manifests as a suppression of the the source-drain current I_{SD} at the basis of the bias triangles depending on bias voltage V_{SD} polarities as presented in Fig. 1.8.

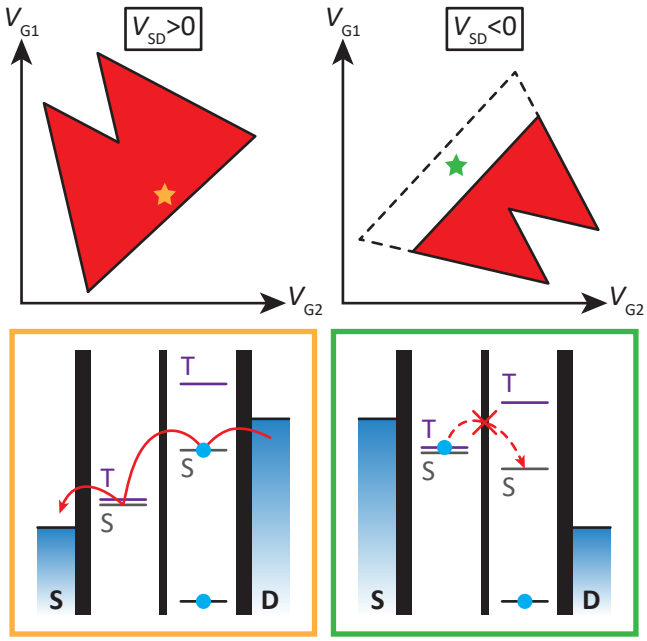

Figure 1.8 – **Pauli spin blockade and bias triangles.** Theoretical source drain current as a function of gate voltages V_{G1} and V_{G2} in the cases of positive (left) and negative (right) source drain bias. The red coloration indicates where the current is not zero. The dashed lines in the negative bias voltage represent the limits of the bias triangles in the absence of PSB. Level alignments diagrams corresponding to the marking stars on the stability diagrams illustrate the transport mechanism at the bases at the bias triangles and explain the current suppression when $V_{SD} < 0$.

For the sake of simplicity, we consider a (1,1) ↔ (0,2) transition. In the case of a bias voltage inducing an electron flow in the direction (0,2) → (1,1) and in each charge transfer, an electron is initially loaded onto the right QD from the drain reservoir forming a S(0,2) state (this tunneling event is always allowed since a Fermi sea can provide electrons with any spin orientation). The electron can then tunnel to the initially empty left QD forming a singlet S(1,1) state, and thereafter to the source reservoir.

For the opposite V_{SD} polarity, where charge flow involves (1,1) → (0,2) transitions, transport is allowed only via the path reservoir → S(1,1) → S(0,2) → reservoir. As soon as an electron tunneling from the source populates the triplet T(1,1) state, transport gets blocked. Seeing that tunnelling between QDs conserves spin, tunneling into the energetically accessible S(0,2) is forbidden. The electron remains trapped in the right dot which materializes in the disappearance of the I_{SD} signal. The current flow cannot be restored until the spin in question flips leading to a S(1,1) state, revoking thereby the blockade. Nevertheless, the timescale of such relaxation is most of the time long enough to make the flowing current undetectable. In the case of a relatively fast spin-flip mechanism, only a reduction in the measured current is observed at the basis of bias triangles. On the other hand, the blockade can be lifted for sufficiently large source-drain bias enabling the T(0,2) state to enter the bias window (this assumes a bias greater than the energy difference between T(0,2) and S(0,2)). This is the reason why the bias triangles are only partially visible for $V_{SD} < 0$ (Fig. 1.8).

PSB has been adopted as a spin to charge conversion technique granting spin state readout in a DQD and a first demonstration was reported for GaAs-based devices [112]. Unlike the 'Elzerman' scheme, it offers more liberty when it comes to the readout method. It could be probed by transport [64, 125, 13, 78, 82, 9, 89, 76], a charge detector [64, 112, 11, 132] or RF gate reflectometry [26, 86]. It also relaxes the constraints on scalability since it doesn't require reservoirs nor proximal charge detectors if the readout technique could sense just the interdot tunneling as we will discuss in Chap. 4.

In the prospect of developing a scalable path, this thesis has focused on the PSB spin to charge conversion method in combination with gate reflectometry readout.

1.3 Electric dipole spin resonance

As we mentioned in Sec. 0.3, holes offer the possibility for an electric-field control of the spin qubit state. This is made possible thanks to the presence of the spin-orbit interaction. In the case of a moving particle experiencing an electrostatic potential V, the spin-orbit Hamiltonian can be written as [149]:

$$\mathcal{H}_{\mathrm{SO}} = -\frac{\hbar}{4m_0^2c^2}\,\boldsymbol{\sigma}\cdot(\boldsymbol{p}\times\nabla V), \tag{1.12}$$

where m_0 is the particle mass, c the speed of light, $\boldsymbol{\sigma}$ a vector of the Pauli matrices and $\boldsymbol{p}$ the momentum operator.

A charge with a mass m and with a velocity $\boldsymbol{v} = \boldsymbol{p}/m$ submerged in an electric field $\boldsymbol{E}$ sees in its proper frame an effective magnetic field $\boldsymbol{B}_{\mathrm{SO}} = -\boldsymbol{p}\times\boldsymbol{E}/(mc^2)$. The spin-orbit interaction is no other than the result of interaction between B_{SO} and the particle magnetic moment. Based on Eq. (1.12), since both the momentum of a particle as well as the electric field get larger when approaching the nucleus, the spin-orbit interaction is higher the closer we get to the atomic core. First orbitals exhibit therefore the strongest spin-orbit couplings and a similar logic leads to stronger spin-orbit interactions for heavier elements.

In QDs, the confinement is such as the momentum of a particle on average is zero in any direction. As a consequence, the spin-orbit Hamiltonian (Eq. (1.12)) does not couple different spins on the same orbital but couples states with different orbital as well as spin components [72]. This means that pure spin states are replaced by pseudo-spin states that are admixtures of both orbital and spin states.

Due to the mixing of spin and orbital states, an electric field could couple to the pseudo-spin states of the same Kramers doublet through spin-orbit coupling. It has been predicted [42] that an electric dipole spin resonance (EDSR) could be induced by means of oscillatory electric fields at a frequency matching the Zeeman splitting energy [103, 98, 89, 146, 26]. While this allows for a compact qubit device design, free of metal striplines used to generate local AC magnetic fields for electron-spin resonance, there is a price to pay. Electric field fluctuations originating from charge noise or even lattice phonons [43] promote spin relaxation and decoherence [87, 14]. Nevertheless, it remains a viable approach for fast qubit manipulation [89, 151] and can result in high qubit fidelity [152, 52, 15].

When applying an oscillating field at a microwave frequency $f_{\mu\mathrm{w}}$ to a QD by means of a

gate-voltage modulation, the trapped charge electronic orbitals jiggle. The spin-orbit interaction translates this motion into rotations of the spin. This is the equivalent of applying an oscillating magnetic field to control the spin state via electron spin resonance (ESR) [75, 113, 137] since as discussed previously, an oscillating electric field is equivalent to an oscillating magnetic field in the charge referential. When the $f_{\mu w}$ matches the Larmor frequency, full spin rotation from up to down states are observed. Fig. 1.9 schematizes the spin rotations induced by the charge spatial movement.

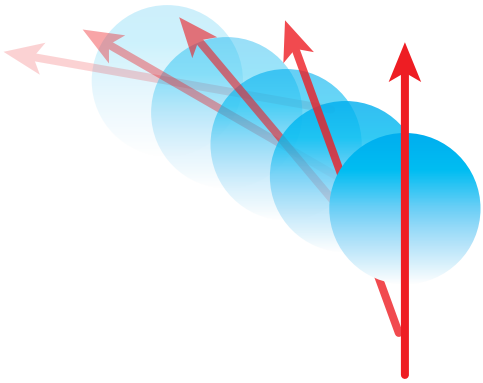

Figure 1.9 – **Illustration of EDSR.** By shaking the charge with an external microwave electric field at a frequency around the Larmor frequency, spin rotations are induced.

Two contributions, generally coexisting, underlie the EDSR mechanism and could be captured simultaneously by a g-matrix formalism [27]:

— iso-Zeeman EDSR (IZ-EDSR): It describes an EDSR where the g-factor is constant (*i.e.* position independent) and was inspected originally in III-V semiconductor structures [103, 98, 109]. The charge moves in an electric field and sees in its referential an oscillatory magnetic field that causes spin rotation around an equatorial axis (see Fig. 0.2).

— g-tensor magnetic resonance (g-TMR): Discovered in a GaAs/AlGaAs heterostructure [68], it denotes a mechanism where the g-tensor changes with the position (*i.e.* the orbital wave function) of the confined particle [68, 124, 129, 5, 141]. An electric-field induced spatial oscillation results in a modulation of the g-tensor, which is equivalent to a transverse modulation of the magnetic field leading to spin rotation.

1.4 Reflectometry

Both Elzerman and Pauli spin blockade are charge sensing based mechanisms as they are spin to charge conversion schemes. As an alternative to transport-based readout, which is typically characterized by a limited bandwidth, the technique of RF reflectometry was introduced by Schoelkopf and co-workers back in 1998 [121]. This first realization, using metal SETs, was

shown to provide large readout bandwidth enabling a readout speed two orders of magnitude greater. The idea was then exported to semiconductor devices in particular for achieving fast spin-qubit readout and different implementations of RF reflectometry were reported over the years.

1.4.1 Principle

RF reflectometry is a non invasive charge detection technique used to uncover new physics at the single charge level taking place in nanoscale devices. This technique relies on the measurement of the dispersive response of a RF resonator, excited at its resonance frequency, and connected to either an ohmic contact or a gate. The dispersive response depends on shifts in the device admittance [60] due to charge tunneling events or charge hybridisation. Fig. 1.10 gives the basic idea behind RF reflectometry. This will not only allow probing full charge stability diagrams at zero bias, but will also give access to excited quantum levels of the probed QD even when a state isn't generating enough DC current to be measured. In principle, this technique could also use a resonant circuit shared by many qubits via frequency multiplexing [54].

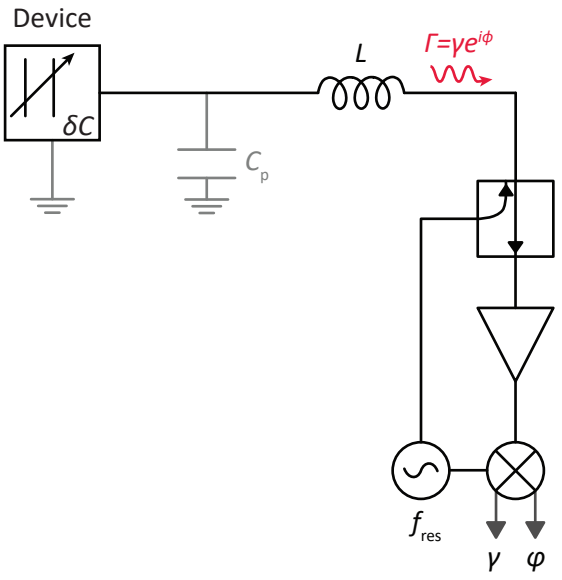

Figure 1.10 – **Illustration of reflectometry principle.** The inductance L along with the parasitic capacitance C_p (and eventually other added capacitors) form an LC resonator. By exciting this resonator at its resonance frequency f_res, it becomes sensitive to variations δC of the device capacitance. These variation manifest as alterations in the reflected signal Γ that gets separated from the injected signal by a directional coupler, then amplified before being demodulated at f_res in order to get its amplitude (γ) and phase (φ) variations.

Either the amplitude [121, 19, 117] or/and the phase [1, 26, 35] of the reflected signal can be used as a readout signal but we will focus on the reflected phase since we are eventually interested in quantum capacitance changes at the interdot transition leading to phase shifts only, while dot lead transitions can lead to real and imaginary changes in the device admittance. As shown in Fig. 1.11, the unwrapped phase derivative with respect to the injected frequency f_inj exhibits a peak. This means that if the resonator is excited at its resonance frequency f_res, it will be very sensitive to variations of f_res. Any shift in the quantum capacitance (and thus

in the resonance frequency f_{res} of the system {resonator + QD}), in this case, will lead to an optimal response in terms of phase shift $\delta\varphi$.

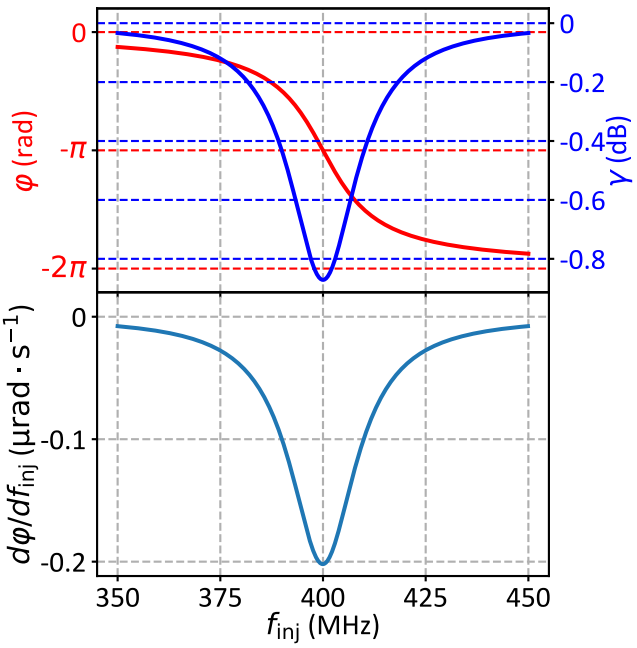

Figure 1.11 – **An example of a LC resonator response.** Reflected phase φ and amplitude γ of a LC resonator (top panel) as a function of the injected frequency f_{inj} and the corresponding derivative of the φ with respect to f_{inj} (bottom panel). The phase derivative is maximal around the resonance frequency ($f_{res} = 400\,\text{MHz}$) indicating a maximal sensitivity to capacitance changes.

As charge sensors were at the heart of readout techniques at the beginnings of semiconductor QD qubits, reflectometry was first transposed to SETs [121, 19, 85, 118, 101, 153] and QPCs [117, 16, 2, 88]. It has immediately gained considerable interest because it gives access to high sensitivities reaching $0.9\,\mu e/\sqrt{\text{Hz}}$, the best charge sensitivity known to date [12]. Single-shot readout has also been achieved using reflectometry [143, 106, 144, 148, 71, 132, 51] with fidelity up to 98 % for 6 µs integration time with on-chip resonators [156] which confirms its potential for qubit readout. It was only later, in the effort of simplifying the qubit layouts, that gate-coupled reflectometry appeared [23]. It is the adopted reflectometry disposition in this thesis that will be detailed in the next section.

1.4.2 Gate-coupled reflectometry

The commonly used spin-to-charge conversion with subsequent charge detection through nearby charge sensors is becoming increasingly challenging as the number of quantum dots to sense increases [95, 52]. Gate-coupled RF reflectometry comes as an alternative to the proximal QPC and SET techniques that also allow charge configuration detection in regimes where the direct transport isn't possible. Since it is necessary to integrate charge sensors to perform qubit readout in order to achieve scalable quantum computers [116], and knowing that QPC and SET rely on charge sensitive devices involving a considerable overhead in terms of gates and contact leads raising a serious issue for scalability towards multi-qubits designs, gate-coupled RF reflectometry [20, 28, 23, 44] has been proposed as an alternative technique for qubit readout. This

would yield a simplified qubit physical layer [116] due to the absence of local charge sensors and so a tighter qubit pitch.

Gate-coupled reflectometry has been proven to give access to sensitivities and bandwidths comparable to the local charge detectors [44]. It has also been used, when combined with charge-to-spin conversion processes, to measure spin states in DQDs [110, 66, 9]. In a similar fashion, the phase shift of a superconducting microwave resonator coupled to the source of an InAs nanowire has enabled spin qubit dispersive readout [109].

The measured device acts as a variable impedance load for the resonator, and the resonant frequency f_{res} undergoes a dispersive shift according to its state. A charge tunneling between the probed dot and a reservoir or between the two dots gives rise to a small capacitance variation δC seen by the resonator besides the other geometric capacitances. This variation is given [28] by :

$$\delta C = -e\,\alpha\,\frac{\partial\langle\nu\rangle}{\partial V_{\text{G}}}, \tag{1.13}$$

where e is the electron charge, α is the lever-arm parameter (the the proportionality factor that allows the conversion of the gate voltage V_{G} into energy, which can also be seen as the effectiveness of the gate voltage to act on the QD chemical potential), and $\langle\nu\rangle$ is the average excess charge on the dot. This capacitance variation leads to phase variation [32]:

$$\delta\varphi \propto -\delta C, \tag{1.14}$$

whenever the charge dynamics is faster than the probing frequency (f_{res}).

In the case of DQD, the probed capacitance variations associated with interdot tunneling can be split into two contributions [93]:

$$\delta C = \delta C_{\text{quantum}} + \delta C_{\text{tunneling}}, \tag{1.15}$$

where C_{quantum} is the quantum capacitance corresponding to the second derivative of the involved energy level with respect to the detuning ε (curvature of the energy level), and $\delta C_{\text{tunneling}}$ the tunneling capacitance appearing whenever inelastic tunnelling processes occur.

Gate reflectometry can as well detect charge tunneling between a QD and a Fermi reservoir, provided the tunnel rate exceeds the probing frequency. In this case a phase shift is produced whenever a hole/electron is tunneling back and forth between the QD and the neighboring reservoir. This requires the chemical potential of the dot to be aligned with the one of the said reservoir.

We have just discussed the origin of the quantum capacitance in a semi-classical picture. A fully quantum derivation will be presented in Chap. 6.

Takeaway messages:

- Transport in a single QD is possible only when a chemical potential is in the bias window.
- In a DQD, the chemical potential of a dot depends on the filling of the other QD due to a mutual coupling capacitance and transport is only possible in specific regions of the stability diagram near the ICTs.
- Spin states in a DQD differ from an odd to an even total charge number and simulations made by diagonalizing the Hamiltonians in each case help us paint the energy diagrams as a function of the system parameters.
- In order to read the spin state, a spin to charge conversion mechanism is needed. Energy selective spin to charge conversion can be achieved either by the 'Elzerman' technique or by Pauli spin blockade.
- The spin orbit interaction, coupling the orbital state of a particle to its spin state, is intrinsically present for holes and could be exploited to electrically manipulate the spin state through EDSR.
- RF reflectometry is a readout technique offering better measurement speeds and high sensitivities. It allows for single shot readout and, in the case of the gate-coupled version, a more simplified qubit architecture through the removal of proximal charge detectors.

1

Chapter 2

Silicon-On-Insulator spin qubit devices

> No physical quantity can continue to change exponentially forever. Your job is delaying forever.
>
> Gordon MOORE

Contents

Nowadays, transistors are everywhere. Either packaged individually or embedded in integrated circuits, they are considered one of the fundamental building blocks of modern electronics. A transistor can be seen as current switch as its base (gate) voltage controls the charge flow between its emitter (source) and collector (drain). It was invented in Bell Labs in 1947 and brought the 1956 Nobel prize to its creators.

As transistors grew smaller and smaller every year, they became viable solutions for quantum applications. Their dimensions can allow for charge confinements presently when the certain experimental conditions are met, *e.g.* cryogenic temperatures. While the first transistor ever made could easily fit in the palm of a hand, the latest 2020 smartphone processors such as Apple A14 (iPhone 12), Qualcomm Snapdragon 888 (Xiaomi Mi 11 and Samsung Galaxy S21) and Samsung Exynos 2100 (Samsung Galaxy S21) rely on 5 nm node fabrication process.

The devices used during this thesis are nanowire field-effect transistor (NW-FET) made on a 300 mm silicon-on-insulator (SOI) processing line [7] in CEA-LETI. We detail their fabrication in this chapter, their geometries and the steps leading to their cooldown inside cryostat.

2.1 Complementary metal oxide semiconductor

Complementary metal oxide semiconductor (CMOS) is an integrated circuits production technology. It links together numerous transistors in a proper way and is present in a variety of electronic components such as microprocessors. It relies on metal-oxide-semiconductor field-effect transistors (MOSFETs), also called "MOS" transistors (hence the "MOS" part in "CMOS"), the most widely used transistor type which was also invented at Bell Labs in 1959. The "complementary" part of the naming refers to the use of pairs of n-type (high concentration of electrons) and p-type (high concentration of holes) transistors in order to achieve the logic functions. This transistor technology is praised for its relatively low power consumption. Except when they change from one state to another, the CMOS transistors do not require an electric current through the gate electrode.

2.2 Silicon-on-insulator

Silicon-on-insulator (SOI) technology is a fabrication technique of semiconductor silicon devices. Its name derives from the fact that the silicon channel is made on an insulator layer, typically silicon oxide, deposited on a silicon substrate in turn. Despite the additional cost, mainly due to the production of SOI substrates, compared to the traditional technology using directly a bulk silicon substrate, this approach is adopted for numerous advantages such as the reduction of the parasitic capacitance within the chip [17]. As we seek more than ever the miniaturization of semiconductor devices, hoping to extend Moore's Law, it is considered, among others, a strategy towards that end.

There are two main methods to make a SOI wafer. The first called Separation by IMplantation of OXygen (SIMOX) [100] starts by embedding an oxygen layer in the silicon bulk by ion beam implantation. The wafer undergoes afterwards a high temperature annealing step that creates a buried silicon oxide (SiO_2) layer. The second process called wafer bonding [80] consists of forming the insulating layer by oxidizing the upper part of the silicon substrate then directly bond the said layer on a second silicon substrate.

2.3 Fabrication & device geometries

In order to obtain devices with qubit functionality, and at the same time leverage the well established CMOS technology, we make our starting square an existing process flow aimed for the manufacturing of CMOS transistors and we alter it [7]. We adopt thereby from the beginning a scalable fabrication process that enables production of qubit devices in an industrial cleanroom and allows the co-integration with classical circuitry.

Starting from a SOI wafer, a silicon nanowire is etched. Its width is trimmed to desired width by controlled oxidation and etching process defined initially by deep ultra-violet lithography. Starting from this point different geometries can be obtained based on the gate layout.

For the geometry where the gates are in series with respect to source and drain, which we name 'pump' geometry, and using a combined deep ultra-violet lithography and e-beam lithography, two separate gates are patterned on the next step. Thanks to the latter combination of techniques, the necessary small spacing between the gates could be achieved. These gates

are composed of two layers. The first one is a thin 5 nm TiN layer that lies under a 50 nm thick polysilicon layer. They are electrically isolated by a dielectric stack of 7 nm SiO_2 followed by a 2 nm Hf-based high-k dielectric. SiN spacers are successively deposited around the gates with a width large enough to fully cover the nanowire channel between the gates and protect it from the next step. The device undergoes afterwards an ion implantation process, required for the creation of low resistance ohmic contacts to the nanowire channel. The used samples are doped with boron ions and therefor they are p-type. Their diffusion from the heavily doped contact regions to the nanowire channel is limited by the wide SiN spacers. Fig. 2.1 shows the described keys steps of the fabrication process. The sample is finalized thereupon with a standard microelectronics back-end of line process.

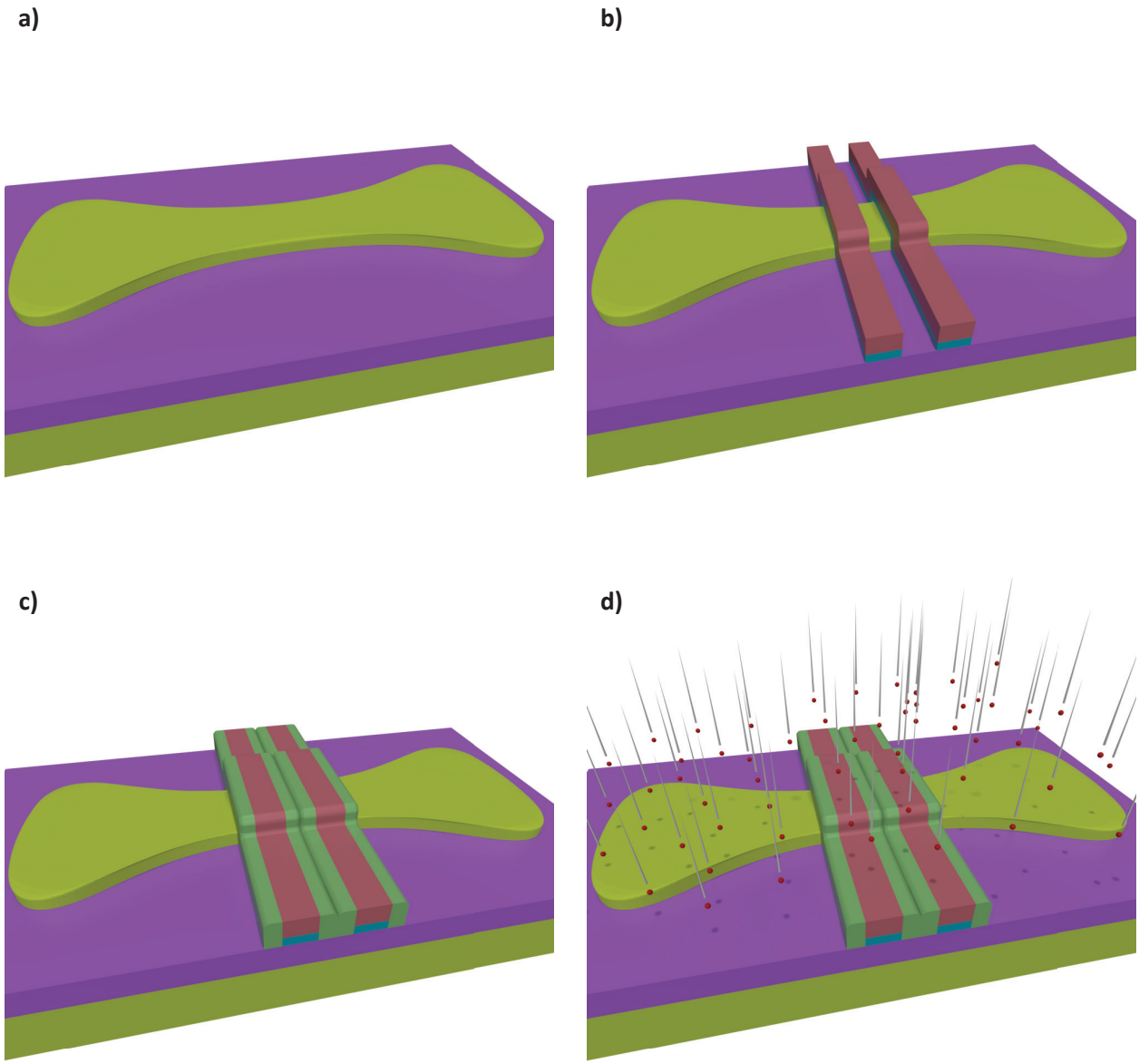

Figure 2.1 – **Schematic illustration of a pump device fabrication key steps.** Silicon is represented in yellow, SiO_2 in purple, TiN in blue, polysilicon in red and SiN in green. **(a)** Silicon nanowire etching. **(b)** Gate definition. **(c)** Deposition of insulating spacers around the gates. **(d)** Boron doping.

The resulting device is illustrated in Fig. 2.2 along with its scanning electron micrograph (SEM). The doped electrodes become metallic and serve as source and drain charge reservoirs. Transport from source to drain is only possible in this configuration when both gates open the channel. At cryogenic temperatures, holes are accumulated under the gates. This geometry led to the first demonstration of a CMOS hole spin qubit [89].

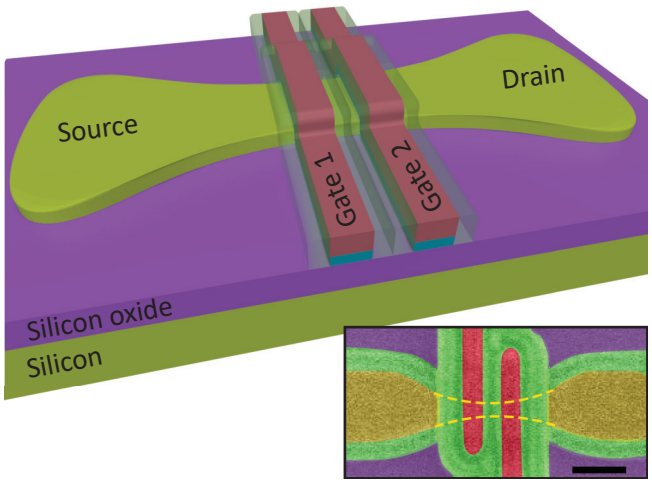

Figure 2.2 – **Schematic illustration of a two-gate pump sample.** The gates are in a series configuration with respect to source and drain. A charge could flow through the channel only by acting on both gates. The insulating spacers around the gates are represented in semi-transparent. The inset shows a false color SEM of the device with colors matching the 3D schematic. The scale bar measures 100 nm.

For the 'face-to-face' geometry, also called 'split-gate' geometry, where the gates are in parallel with respect to source and drain, the fabrication steps differ slightly (see Fig. 2.3). Only one gate is patterned using the same process as the previously described geometry and is also composed of the same gate stack. This gate is thereupon split in two by etching a gap aligned with the symmetry axis of the silicon channel. SiN spacers are deposited around the gates with a width large enough to fully cover the nanowire channel between the gates and protect it from the following dopant implantation. Finally, the boron implantation makes the nanowire extremities metallic leads.

Fig. 2.4 gives a 3D schematic of a split gate device. The charges could flow from source to drain from either side of the channel in this geometry. The holes are accumulated at the corner interface on which the gate overlaps the silicon nanowire.

All of the above presented fabrication steps are fully based on standard processes of a CMOS line except for the intermediate e-beam lithography step. Three different samples are investigated in this thesis. Table 2.1 summarizes the characteristics for each one of them.

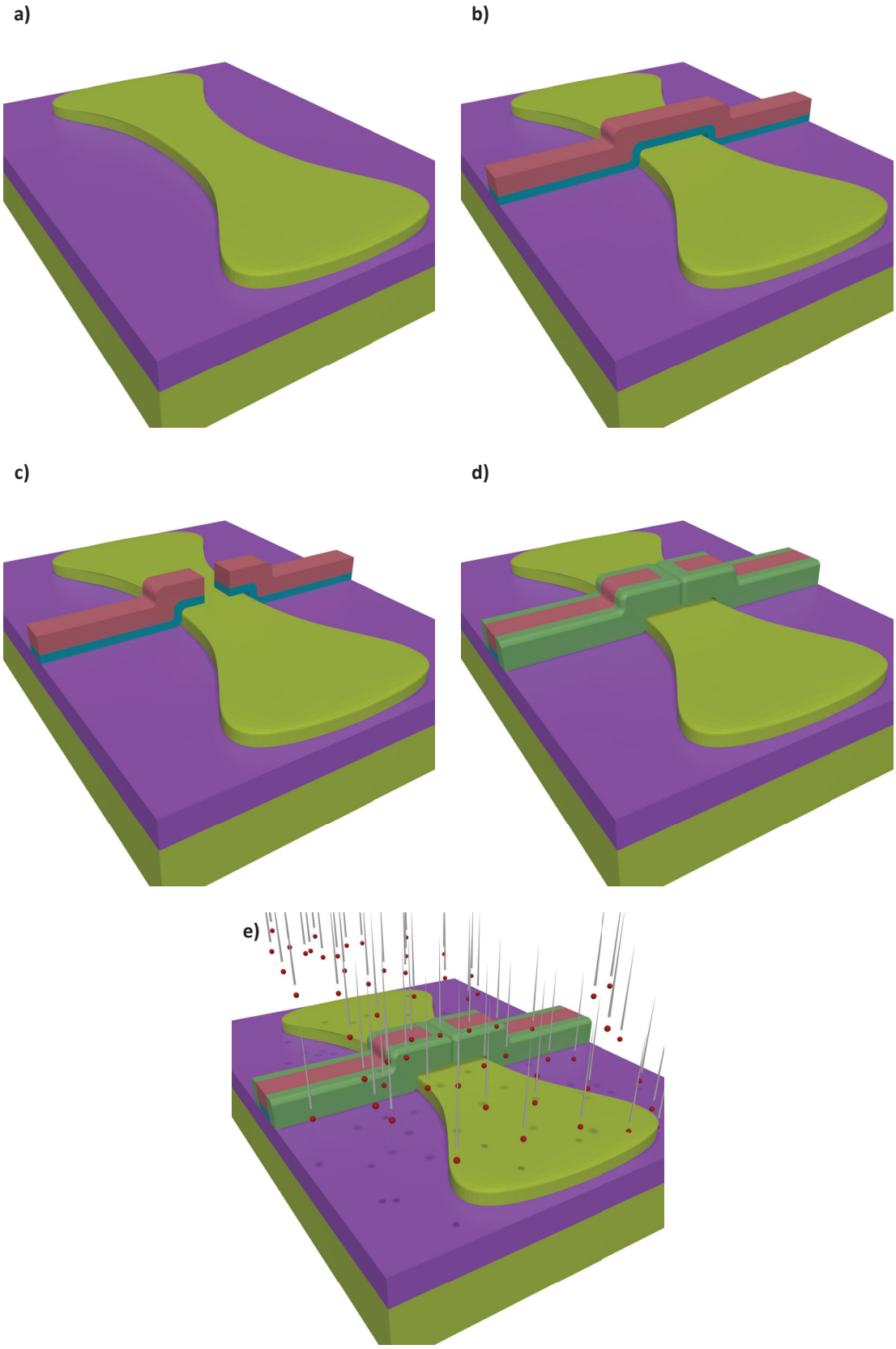

Figure 2.3 – **Schematic illustration of a face-to-face device fabrication key steps.** Silicon is represented in yellow, SiO_2 in purple, TiN in blue, polysilicon in red and SiN in green. **(a)** Silicon nanowire etching. **(b)** Gate definition. **(c)** Gate splitting. **(d)** Deposition of insulating spacers around the gates. **(e)** Boron doping.

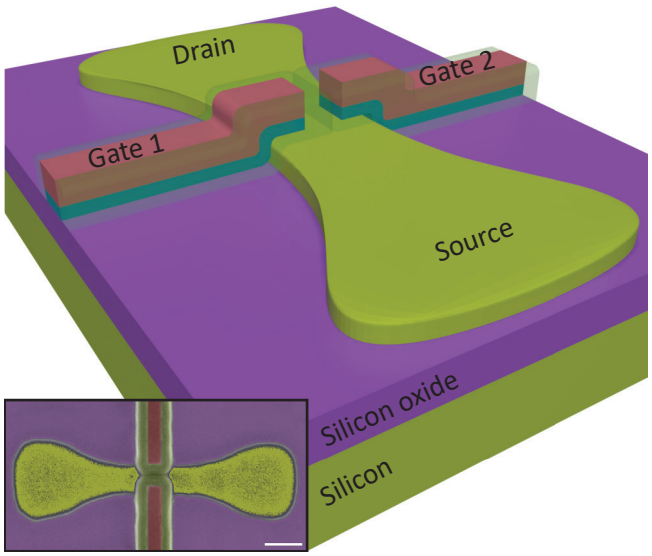

Figure 2.4 – **Schematic illustration of a single split-gate sample.** The gates are in a parallel configuration with respect to source and drain. A charge could flow through the channel by acting on only one gate. The insulating spacers around the gates are represented in semi-transparent. The inset shows a false color SEM of the device with colors matching the 3D schematic. The scale bar measures 100 nm.

	device 1 (Chap. 4)	**device 2** (Chap. 6)	**device 3** (Chap. 6)
Geometry	pump	face-to-face	face-to-face
Doping	p	p	p
Number of gates	2	2	2
Channel width (nm)	35	80	50
Channel height (nm)	11	10	10
Gate width (nm)	35	32	50
Gates separation (nm)	35	32	50

Table 2.1 – **Samples characteristics and dimensions.**

2.4 Procedures upon reception

The devices used for cryogenic experiments are often received embedded in 300 mm wafers containing at once thousands of them. Fig. 2.5 shows a picture of such received wafer. Before delivering a wafer, the LETI team, responsible for the device design and manufacturing, performs some automated measurements on samples with simple geometries (single and double gate). The measured I-V characteristics and gate leakages serve as guidelines in order to assess the yield of the fabrication process and the quality of the transistors. They are also used on our side to select the devices that show the expected room temperature properties.

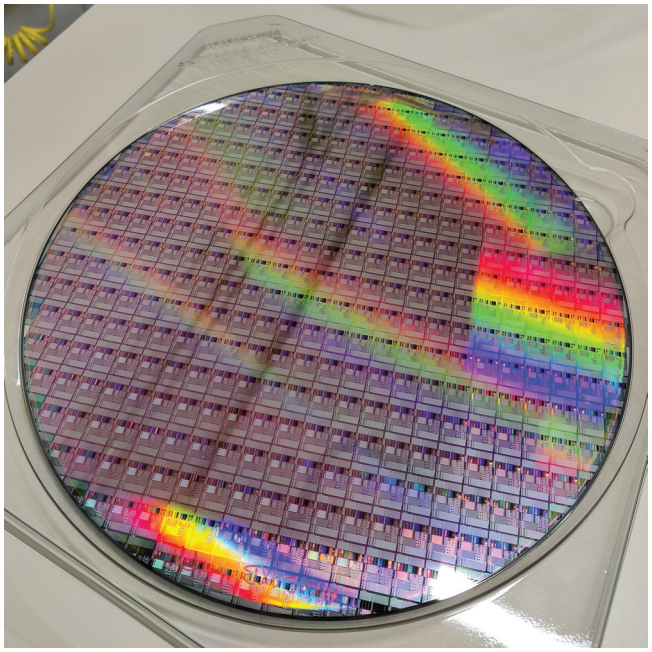

Figure 2.5 – 300 mm **wafer.** The measured devices are fabricated on 300 mm wafer received often as whole.

Whenever room temperature I-V measurements of samples with a large number of gates are needed (more than two gates), the whole wafer is loaded into the in-lab automated measurement station presented in Fig. 2.6. It can also be used to confirm measurements already done on the LETI side. Micro-needles are programmed to enter in contact with the desired samples pads and apply predetermined voltages while measuring at the same time a current flow.

In order to assess the viability of a device for being a cooldown candidate, we start by measuring the inter-gate leakage. Once we are assured that no detectable current could be measured between each set of two gates held at different potentials, we start looking at the source-drain current I_{SD} as a function of the gate voltages. Aside from enabling us to notice any device fabrication anomalies, this room-temperature measurement can help extracting the threshold voltage for each gate which will translate once the the sample is cooled down into an approximate estimation of the gate voltage corresponding to the filling of the first hole in the channel region under the gate. In the case of a pump geometry such as the case of device 1 of which the I-V characteristic is displayed in Fig. 2.7, current can only flow from source to drain when all gates open the channel. Therefore, whenever we sweep one of the gates, the others are kept at relatively large negative voltage (typically $-1.5\,\mathrm{V}$ or $-2\,\mathrm{V}$).

In the case of the face-to-face geometry, such as device 2 and 3, holes can flow under either one or the other gate. Accordingly, when measuring the effect of one of the gates on I_{SD}, the

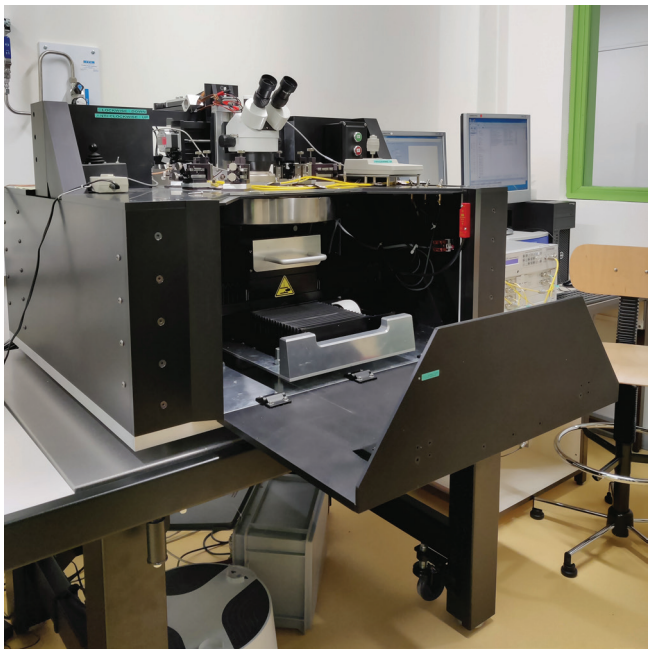

Figure 2.6 – **Automated measurement station.** Room temperature characteristics of the samples are probed using the automated measurement station where a 300 mm wafer is loaded as whole.

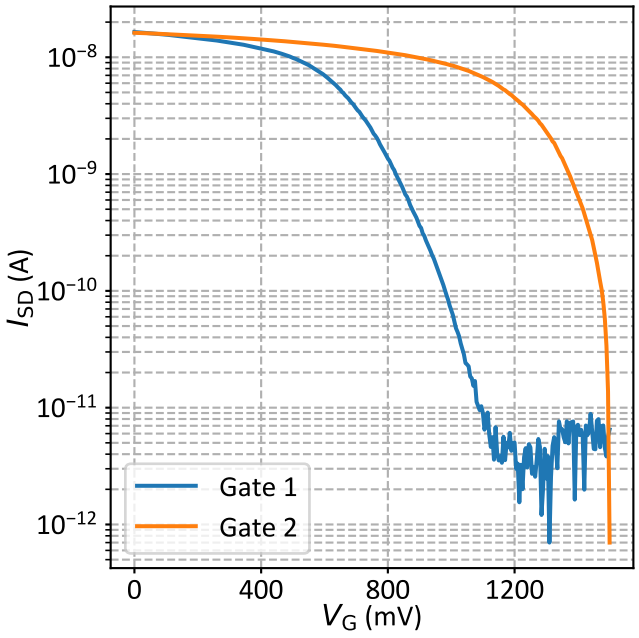

Figure 2.7 – **Room temperature I-V characteristic of device 1.** Source-drain current I_{SD} as a function of gate voltage. A 5 mV bias is applied between the source and drain electrodes. A Since the device is of a pump geometry, the other gate is held at 0 mV (fully open) while the other gate is swept.

other facing gate is held at a pinch-off voltage (typically either zero or positive voltage). See Fig. 2.8 for the I-V characteristic of device 2 given as an example for this device geometry.

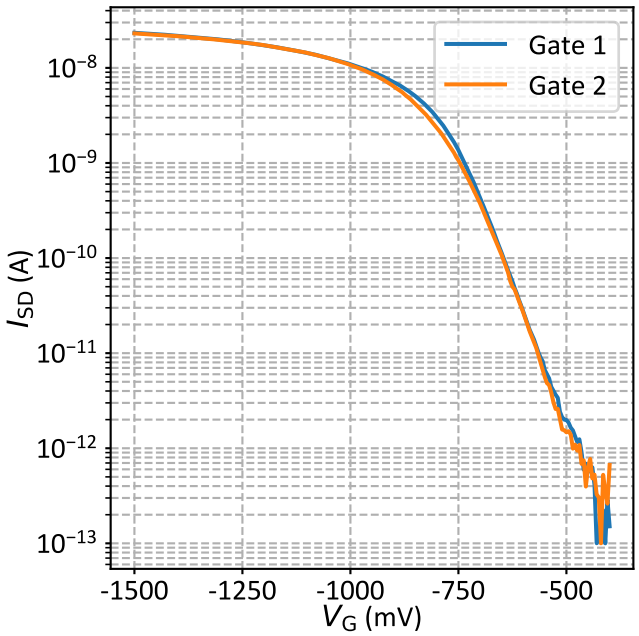

Figure 2.8 – **Room temperature I-V characteristic of device 2.** Source-drain current I_{SD} as a function of gate voltage. A 5 mV bias is applied between the source and drain electrodes. A Since the device is of a face-to-face geometry, the other gate is held at 1 V (fully closed) while the other gate is swept.

Following a full wafer-scale characterization of the basic electrical properties, we cleave the wafer along the silicon crystallographic directions into 13 mm by 16 mm dies as presented in Fig. 2.9. This characterization is used in the selection process of a device, which consists of exploring all I-V curves for a particular wafer and cross referencing them with the desired sample dimensions. In general, a die holds a specific functional circuit. In our case, a die is the reproduced unit throughout the wafer that contains all device types (different geometries and dimensions).

Now that the die containing the desired sample is cut ready, we need to further isolate the device by cleaving a small piece that will fit into the sample holder as shown in Fig. 2.10. The latter is a printed circuit board (PCB) containing the suitable connectors to the fridge RF and DC lines. It is manually prepared by soldering the surface-mount components constituting the bias tees and the readout resonator as well as the connectors. The chip containing the desired device is glued on the PCB via silver paste to ensure electrical contact between the substrate and a metal pad underneath.

Electrical connections between the contact pads on the sample holder and the device bonding pads are made by means of an ultra-sonic micro-bonding machine, pictured in Fig. 2.11, using silver micro-wires.

The device is now ready to be hooked up to the cryogenic setup.

Figure 2.9 – **Wafer dicing.** The 300 mm wafer is cut into dies. Each die contains many samples of different geometries serving different purposes. A wafer map helps identifying the dies numbers depending on their positions in the said wafer. A piece of the second die (top left) containing a desired sample has been cut.

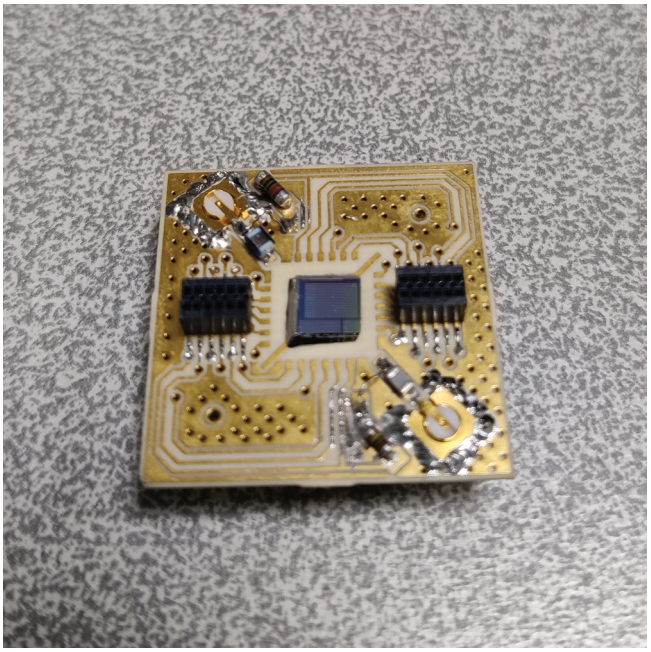

Figure 2.10 – **Sample holder.** The PCB on which the sample is glued and which is connected afterwards to the cold finger of the fridge. A piece of a die containing a desired sample has been glued to the center of the sample holder using silver paste. Two mini-SMP connectors (top left and bottom right) assure the delivery of microwave signals to the sample. The black connectors (middle left and right) are used for DC signals. All the electronic components are manually soldered.

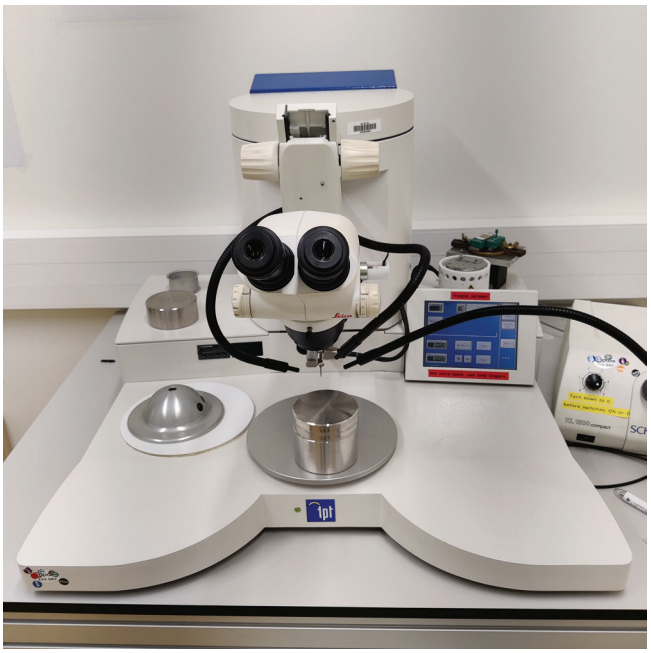

Figure 2.11 – **Ultrasonic micro-bonding machine.** The sample terminals are connected to the sample holder pads by means of silver micro-wire bonded on each side using pressure and ultrasonic vibrations. The binoculars help position the bonding needle in the desired spots.

Takeaway messages:

- The samples used in this thesis are silicon NW-FETs made on 300 mm SOI substrates.
- The key fabrication steps are the etching of the Si nanowire, the definition of gate electrodes (by optical and e-beam lithography), deposition of spacers around the gates and finally the doping of the source and drain electrodes.
- In a face-to-face geometry, also called split-gate geometry, the gates are partially overlapping the channel and face each other. Source-drain current can flow under either of them, with no need of having charge accumulation simultaneously under both gates.
- In a pump geometry, also called series geometry, the gates are overlapping the whole channel width at separate positions along the nanowire. Source-drain current can flow only by simultaneously biasing both gates to charge accumulation mode.
- The devices are embedded in 300 mm wafers which are initially characterised using additional measurements with an automated station and successively diced. Small chips (typically 5 mm by 5 mm) containing the selected devices are then mounted and microbonded on a sample holder with DC and RF connectors and passive surface-mount components.

2

Chapter 3

Implementation of reflectometry readout

> The experiment should be set up to open as many windows as possible on the unforeseen.
>
> Frederic JOLIOT-CURIE

Contents

In this chapter, the experimental setup used throughout this thesis is presented. We shall provide some general experimental details common to the different experiments discussed in the following chapters. The characterization of the resonators used for RF gate reflectometry for each studied sample is also included in this chapter. Furthermore, we introduce two important quantities that measure the probed signal quality and the readout fidelity.

3.1 Experimental setup

The experimental setup consists mainly of an Oxford Instruments Triton ™ dilution refrigerator with a base temperature of $T_{\text{base}} \approx 20\,\text{mK}$, shown in Fig. 3.1, and a set of instruments allowing for the measurement and control of the studied sample.

The refrigerator is composed mainly of:

— a cryostat

— a control cabinet

— a compressor for the pulse tube refrigerator

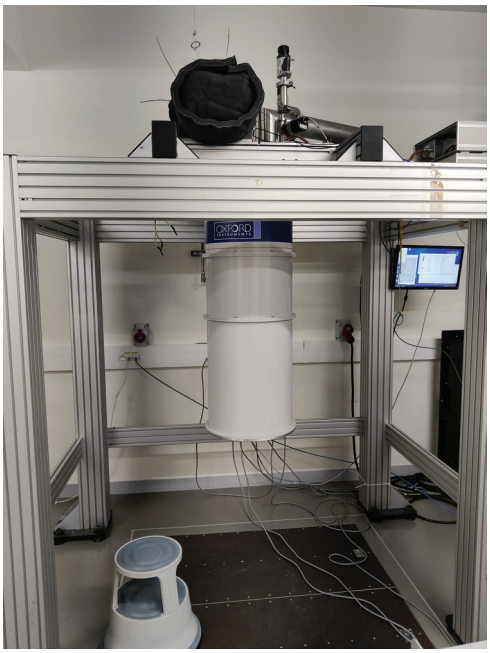

Figure 3.1 – **Oxford Instruments Triton™ dilution refrigerator.** Picture of the used fridge with a base temperature of $T_{\text{base}} \approx 20\,\text{mK}$.

— a compressor for ^{3}He/^{4}He mixture

— ancillary pumps

— a computer based controller (different from the measurement computer)

The sample holder described in Sec. 2.4 is mounted at the bottom of the fridge column, presented in Fig. 3.2, and connected to the cryostat measurement lines.

The cryostat is equipped with 24 noise-filtered DC lines going from the sample to the top of the fridge and connected to a matrix box featuring an electrical switch for each line. A superconducting vector magnet allowing to generate high magnetic fields (up to 6 T in the vertical direction z, and up to 1 T along the x and y axes) is positioned below the mixing-chamber plate while being thermally and mechanically anchored to the 4 K plate.

All of the instruments in the experimental setup are connected to a computer serving as a processing unit ensuring measurement control and data acquisition. Fig. 3.3 shows the measurement circuitry of the experimental setup including the room temperature instruments.

DC voltages are generated by room-temperature digital analog converters (DACs) (Delft IVVI electronics) and filtered at low temperatures by home-made silver epoxy filters and two-stage RC filters, both thermally anchored to the mixing chamber plate of the dilution refrigerator. These signals are applied to the gate electrodes of the devices under study. Source and drain contacts are kept grounded throughout the whole experiments described in Chaps. 4 and 6.

Transport measurements are realised by probing the current flow through the studied sample using the Delft IVVI current-voltage converter. Its analog output is fed to a digital multimeter (DMM) and averaged over the number of power line cycles (NPLC) (typically 2-10 NPLC).

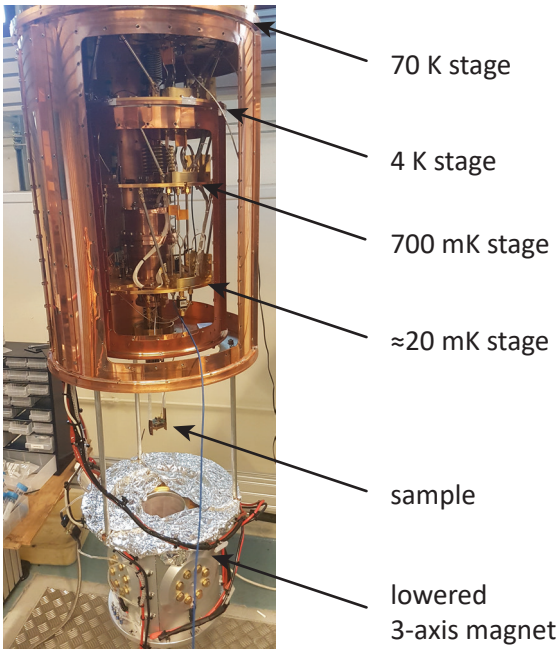

Figure 3.2 – **Open cryostat column.** Picture of the the opened cryostat column showing the different refrigeration stages. The cold finger used to shield ans surround the sample has been removed to get a view of the sample lodging spot. The 3-axis magnet has been lowered to give access to the device.

The reflectometry channel is fed by an Agilent N5181A RF source, which also provides the reference signal of a Zurich Instruments (ZI) ultra high frequency lock-in (UHF-LI) for demodulation. The reflectometry tone is pass-band filtered at room temperature and attenuated at different stages of the fridge for thermalization (see Fig. 3.3). It is added to the DC signal via a bias tee mounted on the sample holder. The reflectometry tank circuit consists of a 220 nH surface-mount inductor (Coilcraft 221XGLB), soldered on the PCB, and a parasitic capacitance C_p ($\lesssim 1$ pF). The reflected signal is separated from the incoming wave by a directional coupler (Mini-circuits ZEDC-15-2B) and amplified at the 4 K stage by a low noise amplifier (Caltech ClTLF1) with 35 dB gain and 6 K noise temperature. The RF excitation power applied to the resonator is constant throughout all the measurements and is set to a value low enough such that the AC-Stark effect is negligible. We estimate $P_\mathrm{ref} \approx -110$ dBm.

One output of the UHF-LI is used in the arbitrary wave generator (AWG) mode to precisely gate the microwave tone delivered by an Agilent E8257D source for coherent spin rotations (Chap. 4) and spectroscopy excitations (Chap. 6). The resulting microwave bursts are added by a triplexer to the readout/manipulation pulses generated by the other UHF-LI channel. The signal then passes through different attenuators and feeds a second bias tee on the board.

The video mode described in Chap. 5 relies on the addition of two fast ramps generated by the AWG module of the UHF-LI to the gate voltages. The superposition of the signals is ensured by the Delft IVVI summing module that we modified in its internal wiring in order to support this functionality.

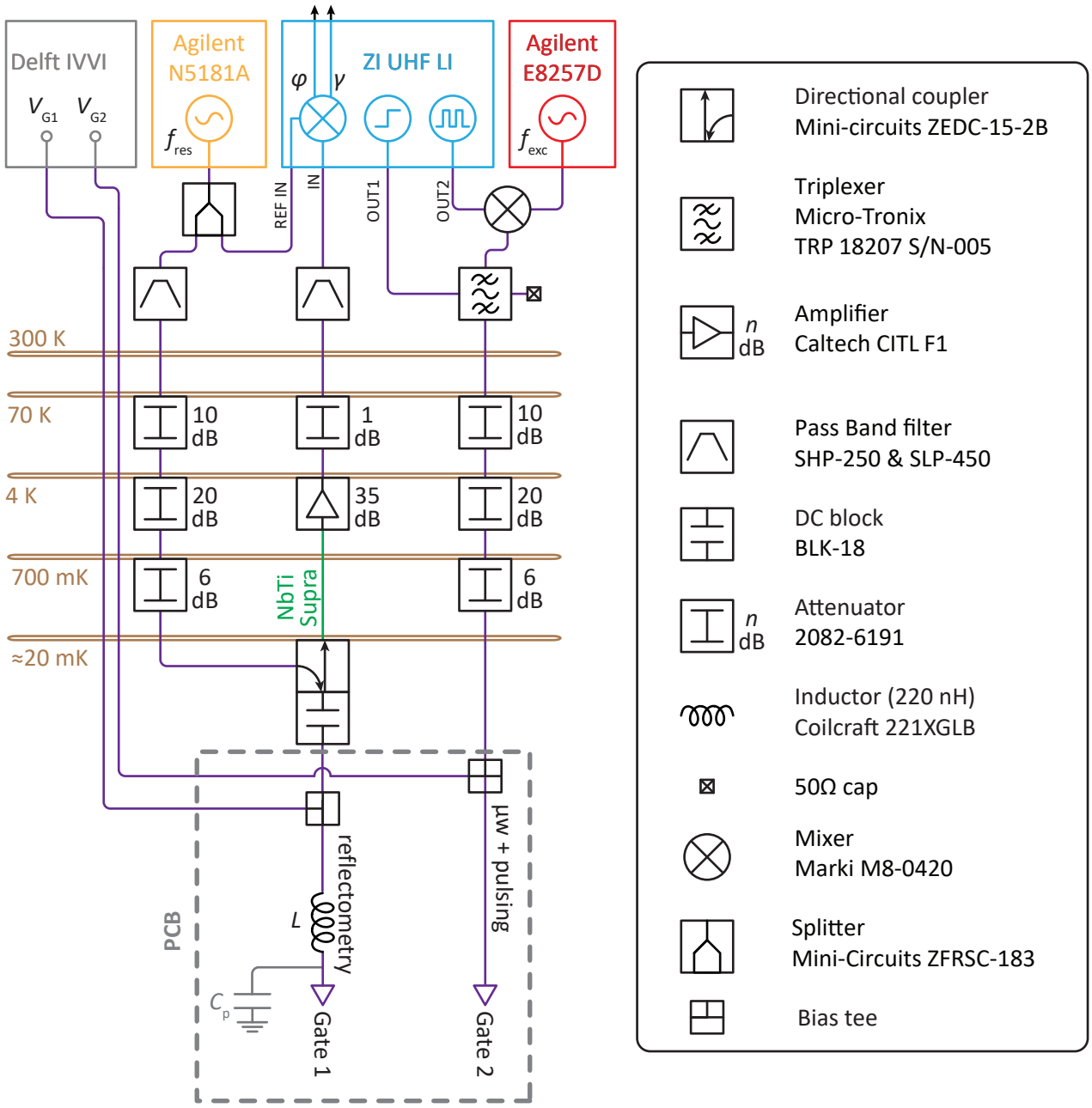

Figure 3.3 – **Schematic of the measurement setup.** The circuitry of the right gate combines DC voltages for DQD electrostatic tuning, fast voltage pulses and EDSR microwave tones. For the left gate, the DC voltage is added to reflectometry radio-frequency signal for dispersive homodyne detection.
For each gate, a bias tee combines a DC component and an AC component: V_{G1} and the reflectometry signal for gate 1, and V_{G2} and the spectroscopy tone for gate 2.

3.2 Resonator characterization

Once the sample is at T_{base}, we start by characterizing the resonator response. Due to variations in the bonding layout and sample holder (PCB) preparation (*e.g.* unavoidable variations in the soldering of the surface-mount components), this response, though more or less comparable, is specific to each {sample + PCB} ensemble. As an example, Fig. 3.4 shows the resonator response for device 2 at base temperature.

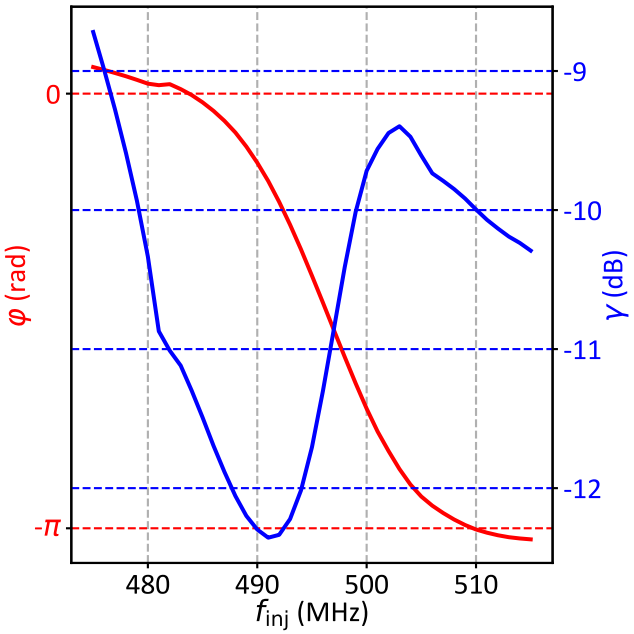

Figure 3.4 – **Resonator characterization for device 2.** Phase response φ and attenuation γ of the LC resonator at base temperature in the case of device 2. We find a resonance frequency $f_{\text{res}} = 497\,\text{MHz}$ and a loaded quality factor $Q_{\text{loaded}} \approx 24$.

By unwrapping the reflected phase φ and removing the linear background, we extract the inflection point marking the resonance at f_{res}. The loaded Q-factor Q_{loaded} is then obtained from [55]:

$$\left.\frac{d\varphi}{df_{\text{inj}}}\right|_{f_{\text{inj}}=f_{\text{res}}} = \frac{-4Q_{\text{loaded}}}{f_{\text{res}}}, \tag{3.1}$$

where f_{inj} is the injected frequency used to excite the resonator.

Once the resonance frequency is extracted, the parasitic capacitance C_{p} forming the tank circuit along with the surface mount inductor L can be calculated using:

$$C_{\text{p}} = \frac{1}{(2\pi f_{\text{res}}\sqrt{L})^2}. \tag{3.2}$$

The extracted values for each device used in this thesis are detailed in Table 3.1.

3.3 Signal to noise ratio & fidelity

Before engaging in any complex measurements or experiments, it is judicious to be able to state if the signal at hand is good enough. Starting with a small signal with a large relative

	device 1 (Chap. 4)	**device 2** (Chap. 6)	**device 3** (Chap. 6)
$f_{\mathbf{res}}$	339 MHz	497 MHz	560 MHz
L	220 nH	220 nH	220 nH
$C_{\mathbf{p}}$	1 pF	466 fF	367 fF
$Q_{\mathbf{loaded}}$	18	24	54

Table 3.1 – **Extracted resonators values.**

noise level for example makes it almost sure that the future complicated measurements (qubit manipulation, readout with pulsing, photon induced transitions, ...) will fail to provide a detectable signal level that could stand out from noise. In the following we discuss how to quantify the signal quality and its impact on qubit quality (fidelity).

3.3.1 Signal to noise ratio

Signal to noise ratio (SNR) is an indicator of the information transmission quality. It compares the signal level to the background noise. In the context of qubit measurements using a reflectometry technique, SNR can also be translated into charge sensitivity [117, 1].

SNR is a dimensionless quantity and is by definition the ratio between the signal power P_{S} and the background noise power P_{N}:

$$\mathrm{SNR} = \frac{\mathrm{P_S}}{\mathrm{P_N}}. \tag{3.3}$$

SNR may also be expressed in decibels in order to better capture wide dynamic range of signals:

$$\mathrm{SNR_{dB}} = 10 \cdot \log_{10}(\mathrm{SNR}). \tag{3.4}$$

Since we always measure signals across the same impedance, the square amplitudes of signal V_{S} and noise V_{N} can be compared to yield the SNR value:

$$\mathrm{SNR} = \left(\frac{\mathrm{V_S}}{\mathrm{V_N}}\right)^2. \tag{3.5}$$

Two methods can be used to extract the SNR value. One relies on side-band modulation and the other, more straightforward, on a direct measurement in the IQ plane.

Side band modulation method

One way of evaluating the SNR value for a phase signal on a given ICT consists of adding a low frequency modulation on top of the injected carrier signal (resonator excitation) and look at the side bands generated in the frequency spectrum [117, 1]. As a working point for this technique, we take the side of the phase dip associated with an ICT, where the signal amplitude corresponds to half of the total dip height. The modulation signal frequency f_{mod} can be arbitrarily chosen as long as it remains small compared to the carrier frequency f_{inj} and its power P_{mod} should be set to the minimal value allowing for a full sweep of the ICT signal.

The described modulation results in a variation of the phase signal amplitude at the modulation frequency (hence the choice to sit on a point where the signal slope is maximal). This variation is quantified using the fast Fourier transform (FFT) of the reflected signal computed

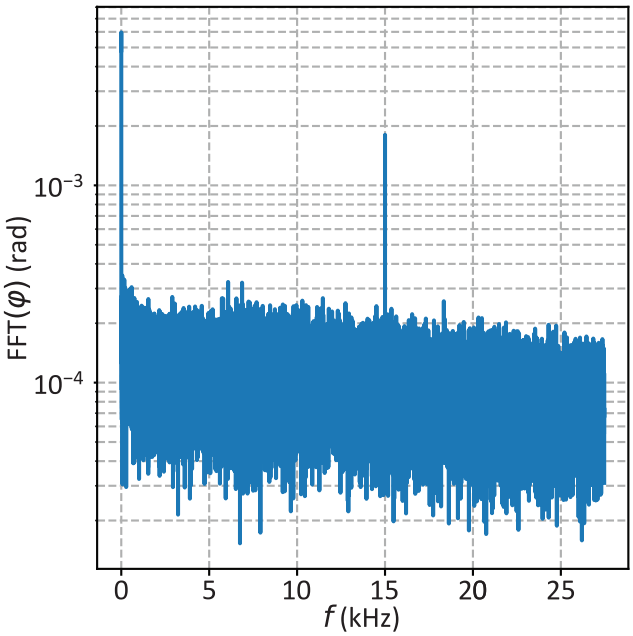

Figure 3.5 – **FFT of the reflected signal in the presence of a small additional modulation.** The frequency axis is shifted so that the frequency origin corresponds to the carrier frequency f_{inj} which is maintained at the resonance frequency of the oscillator ($f_{\text{inj}} = f_{\text{res}}$). A side-band appearing at $f_{\text{mod}} = 15\,\text{kHz}$ is used to compute the SNR value.

in the phase φ domain as shown in Fig. 3.5.

Using the ZI UHF-LI, the limit frequency for the FFT measurement f_{max} is directly related to the demodulator data transfer rate (DTR) as follows:

$$f_{\text{max}} = \frac{\text{DTR}}{2}. \tag{3.6}$$

As for the FFT resolution δf, it could be deduced from:

$$\delta f = \frac{2 \times f_{\text{max}}}{N}, \tag{3.7}$$

where N is the number of points to be set for the FFT measurement.

We see the appearance of a side-band on the FFT graph and the SNR value can be found following:

$$\text{SNR} = 10 \cdot \log_{10}\left(\frac{\text{side band amplitude}}{\text{noise floor level}}\right)^2. \tag{3.8}$$

IQ plane method

We consider two positions in the stability diagram, one being “ON” and the other “OFF" the ICT. For each position, we measure N values of the UHF-LI demodulator response corresponding to in-phase (I coordinates) and quadrature (Q coordinates) components. Fig. 3.6 gives an example of such a measurement.

Using this method, the SNR value is given by [71]:

$$\text{SNR} = \frac{\text{d}^2}{\frac{1}{2}(\sigma^2_{\text{ON}} + \sigma^2_{\text{OFF}})}, \tag{3.9}$$

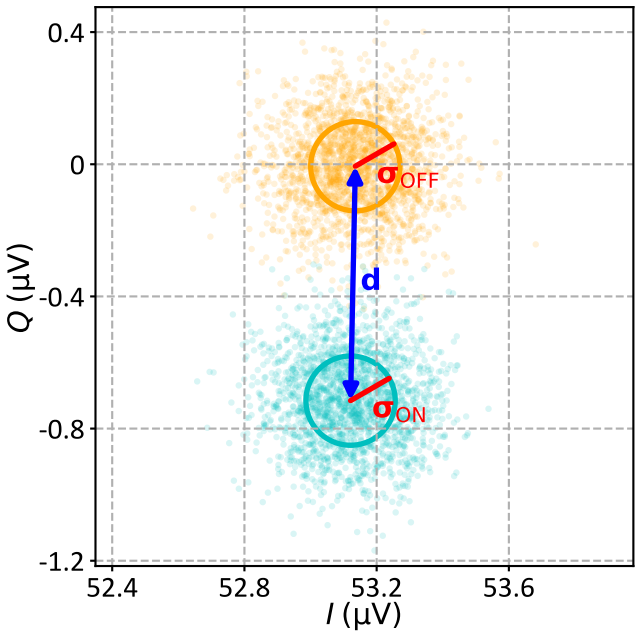

Figure 3.6 – **IQ plane measurements taken on and off an ICT.** Scatter plot of $N = 1000$ points for each position: "ON" (cyan) and "OFF" (orange) the ICT. A circle centered on the "OFF" ("ON") points distribution center and with a radius of σ_{OFF} (σ_{ON}), its standard deviation, is drawn. The distance between the centers of these two circles is d. SNR = 1 corresponds to the case where the two circle come in contact, *i.e.* $d = \sigma_{\text{ON}} + \sigma_{\text{OFF}}$.

where σ_{OFF} (σ_{ON}) is the standard deviation characterizing the "OFF" ("ON") points distribution and d the distance separating the centers of these two distributions in the IQ plane (see Fig. 3.6).

Signal to noise ratio dependencies

When the carrier signal power P_{inj} is high, it leads to a broadening of the interdot feature as proved in Fig. 3.7. Therefore, investigating how SNR depends on P_{inj} is not useful in the high-power regime. We choose then P_{inj} to be the highest value such as we have no feature broadening. This condition yields the best SNR with no interdot signal broadening. For lower P_{inj}, while the linewidth remains unchanged, the SNR degrades because the signal amplitude decreases relative to the noise floor set by the cryogenic amplifier.

When using the side band modulation method, the SNR depends on the modulation signal power P_{mod} as presented by Fig. 3.8. In fact, since we are sitting on the side on an interdot phase dip, the reflected phase signal has maximal sensitivity to gate-voltage detuning, and phase response increases with the amplitude of the signal modulation, which is proportional to $\sqrt{P_{\text{mod}}}$. The maximal phase response is achieved when the working point oscillates between the peak and the valley of the signal. This is clearly shown in Fig. 3.9. Once the P_{mod} starts to broaden the probed transition, the separation between these maximum points increase. These results are very similar to a recently conducted study [1].

When studying the dependence of SNR on the frequency f_{mod} of the modulation signal, the maximal FFT scan frequency depends on the UHF-LI DTR according to Eq. (3.6). The UHF-LI cannot support high values of DTR for a continuous trigger mode (acquiring all the time). Hence, the extraction of SNR values for modulation frequencies higher than 400 kHz was not possible. The impact of f_{mod} on the SNR has been shown [117] to be related to the

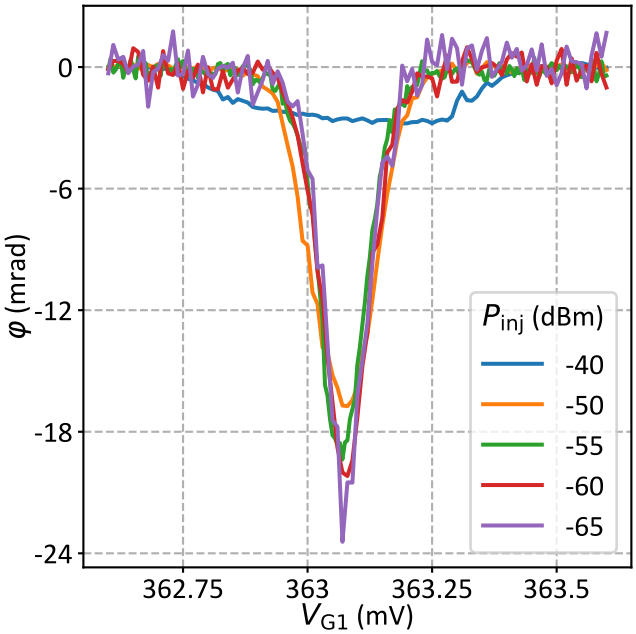

Figure 3.7 – **Injected power effect on interdot signal.** ICT phase signal as a function of gate voltage V_{G1} for various injected carrier powers P_{inj}. The interdot signal starts broadening at -50 dBm.

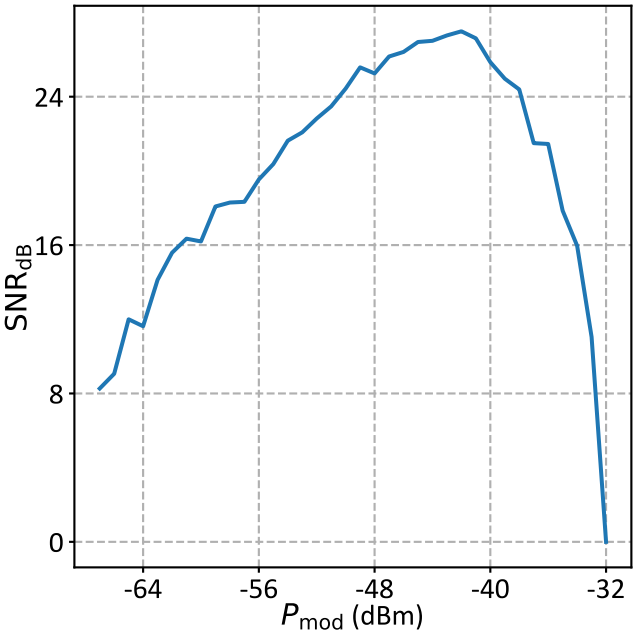

Figure 3.8 – **Modulation power impact on SNR.** SNR_{dB} as a function of the modulation signal power P_{mod}. The maximal value is obtained when the modulation power is enough to make the working point oscillate between the peak and the valley of the probed phase signal signal.

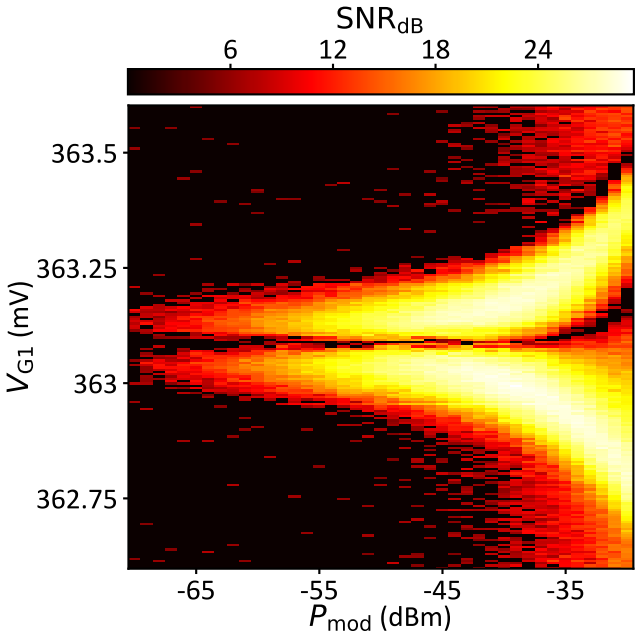

Figure 3.9 – **SNR as a function of V_{G1} and the modulation signal power P_{mod}.** For a given modulation power, two SNR maxima appear with a gate voltage whose separation that increases as P_{mod} is increased. Their positions corresponds to the V_{G1} points of maximum slope at either side of the ICT signal. The increasing separation with increasing P_{mod} suggests that the transition is being broadened by the modulation signal.

bandwidth of the resonator. Thus, the SNR value is expected to be constant and maximal for modulation frequencies included in the resonator bandwidth and then starts to deteriorate.

As expected, the SNR signal is maximal around the resonator resonance frequency as we could conclude from Fig. 3.10. By sitting at the resonance frequency $f_{inj} = f_{res}$, the system finds itself at the most sensitive working point.

Another important component to take into account is the demodulator low pass filter integration time τ_{int}. The higher the integration time is, the more noise is filtered leading to a higher SNR as highlighted in Fig. 3.11. While increasing τ_{int} results in a better measured signal, it extends the time necessary to accomplish the measurement. A fine balance should therefore be found between how fast one would want to measure and its effect on the SNR.

3.3.2 Readout fidelity

Given two quantum states, $|\uparrow\rangle$ and $|\downarrow\rangle$, the so-called readout fidelity is an indicator of how good a measurement differentiates between these states. It expresses the possibility to measure correctly the quantum state. In a certain sense, fidelity forms the bridge between the neat high level flawless implementation and the messy reality of a fallible quantum hardware.

For a set of N measurements of the quantum state, we fit the histogram of measurement results to overlapping Gaussian distributions, which we show for example in Fig. 3.12. The $|\uparrow\rangle$ ($|\downarrow\rangle$) distribution is centered around the phase value $\varphi_\uparrow$ ($\varphi_\downarrow$) and have a standard deviation σ. These distributions are separated by a distance d and cross at φ_{int}. For the sake of simplicity, we consider that both measured quantum states have the same σ and perfect spin-to-charge

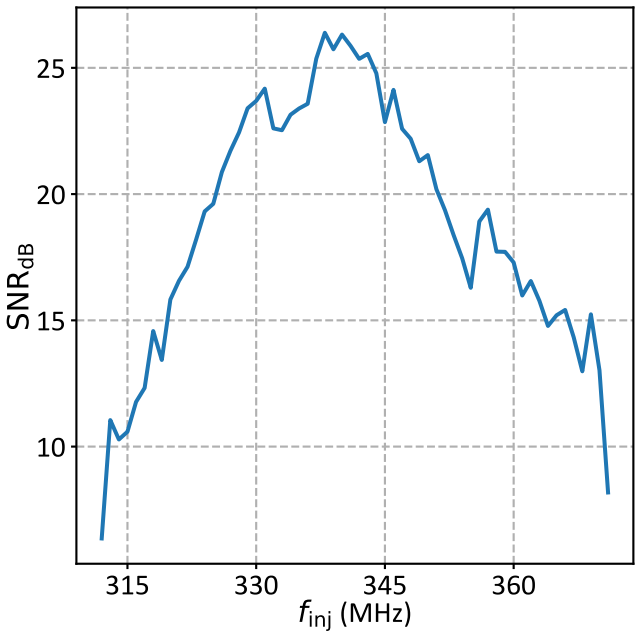

Figure 3.10 – **Injected frequency influence on SNR.** SNR_{dB} as a function of the injected frequency f_{inj}. The curve exhibits a maxima when injected power matches the resonance frequency of the tank circuit $f_{inj} = f_{res}$.

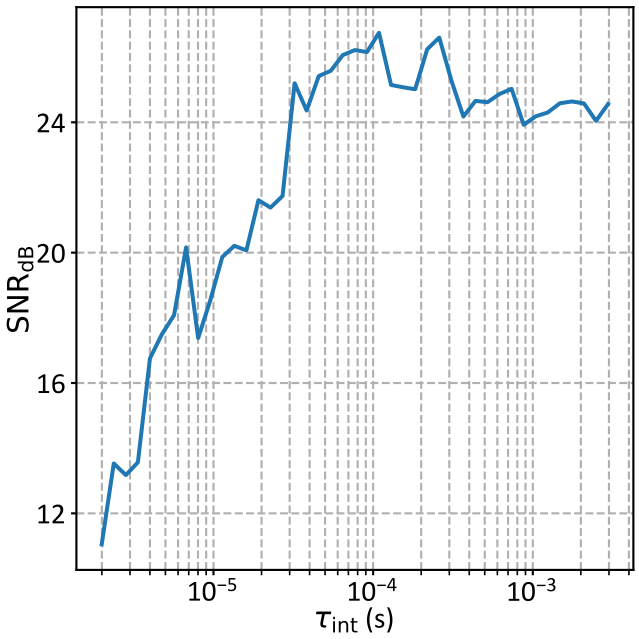

Figure 3.11 – **SNR as a function of the demodulator low-pass filter integration time.** The less the signal is integrated, the higher the signal noise is and signal quality deteriorates.

conversion.

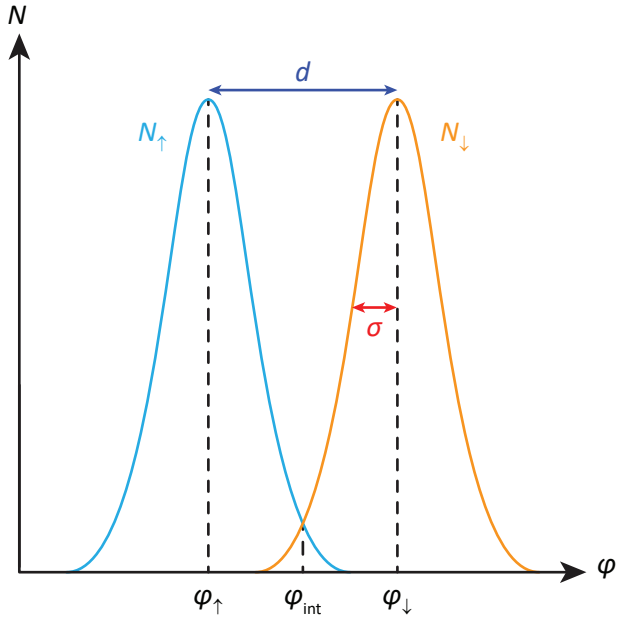

Figure 3.12 – **Detected events number N distribution of up and down states measurements.** Each Gaussian, characterized by a standard deviation σ, simulates measurement histograms for the states $|\uparrow\rangle$ (cyan) and $|\downarrow\rangle$ (orange). The two distribution are separated by a distance d between the centers $\varphi_\uparrow$ and $\varphi_\downarrow$ and they intersect at φ_{int}.

The fidelities of the $|\downarrow\rangle$ and $|\uparrow\rangle$ states are given by [8]:

$$\mathcal{F}_\downarrow = 1 - \int_{-\infty}^{\varphi_{\text{int}}} N_\downarrow \, d\varphi, \tag{3.10}$$

$$\mathcal{F}_\uparrow = 1 - \int_{\varphi_{\text{int}}}^{+\infty} N_\uparrow \, d\varphi. \tag{3.11}$$

The resulting fidelity will be then [70]:

$$\begin{aligned} \mathcal{F} &= \frac{\mathcal{F}_\downarrow + \mathcal{F}_\uparrow}{2} \\ &= 1 - \frac{1}{2}\left(\int_{-\infty}^{\varphi_{\text{int}}} N_\downarrow \, d\varphi + \int_{\varphi_{\text{int}}}^{+\infty} N_\uparrow \, d\varphi \right). \end{aligned} \tag{3.12}$$

If we consider Gaussian distributions for the up and down states as follows:

$$N_{\downarrow(\uparrow)} = \frac{1}{\sigma\sqrt{2\pi}} e^{-\frac{\left(\varphi - \varphi_{\downarrow(\uparrow)}\right)^2}{2\sigma^2}}, \tag{3.13}$$

we end up with a simpler expression for the fidelity:

$$\begin{aligned} \mathcal{F} &= \frac{1}{2}\left(-\operatorname{erf}\left(\frac{\varphi_{\text{int}} - \varphi_\downarrow}{\sqrt{2}\sigma} \right) + \operatorname{erf}\left(\frac{\varphi_{\text{int}} - \varphi_\uparrow}{\sqrt{2}\sigma} \right) \right) \\ &= \operatorname{erf}\left(\frac{d}{2\sqrt{2}\sigma} \right), \end{aligned} \tag{3.14}$$

where erf denotes the Gauss error function.

Eq. (3.9) lets us then link $\mathcal{F}$ to the SNR value as:

$$\mathcal{F} = \mathrm{erf}\left(\frac{\sqrt{\mathrm{SNR}}}{2\sqrt{2}}\right). \tag{3.15}$$

Even though we took a simple model for our calculations, Eq. (3.15) remains a very good estimate for the fidelity using the SNR value. To better illustrate this, Fig. 3.13 shows the evolution of the qubit error $(1-\mathcal{F})$ as a function of SNR. A quick approximation, even for more complicated situations, yields then a fidelity of 99 % for SNR $\simeq$ 26, and a fidelity of 99.9 % for SNR $\simeq$ 43.

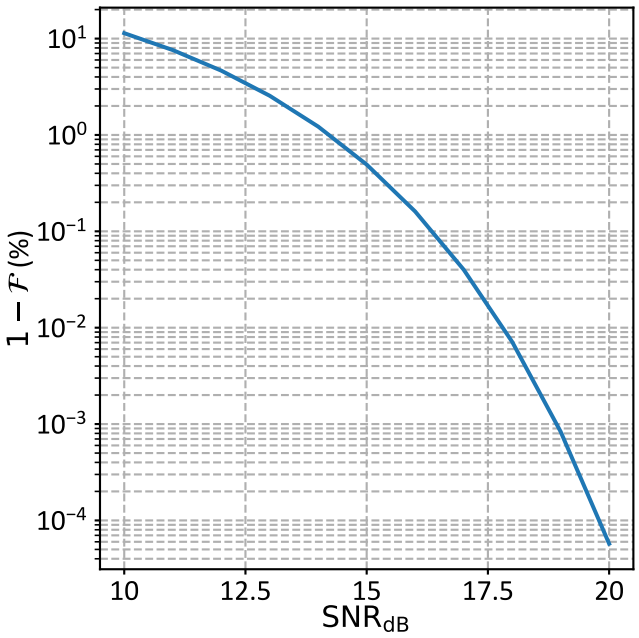

Figure 3.13 – **Qubit error.** Readout error as a function of $\mathrm{SNR_{dB}}$.

Takeaway messages:

- The studied samples are held at a temperature $T_{\text{base}} \approx 20\,\text{mK}$ using a dilution refrigerator and a set of instruments assures their readout and manipulation.
- The experimental setup allows at the same time for transport measurements, by means of the Delft IVVI IV converter, as well as reflectometry measurements, using the ZI UHF-LI.
- The resonator characteristics (f_{res}, Q_{loaded}, C_{p}) are extracted by studying its phase or/and amplitude response to the injected signal frequency f_{inj}.
- SNR is a measure of the signal quality and is directly linked to qubit readout fidelity.

Chapter 4

Gate-reflectometry dispersive readout and coherent control of a hole spin qubit in silicon

An experiment is a question which science poses to Nature, and a measurement is the recording of Nature's answer.

Max PLANCK

Contents

Silicon spin qubits have emerged as a promising path to large-scale quantum processors. In this prospect, the development of scalable qubit readout schemes involving a minimal device overhead is a compelling step. Here we report the implementation of gate-coupled RF reflectometry for the dispersive readout of a fully functional spin qubit device. We use a p-type double-gate transistor made using industry-standard silicon technology. Two gates tune an isolated hole DQD, and two distinct electric RF tones (one per gate) allow spin manipulation and dispersive readout. The qubit state is measured through the phase response of a lumped element resonator to spin-selective interdot tunneling. The demonstrated qubit readout scheme requires no coupling to a Fermi reservoir, thereby offering a compact and potentially scalable solution whose operation may be extended above 1 K. We assess hole single spin dynamics and show coherent spin control, validating a protocol for complete qubit characterization exploitable in more complex architectures.

The work described in this chapter has led to a recently published article [26].

4.1 Methods

The experiment in this chapter is carried out on device 1 described in Sec. 2.3. The device has two parallel top gates, gate 1 and gate 2, wrapping an etched Si nanowire channel. At low temperature ($\approx 20\,\mathrm{mK}$), DC voltages V_{G1} and V_{G2} are applied to these gates to induce two closely spaced hole quantum dots. The "Control" gate, gate 2, delivers also sub-μs pulses and microwave excitation in the GHz range to manipulate the qubit. The "Readout" gate, gate 1, is wire-bonded to a surface-mount inductor forming along with a parasitic capacitance and the device impedance a tank circuit resonating at $f_0 = 339\,\mathrm{MHz}$ (see full characterization in Sec. 3.2). We excite the resonator input at $f_{res} = f_0$ and power $P_{res} \approx -110\,\mathrm{dBm}$. We measure the phase variation φ of the reflected signal isolated from the incoming wave by a directional coupler, amplified by 35 dB at 4 K and demodulated to baseband using homodyne detection. The resonant frequency f_0 undergoes a dispersive shift according to the state of the qubit as explained in Sec. 1.4. The full measurement circuit is reported in Sec. 3.1.

4.2 Charge stability diagram

To determine the charge stability diagram of our DQD, we probe the phase response of the resonator while sweeping the DC gate voltages V_{G1} and V_{G2}. A series of nearly horizontal parallel lines are visible in the left panel of Fig. 4.1. These lines repeat quite regularly from metallic DQDs to depletion, and even when the silicon channel is completely closed (data not shown). Consequently, we speculate that these features are related to the charging of objects extrinsic to the channel. On top of this background, most of the short diagonal cuts on the yellow background are interdot transition lines. A zoom into the area highlighted by the blue square leads to the diagonal ridge in the right graph of Fig. 4.1 which denotes the interdot charge transition we shall focus on hereafter.

In the many-hole (quasi-metallic) regime, the typical gate voltage between two charge states is about 25 mV. This value is consistent with other experiments on similar samples [89, 27]. Away from the many hole regime, the interdot lines are unevenly spaced, as it is the case in Fig. 4.1. Importantly, for interdot tunnel couplings of few GHz (like the one under study), the interdot transition lines are quite thin in gate voltage, and are difficult to resolve in large maps obtained with large voltage steps (a point that will be addressed in Chap. 5). We use the threshold voltages at room temperature of the two gates and the addition voltage of the many hole regime for a rough estimation of the absolute filling of the dots. We obtain around 5 and 10-20 holes in the left (mainly controlled by V_{G1}) and right dot (mainly controlled by V_{G2}), respectively.

Along the ICT, the electrochemical potentials of the two dots line up enabling the shuttling of a hole charge from one dot to the other. This results in a phase variation in the reflected signal. Quantitatively, φ is proportional to the quantum capacitance associated with the gate voltage dependence of the energy levels involved in the interdot charge transition. Interdot tunnel coupling results in the formation of molecular bonding (+) and anti-bonding (−) states with energy levels E_+ and E_-, respectively. These states have opposite quantum capacitance since $C_{Q\pm} = -\alpha^2(\partial^2 E_\pm/\partial\varepsilon^2)$ [28]. Here, ε is the gate-voltage detuning along a given line crossing the interdot charge transition boundary, and α is a lever-arm parameter relating ε to the energy difference between the electrochemical potentials of the two dots (we estimate $\alpha \simeq 0.58\,\mathrm{eV/V}$ along the detuning line in Fig. 4.1. The width of the phase ridge, once translated into energy, gives the interdot tunnel coupling t.

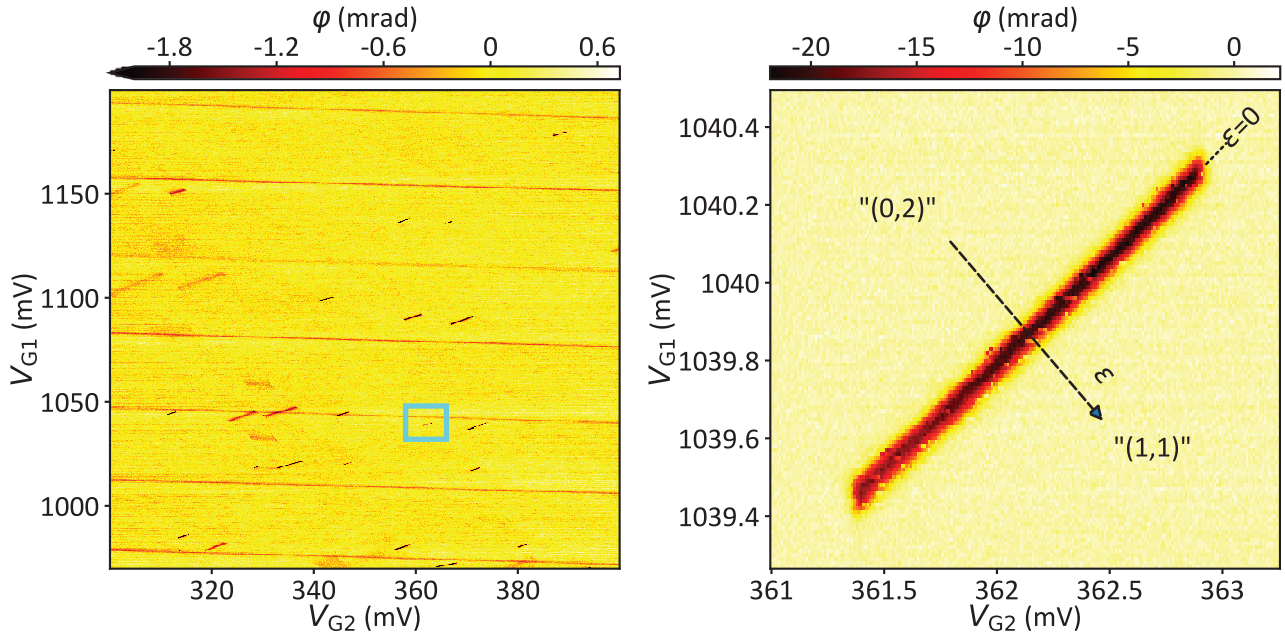

Figure 4.1 – **Charge stability diagram of device 1.** Phase shift of the reflected signal as a function of V_{G2} and V_{G1} near the interdot transition line under study (right) and broadly around it (left). As V_{G1} approaches the gate voltage threshold, ICTs are unequally placed. The blue square in the left graph denotes the zoomed-in area in the right panel. The dashed arrow indicates ε detuning axis.

A comprehensive description of the experimental phase signal is achieved by considering the excited levels of the DQD as partially populated. Importantly, we make the assumption that the average occupation probability of the available excited states are populated according to a Boltzmann distribution with an effective temperature T_{eff}, which is used as a free parameter. Each state leads to an averaged phase signal:

$$\langle\varphi\rangle_i = \varphi_i|_{T=0} \cdot \frac{e^{-\frac{E_i}{k_B T_{\text{eff}}}}}{Z}, \tag{4.1}$$

where $\varphi_i|_{T=0}$ is proportional to the quantum capacitance of the state with energy E_i in the 0 K limit, k_B the Boltzmann constant, T_{eff} an effective temperature, and Z is the partition function over the states. The measured phase signal then is $\varphi = \sum_i \langle\varphi\rangle_i$ [123].

The coupling term t is estimated from a detuning trace at $B = 0$ T. The full width at half maximum (FWHM) of the phase interdot ridge is linked to the effective temperature T_{eff} [93]. Two limiting situations are envisaged. At low temperature, $k_B T_{\text{eff}} < t/10$, the width of the interdot signal is set by the tunnel coupling to $\sim 3t$. Here, just the ground singlet is populated. In the opposite limit of high temperature, $k_B T_{\text{eff}} > 2t$, the threefold triplet and both bonding and anti-bonding singlet are thermally populated. By sweeping T_{eff}, the magnitude of the interdot resonance drops, but the FWHM saturates at $\sim 4t$. In the intermediate regime, the FWHM increases progressively with T_{eff}, up to the saturation point occurring at $k_B T_{\text{eff}} \simeq 2t$. Furthermore, this demonstrates that the FWHM allows to estimate t in the $(3t, 4t)$ range whatever the temperature is. This distinguishes dispersive readout from charge sensing (especially when $k_B T_{\text{eff}} > 2t$), as the resonator sensitivity is ultimately constrained to the avoided crossings in the energy level diagram. Fits to the interdot detuning phase shift yield $t = 8.5\,\mu$eV and

$t = 6.4\,\mu$eV in the low and high temperature limit, respectively.

4.3 Magnetospectroscopy of the double quantum dot

The total charge parity and the spin character of the DQD states can be determined from the evolution of the ICT in an applied magnetic field B [123]. Fig. 4.2 shows the B_y dependence of the phase signal at the detuning line indicated in Fig. 4.1. Four representative traces taken from this plot are shown in Fig. 4.4. The interdot phase signal progressively drops with B_y. At $B_y = 0.35\,$T the line profile is slightly asymmetric, while a double-peak structure emerges at $B = 0.46\,$T. The two peaks move apart and weaken by further increasing B_y, as revealed by the trace at $B = 0.85\,$T.

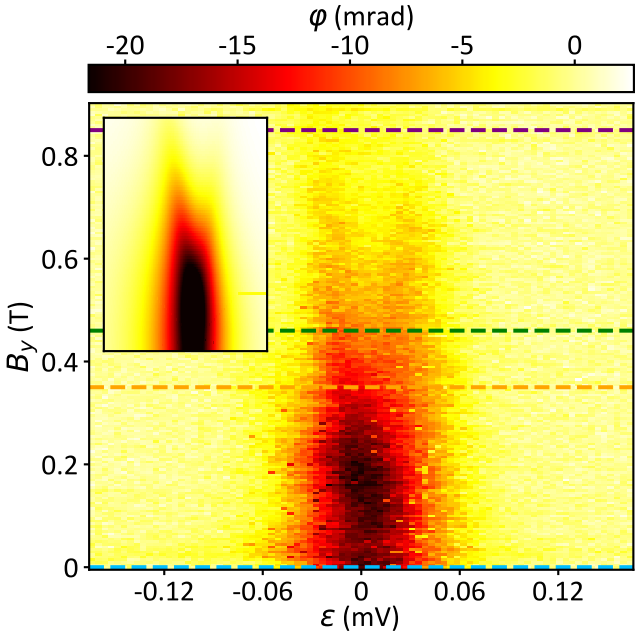

Figure 4.2 – **Magnetospectroscopy of the ICT under study.** Interdot dispersive signal as a function of the magnetic field B_y oriented along the nanowire axis. The phase response diminishes with B_y, denoting an ICT of (0,2) $\leftrightarrow$ (1,1) type. Inset: theoretical prediction of the dispersive response for a DQD model taking into account thermally activated state populations.

The observed behavior can be understood in terms of an interdot charge transition with an even number of holes in the DQD, in a scenario equivalent to a (0,2) $\leftrightarrow$ (1,1) transition. We shall then refer to a "(0,2)" and a "(1,1)" state, even if the actual number of confined holes is larger as mentioned earlier. The ε dependence of the DQD states at finite B is presented in the left panel of Fig. 4.3. Deeply in the positive detuning regime, different g-factors for the left (g_1) and the right dot (g_2) result in four non-degenerate (1,1) levels corresponding to the following spin states: $|\downarrow\downarrow\rangle$, $|\uparrow\downarrow\rangle$, $|\downarrow\uparrow\rangle$ and $|\uparrow\uparrow\rangle$ [98, 99, 109]. At large negative detuning, the ground state is a spin-singlet state $S(0,2)$ and the triplet states $T(0,2)$ lie high up in energy. Around zero detuning, the $|\uparrow\downarrow\rangle$, $|\downarrow\uparrow\rangle$ states hybridize with the $S(0,2)$ state forming an unpolarized triplet $\mathrm{T}_0(1,1)$ and two molecular singlets, S_g and S_e, with bonding and anti-bonding character, respectively.

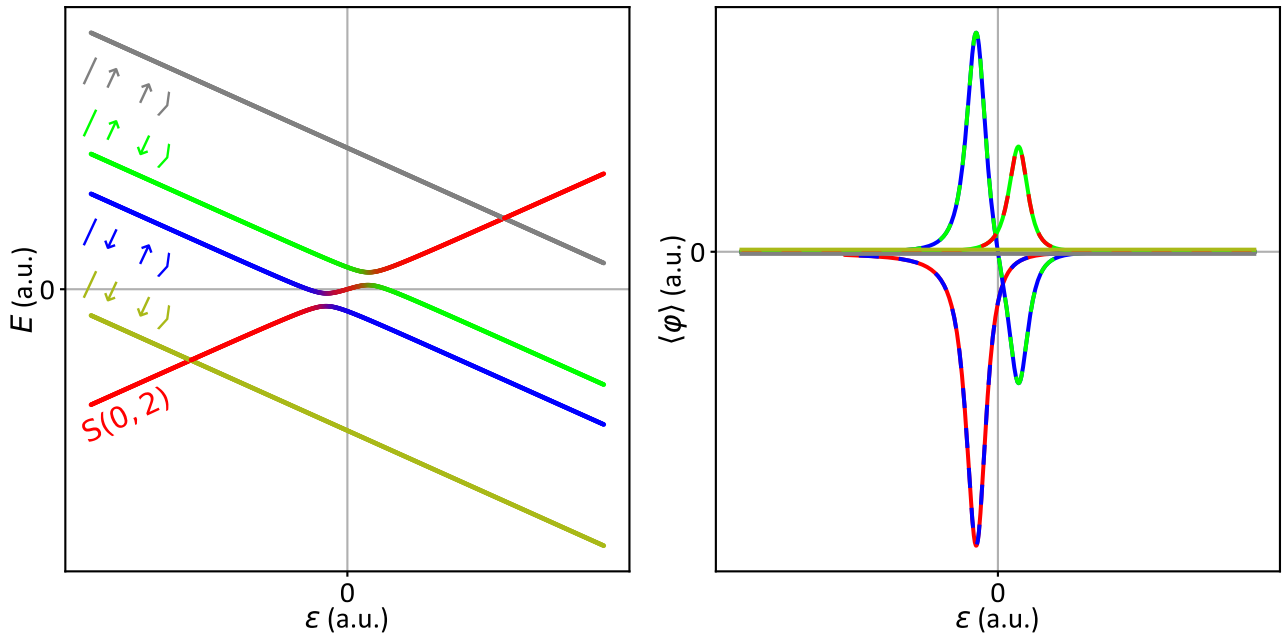

Figure 4.3 – **Energy diagram and resulting phase response.** Schematic of the DQD energy levels close to a (0,2) ↔ (1,1) transition at finite B and for $|g_1 - g_2| = 0.5$ (left panel), and thermally-averaged phase response $\langle\varphi\rangle$ with $T_{\text{eff}} = 0.25\,\text{K}$ (right panel). $\langle\varphi\rangle$ is second derivative of the energy-level dispersion of each state of the left graph, weighted by the Boltzmann occupation probability. The alternating colors of the phase signal match the state colors.

The spin-orbit transition matrix elements are supposed weak compared to t and the Zeeman terms. Sizable spin-flip tunnelling terms would lead to a dispersive signal with a strong magnetic field dependence. We found no evidence of the corresponding dispersive signals in the magnetospectroscopy data.

We use the spectrum of Fig. 4.3 to model the evolution of the interdot phase signal in Fig. 4.2 (see Sec. 1.1.3 for more details). The right panel shows $\langle\varphi\rangle_i$ as a function of ε for $T_{\text{eff}} = 250\,\text{mK}$. The spin polarized triplet states $\text{T}_-(1,1)$ and $\text{T}_+(1,1)$ (*i.e.* $|\downarrow\downarrow\rangle$ and $|\uparrow\uparrow\rangle$, respectively) are linear in ε and, therefore, they do not cause any finite phase shift. S_g, S_e, and $\text{T}_0(1,1)$, on the other hand, possess a curvature and are sensed by the reflectometry apparatus. We note that the phase signal for $\text{T}_0(1,1)$ has a peak-dip line shape whose minimum lies at positive ε (dashed blue/green trace), partly counterbalanced by the positive phase signal due to S_e. The S_g state causes a pronounced dip at negative ε (dashed blue/red trace), dominating over the peak component of $\text{T}_0(1,1)$. The overall net result is a phase signal with an asymmetric double-dip structure consistent with our experimental observation.

This simple model, with the chosen $T_{\text{eff}} = 250\,\text{mK}$, qualitatively reproduces the emergence of the double-dip structure at $B_y \sim 0.4\,\text{T}$, as well as its gradual suppression at higher B_y, as shown in the inset to Fig. 4.2 and in Fig. 4.4 (increasing the Zeeman energy results in the depopulation of the S_g and $\text{T}_0(1,1)$ excited states in favor of the $\text{T}_-(1,1)$ ground state, for which $\varphi = 0$). The parameters used for the simulations are $g_1 = 1.52$, $g_2 = 2.02$ and $t = 6\,\mu\text{eV}$.

Fast excitations/relaxations in the singlet manifold may contribute to the DQD phase response through the tunnel capacitance [93]. However, if such nonadiabatic processes are slow ($\sim 100\,\text{MHz}$) compared to the probing frequency f_res, the tunnel capacitance is small with respect to the quantum capacitance. On the other hand, with fast charge relaxations ($\sim 1\,\text{GHz}$)

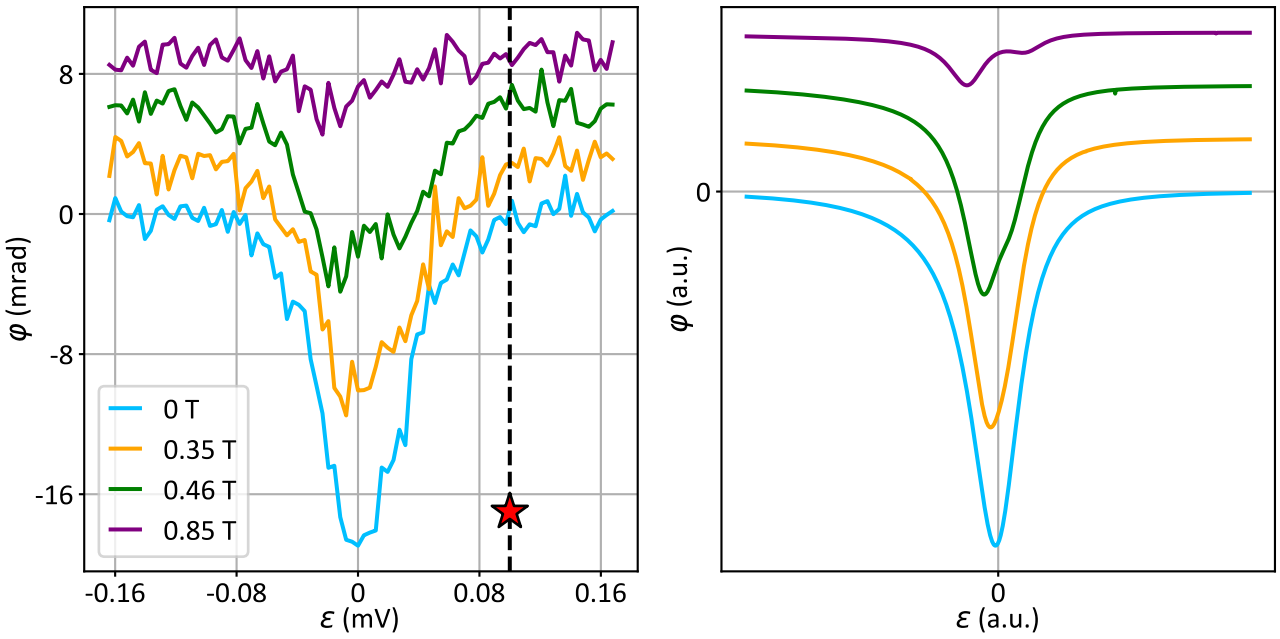

Figure 4.4 – **Phase shift qualitative simulation.** Line cuts of the plot in Fig. 4.2 at the position of the dashed lines (left) and corresponding qualitative phase shift resulting from the sum of all $\langle\varphi\rangle$ from the right panel of Fig. 4.3 (right). Data are offset for clarity. A double-peak structure emerges at sufficiently high B_y in qualitative agreement with the experimental data.

the interdot ridge would have lineshape and width not compatible with the magnetic field evolution reported Fig. 4.2.

Now that we have elucidated the energy level structure of the DQD, we can discuss the operation of the device as a single-hole spin qubit with electrical control and dispersive readout.

4.4 Electric-dipole spin resonance detection

EDSR [89, 27, 139] is induced by a microwave voltage modulation applied to gate 2 (see Sec. 1.3 for more details). To detect EDSR dispersively, the resonating states must have different quantum capacitances. The DQD is initially tuned to the position of the red star in Fig. 4.4, where the DQD is in a "shallow" (1,1) configuration, *i.e.* close to the boundary with the (0,2) charge state.

Fig. 4.5 shows the dispersive measurement of an EDSR line. The microwave gate modulation of frequency f_{exc} is applied continuously and B is oriented along the nanowire axis (y-axis). We ascribe the resonance line to a second harmonic driving process where $2hf_{\text{exc}} = g\mu_B B_y$ (h the Planck's constant, μ_B the Bohr magneton and g the effective hole g-factor). From this resonance condition we extract $g = 1.735 \pm 0.002$, in agreement with previous works [89, 27]. The first harmonic signal,is shown in the right panel of Fig. 4.5. Though both first and second harmonic excitations can be expected [120], the first harmonic EDSR line is unexpectedly weaker. A comparison of the two signal intensities requires the knowledge of many parameters (relaxation rate, microwave power at the sample, *etc.*) and calls for deeper investigations.

The acquired EDSR signal is not satisfactory along the y-direction and would potentially

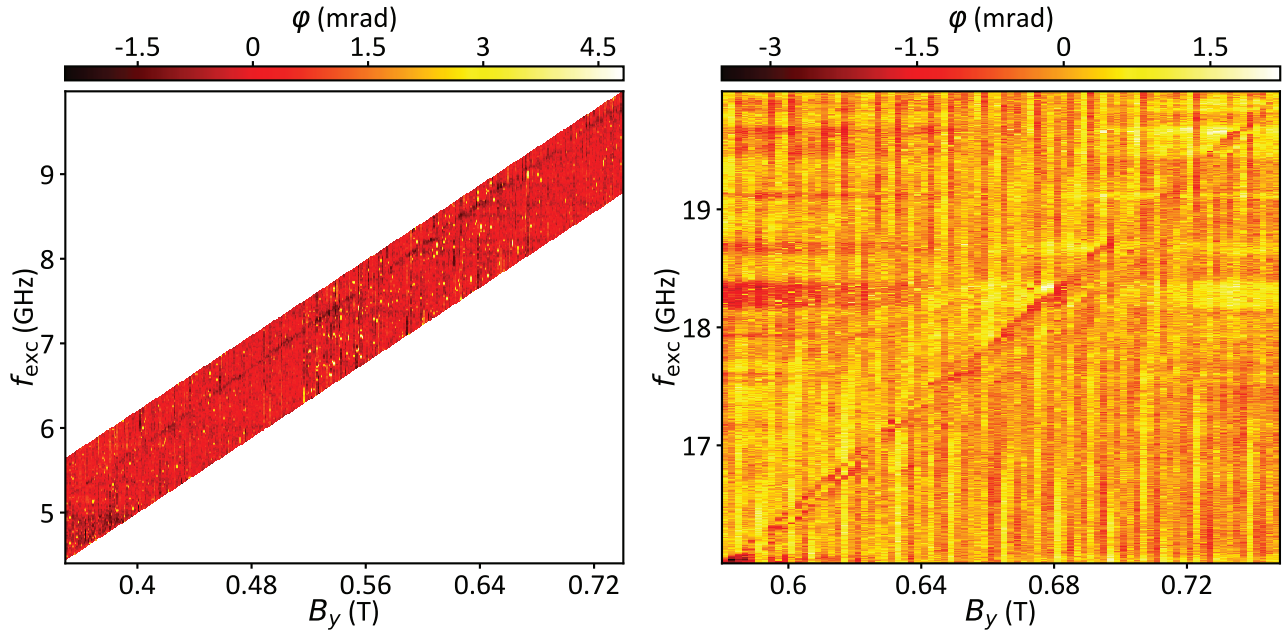

Figure 4.5 – **EDSR detection.** Phase response as a function of B_y oriented along the nanowire axis and microwave frequency f_{exc}. The linear phase ridge of the second harmonic (left) and first harmonic (right) is a hallmark of EDSR.

not be enough for the readout of manipulated states. Optimizing its level is necessary then before doing further advanced manipulations. Fig. 4.6 highlights the effect of the magnetic field $\boldsymbol{B}$ direction on the ICT phase signal while maintaining a constant field module $B = 0.6\,\mathrm{T}$. We adopt a spherical description of the direction of $\boldsymbol{B}$ throughout the polar angle θ_B and the azimuthal φ_B (see top left inset of Fig. 4.6). The interdot signal is found to be heavily impacted by the magnetic field orientation. This suggests an evolution of the g-factors of the QDs as well as the spin-orbit coupling terms depending on θ_B and φ_B [27].

Just as g-factors and state coupling terms are sensitive to $\boldsymbol{B}$ field orientation, the same can be said about the curvature of the state we promote EDSR transitions to. Fig. 4.7 shows the EDSR peak evolution as a function of φ_B while arbitrarily fixing θ_B to 90°. Along this azimuthal trajectory the maximum signal is observed for $\varphi_B = 55°$. Next, we explored the EDSR dependence on the polar angle for $\varphi_B = 55°$. We find that the phase amplitude decreases as we move away from $\theta_B = 90°$. Therefore, in the following experiments of spin manipulation the magnetic field orientation was set to $\varphi_B = 55°$ and $\theta_B = 90°$.

The visibility of the EDSR signal can be yet optimized by a fine tuning of the gate voltages. Fig. 4.8 shows a high-resolution measurement over a narrow region of the stability diagram around the interdot charge transition boundary at $B = 0.52\,\mathrm{T}$ without (top left) and with (top right) continuous resonant microwave tone $f_{exc} = 7.42\,\mathrm{GHz}$. The interdot line has a double peak structure consistently with the data of Figs. 4.2 and 4.4. EDSR appears as a distinct phase signal around $V_{G2} \simeq 363.5\,\mathrm{mV}$ and $V_{G1} \simeq 1039.5\,\mathrm{mV}$, *i.e.* slightly inside the (1,1) charge region, pinpointed by the black arrow as "I/R". Such EDSR feature is extremely localized in the stability diagram reflecting the gate-voltage dependence of the hole g-factor [27].

The bottom part of Fig. 4.8 displays line cuts across the interdot transition line at fixed V_{G1} (along the dashed lines of the figures above) and different microwave excitation conditions. With no microwaves excitation, we observe the double-peak line shape discussed above.

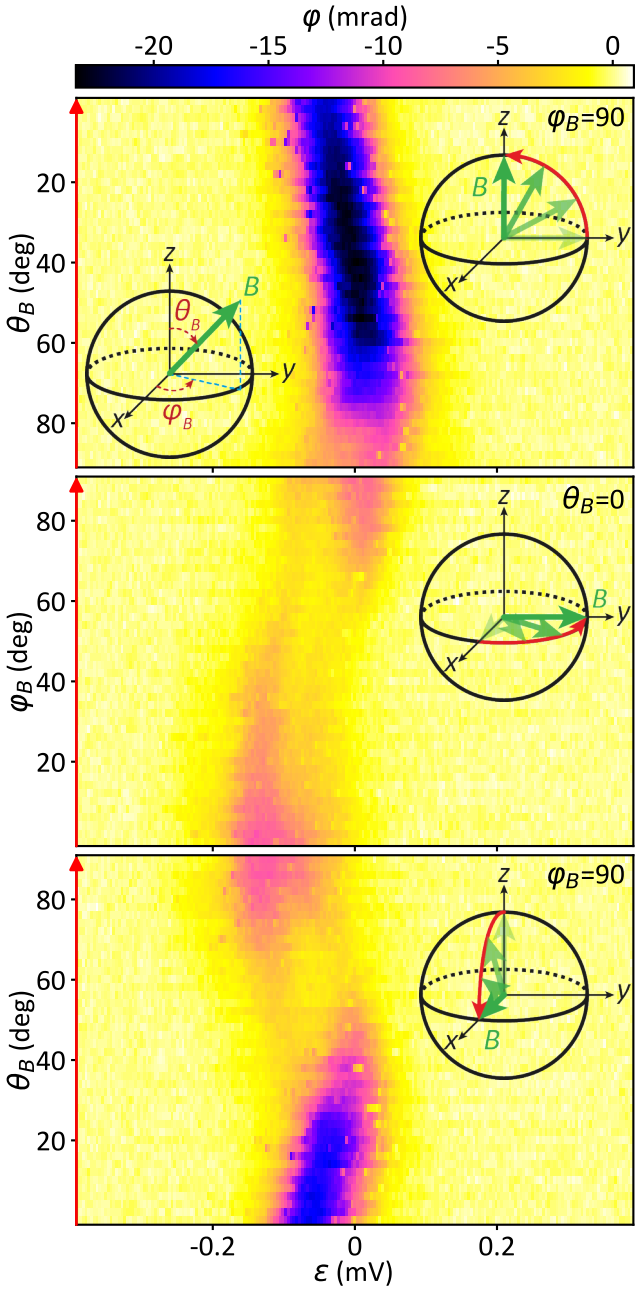

Figure 4.6 – **ICT signal dependence on magnetic field direction.** Phase shift of the reflected signal as a function of the detuning ε and the magnetic field direction. The magnetic field module B is equal to 0.6 T throughout the measurement and the angles θ_B and φ_B are the polar angle and azimuthal angle of its spherical coordinates as illustrated in the top left inset. The top right inset of each graph gives the value of the non-swept magnetic field angle and shows a schematic of the trajectory of $\boldsymbol{B}$ marked by a red arrow that can be found again at the vertical axis of the figure to make the parallel.

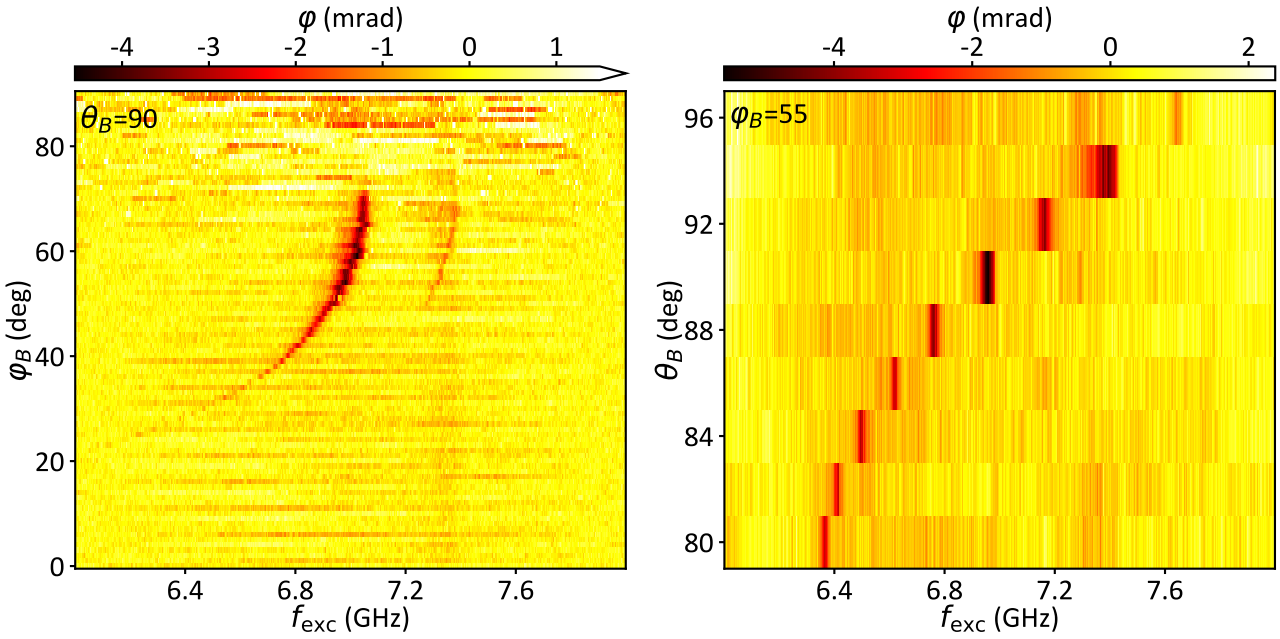

Figure 4.7 – **Magnetic field direction selection.** EDSR peak phase shift as a function of the azimuthal angle φ_B (left) and the polar angle θ_B (right) of the applied magnetic field $\boldsymbol{B}$ with $B = 0.5\,\mathrm{T}$. The highest phase shift is found for $\varphi_B = 55°$ and $\theta_B = 90°$.

With a microwave gate modulation at $f_{\mathrm{exc}} = 7.42\,\mathrm{GHz}$, the spin resonance condition is met at $V_{\mathrm{G2}} \simeq 363.5\,\mathrm{mV}$, which results in a pronounced EDSR peak, the same observed at point "I/R" in the top right panel. The peak vanishes when f_{exc} is detuned by 20 MHz (green trace).

At point "I/R", resonant microwave excitation enables the spectroscopy of the $\mathrm{T}_0(1,1)$ state. In a small detuning window, the populations of $\mathrm{T}_-(1,1)$ and $\mathrm{T}_0(1,1)$ are assumed to be balanced by EDSR (see the energy levels in the inset to the top right panel of Fig. 4.8). This results in a phase signal dramatically enhanced resembling the feature centered at "I/R". A further confirmation that the spin transitions are driven between $\mathrm{T}_-(1,1)$ and $\mathrm{T}_0(1,1)$ is given by the extrapolated intercept at 0 T of the EDSR transition line in Fig. 4.5, found much smaller ($< 100\,\mathrm{MHz}$) than t. In the following, we shall use point "I/R" to perform qubit initialization and readout.

One might expect the detuning position of the EDSR peak to depend on f_{exc}, along with an increase of phase signal approaching $\varepsilon = 0$. However, as observed in other types of Si qubits [122, 130, 91], in the vicinity of $\varepsilon = 0$ decoherence rates increase as well, which limits the detuning window for convenient reflectometry readout. This argument is supported by the data shown in Fig. 4.9.

As pointed out, the microwave-induced population of $\mathrm{T}_0(1,1)$ state is detected in a "shallow" (1,1) charge stability region with a nearly constant dispersion $d|E_{\mathrm{T}_0(1,1)} - E_{\mathrm{T}_-(1,1)}|/d\varepsilon$. In this regime, the qubit is robust with respect to fluctuations in detuning. Close to zero detuning ($363.2 < V_{\mathrm{G2}} < 363.4\,\mathrm{mV}$), the EDSR signal is not resolved, due to the increased noise sensitivity. This makes this bias regime unsuitable for readout.

Now that the optimal conditions are met in order to ensure a good EDSR signal, we could turn to time-domain coherent spin rotations.

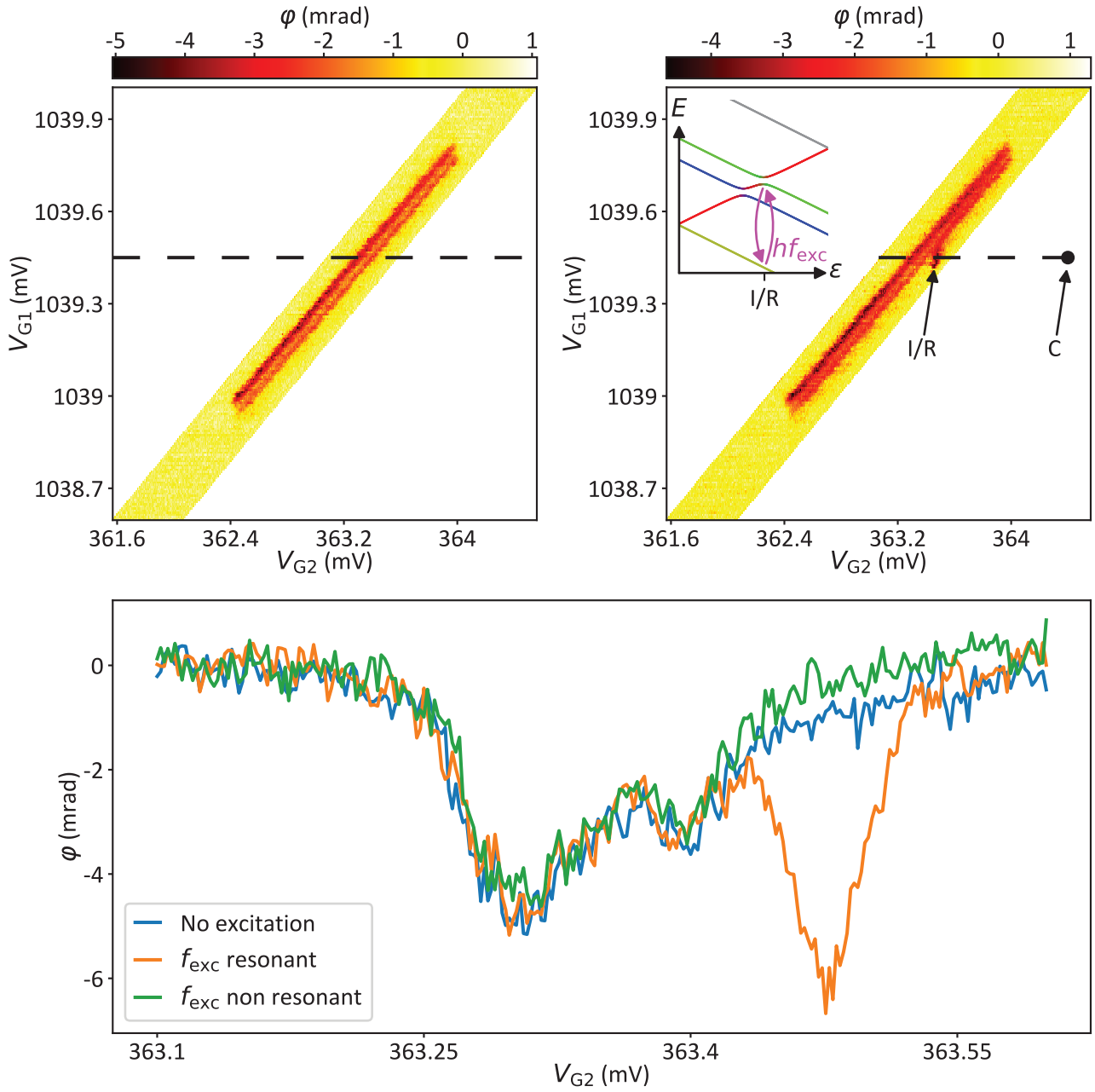

Figure 4.8 – **Manifestations of EDSR in the stability diagram.** Stability diagram at $B = 0.52\,\mathrm{T}$ (orientation $\varphi_B = 55°$ and $\theta_B = 90°$ with no microwave excitation (top left) and with $f_{\mathrm{exc}} = 7.42\,\mathrm{GHz}$ (top left). The change of population induced by EDSR between $\mathrm{T}_-(1,1)$ and $\mathrm{T}_0(1,1)$ (pink arrows in inset) is visible as a localized phase signal at point "I/R". Phase shift cuts are taken along the dashed line (bottom) without microwave irradiation, and with on-resonance and off-resonance excitations at $f_{\mathrm{exc}} = 7.42\,\mathrm{GHz}$ and $7.42\,\mathrm{GHz}$ respectively. When the driving tone is resonant, EDSR-stimulated transitions appear as a pronounced peak.

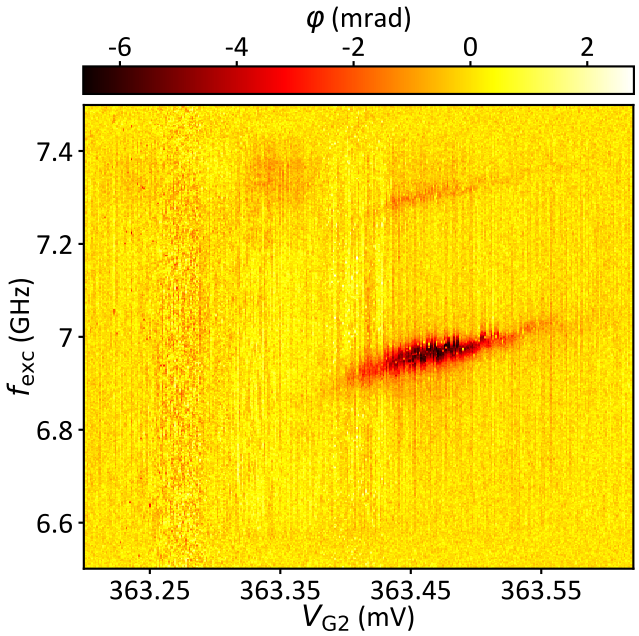

Figure 4.9 – **EDSR peak dependence on gate voltage.** Phase response as a function of the gate 2 voltage and the driving frequency. The map is acquired by sweeping f_{exc} and stepping V_{G2}. At the beginning of each line, the phase of the reflectometry signal is set to 0. The magnetic field $B = 0.5\,\mathrm{T}$ is oriented along $\varphi_B = 55°$ and $\theta_B = 90°$. $\varepsilon = 0$ corresponds to $V_{\mathrm{G2}} \simeq 363.3\,\mathrm{mV}$.

4.5 Single spin manipulation and relaxation time measurement

The device is operated as a spin qubit implementing the protocol outlined in Fig. 4.10. The upper part of the voltage sequence tunes the DQD at the control point "C" ($\simeq 1\,\mathrm{mV}$ deep in the (1,1) region) where holes are strongly localized in either one or the other dot with negligible tunnel coupling. A microwave burst of duration τ_{burst} and frequency f_{exc} drives single spin rotations between $|{\downarrow\downarrow}\rangle$ and $|{\uparrow\downarrow}\rangle$. The system is then brought back to "I/R" in the "shallow" (1,1) regime for a time t_{wait} for readout and initialization. The dispersive readout eventually relies on the spin-resolved phase shift at "I/R", though the reflectometry tone f_{res} is applied during the whole sequence period T_{M} and the reflected signal is streamed constantly to the acquisition module.

We demonstrate coherent single spin control in the chevron plot of Fig. 4.11. The phase signal is collected as a function of microwave burst time τ_{burst} and driving frequency f_{exc}. The spin state is initialized at point "I/R". The phase signal is plotted as a function of τ_{burst} with f_{exc} set at the Larmor frequency f_{Larmor}. The Rabi oscillations shown in the bottom panel have a 10.1 MHz frequency, consistent with previous results [89, 27], and a decaying envelope with a $T_2^{\mathrm{Rabi}} = 0.45 \pm 0.03\,\mu\mathrm{s}$ obtained by fitting the data to:

$$a_0 + a_1 e^{-\frac{\tau_{\mathrm{burst}}}{T_2^{\mathrm{Rabi}}}} \sin(2\pi f_{\mathrm{Rabi}} \tau_{\mathrm{burst}} + a_2), \tag{4.2}$$

where $a_{0,1,2}$ are free fitting parameters.

Fig. 4.11 witnesses the success of using electrical RF signals both for coherent manipulation by EDSR and for qubit-state readout by means of gate reflectometry.

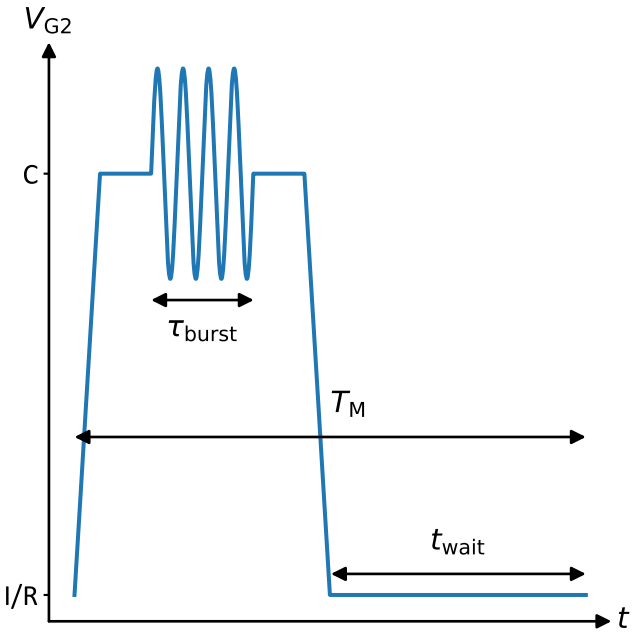

Figure 4.10 – **Qubit manipulation pulse sequence.** The pulse sequence alternating between "deep" $(1,1)$ regime ("C" point in Fig. 4.8) for spin manipulation and "shallow" $(1,1)$ regime ("I/R" point in Fig. 4.8), close to the (0,2) $\leftrightarrow$ (1,1) transition, for the readout and resetting of the spin system. A microwave burst rotates the hole spin for τ_{burst} during the manipulation stage. A waiting time t_{wait} at the "I/R" level ensures the resetting of the spin/charge state. The readout tone is continuously applied throughout the sequence period T_{M}.

We determine the lifetime T_1 of the excited spin state at the readout point "I/R" by sweeping t_{wait} after a π-burst at point "C". The results are shown in Fig. 4.12. The magnetic field direction was set to $\varphi_B = 0°$ and $\theta_B = 60°$ (after a refrigerator incident resulting in the warm-up of the sample, the device was cooled down again and it was found that the EDSR signal was maximized for this magnetic field direction). The phase signal rapidly diminishes with increasing t_{wait} because spin relaxation depopulates the excited spin state in favor of the non-dispersive $\text{T}_-(1,1)$ ground state. The estimated spin lifetime at the readout position is $T_1 = 3.2 \pm 0.3\,\mu\text{s}$. By shifting the position of a 100 ns microwave burst within a 12 µs pulse, no clear decay of the dispersive signal is observed, which suggests a spin lifetime longer than 10 µs at manipulation point.

To extract the spin relaxation time at the readout position "I/R", we use a pulse length of 250 ns and sweep t_{wait}. During the pulse, a microwave burst of 100 ns flips one of the two spins. We normalize the amplitude of the phase shift by a factor $T_{\text{M}}/t_{\text{wait}} = 1 + 250\,\text{ns}/t_{\text{wait}}$ since the signal is acquired during the whole period T_{M}. The readout projects the $|{\uparrow\downarrow}\rangle$ state on the $\{\text{T}_0(1,1), \text{T}_-(1,1)\}$ basis. The time-dependent probability that the spin relaxes in $\text{T}_-(1,1)$ is given by:

$$P(t)_{\text{T}_-(1,1)} = P(t=0)_{\text{T}_0(1,1)} e^{-t/T_1}. \tag{4.3}$$

The time averaged data points in Fig. 4.12 are then fitted to:

$$\varphi = \frac{T_{\text{M}}}{t_{\text{wait}}} \left[a_0 - a_1 \frac{T_1}{T_{\text{M}}} \left(e^{-T_{\text{M}}/T_1} - 1 \right) \right], \tag{4.4}$$

with $T_{\text{M}} = t_{\text{wait}} + 250\,\text{ns}$ and $a_{0,1}$ are fitting parameters.

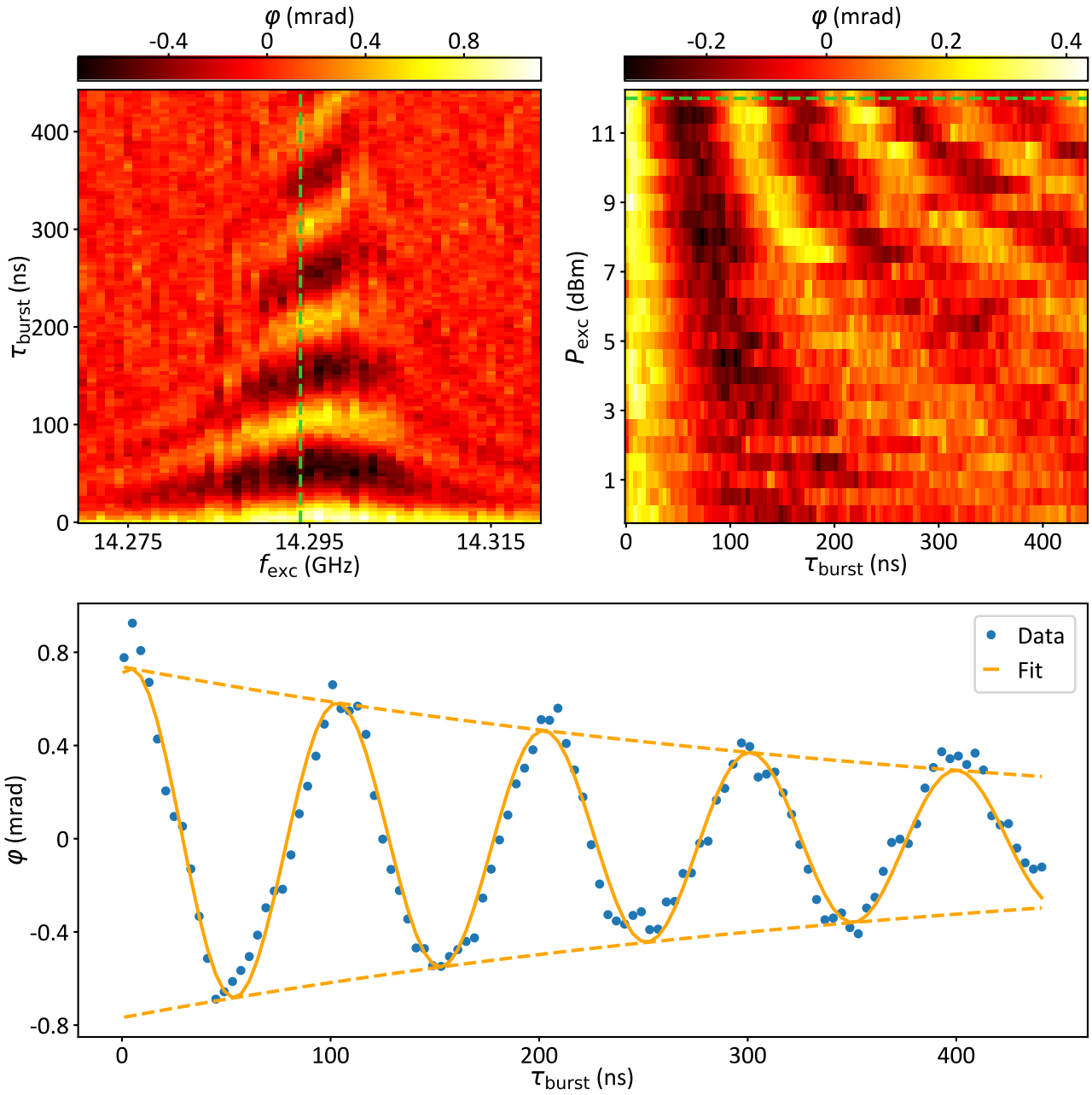

Figure 4.11 – **Chevron pattern and Rabi oscillations.** Dispersive signal $\varphi(f_{\mathrm{exc}}, \tau_{\mathrm{burst}})$ (top left) and $\varphi(\tau_{\mathrm{burst}}, P_{\mathrm{exc}})$ (top right), measured with the detuning pulses of Fig. 4.10 with $t_{\mathrm{wait}} = 1\,\mu\mathrm{s}$. Eight (three) maps have been averaged for the chevron pattern (power dependence) graph. The P_{exc} for the chevron graph is marked by a dashed line on the power dependence graph. A cut long along the dashed line in the top left figure shows Rabi oscillations (bottom panel). A fit of these oscillations yields $f_{\mathrm{Rabi}} = 10.1\,\mathrm{MHz}$ and $T_2^{\mathrm{Rabi}} = 0.45 \pm 0.03\,\mu\mathrm{s}$.

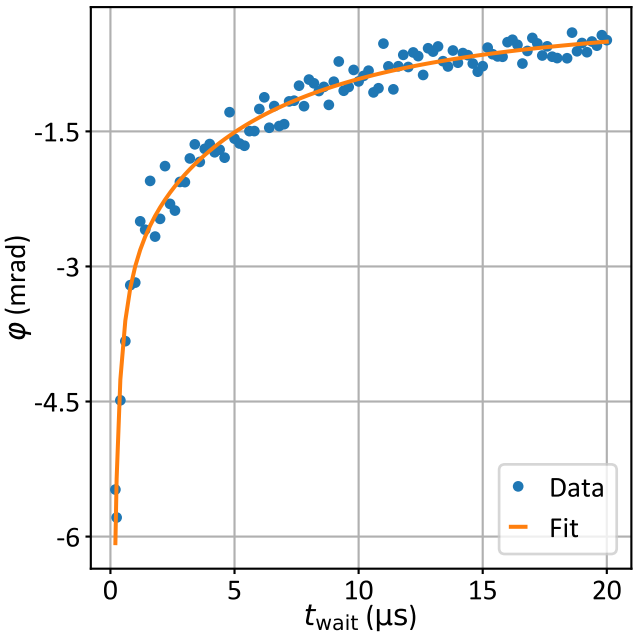

Figure 4.12 – T_1 **measurement.** Phase shift as a function of t_{wait} for a $\simeq 1\,\text{mV}$ pulse on V_{G2}, $\tau_{\text{burst}} = 100\,\text{ns}$ and $f_{\text{exc}} = 12.865\,\text{GHz}$, with $B = 0.62\,\text{T}$ along $\varphi_B = 0°$ and $\theta_B = 60°$. The phase signal approaches 0 when $t_{\text{wait}} \gg T_1$. A simple model yields $T_1 = 3.2 \pm 0.3\,\mu\text{s}$.

The measured T_1 is compatible with the relaxation times obtained for hole singlet-triplet states in acceptor pairs in Si [133] and in Ge/Si nanowire double quantum dots [53]. In both cases T_1 has been measured at the charge degeneracy point with reflectometry setups similar to ours. Nonetheless, charge detector measurements have shown T_1 approaching $100\,\mu\text{s}$ for single hole spins in Ge hut wire quantum dots [144] and $\lesssim 1\,\text{ms}$ for Ge/Si singlet-triplet systems [56]. This suggests that despite the intrinsic spin-orbit coupling single spin lifetimes in the ms range might be achievable in Si too. Strategies to boost T_1 at the readout point may consist of inserting RF isolators between the coupler and the amplifier to reduce the back-action on the qubit and avoiding high-κ dielectric in the gate stack to limit charge noise.

We note that T_1 could depend on the orientation of the magnetic field as well [147]. Future studies on magnetic field anisotropy will clarify whether T_1, along with the effective g-factors (and hence the dispersive shift for readout) and Rabi frequency, can be maximized at once along a specific direction.

Technical improvements intended to enhance the phase sensitivity, like resonators with higher Q-factor and parametric amplification, could push the implemented readout protocol to distinguish spin states with a micro-second integration time, enabling single shot measurement as reported in a recent experiment with a gate-connected superconducting resonant circuit [156]. Lastly, the resonator integration in the back-end of the industrial chip could offer the possibility to engineer the resonant network at a wafer scale, guaranteeing controlled and reproducible qubit-resonator coupling.

The gate-based dispersive sensing demonstrated here does not involve local reservoirs of charges or embedded charge detectors. This meets the requirements of forefront qubit architectures (*e.g.* Ref. [83]), where the spin readout would be performed at will by any gate of the 2D quantum dot array by frequency multiplexing.

Dispersive spin detection by Pauli blockade has a fidelity not constrained by the temperature of the leads. As recently shown [150, 111], isolated DQDs can serve as spin qubits even if placed at environmental temperatures exceeding the spin splitting, like 1 K or more. This should relax many cryogenic constraints and support the co-integration with classical electronics, as foreseen in a scale-up perspective [135].

Takeaway messages:

- The device adopted for this experience is a double-gate, p-type pump device.
- We used gate-coupled RF reflectometry for the dispersive readout of a fully functional spin qubit device.
- The demonstrated qubit readout scheme requires no coupling to a Fermi reservoir, thereby offering a compact and potentially scalable solution.
- We measured Rabi oscillations with a 10.1 MHz frequency and a decaying envelope with a $T_2^{\text{Rabi}} = 0.45\,\mu\text{s}$. We measured also a relaxation time T_1 of 3.2 µs at the readout gate-voltage setting.

Chapter 5

Video Mode

The trouble is, you think you have time.

Buddha

Contents

A two dimensional stability diagram measurement is a very time consuming task an experimenter faces on a daily basis and is considered as a key component in the exploration of the device characteristics. It accounts for a huge amount of measurement time in the first stage of any experiment when it is necessary to find a working point to operate a qubit.

In transport experiments, the time required to explore large stability diagrams of DQD devices can be reduced by applying relatively large source-drain bias voltages. Besides increasing the current level, this turns point or line structures into two-dimensional features that can be captured even with relatively coarse (hence less time-demanding) gate-voltage scans. This cannot be done with gate reflectometry where features remain typically one-dimensional and hence easy to miss. On the other hand, RF gate reflectometry allows for fast measurement while current measurements are intrinsically slow.

We mainly focus in this chapter on optimizing the exploration time of a device by shortening the measurement time of a 2D stability diagram using RF gate reflectometry.

5.1 Understanding basic measurements

In a basic measurement, in order to probe the two dimensional dependence of a measurable parameter λ as a function of two adjustable parameters a and b, one would need to commu-

nicate at least twice for each measurement point on the map. Fig. 5.1 illustrates such a process.

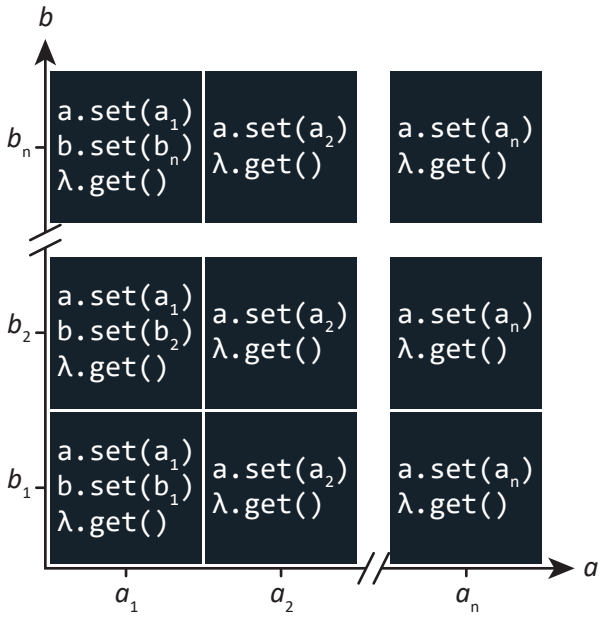

Figure 5.1 – **Illustration of a basic 2D measurement process.** Each square in the map encapsulates the necessary instructions that need to be launched by a controlling unit, and corresponds to a data point (pixel). a_n (b_n) represent the setpoints of parameter a (b).

One could immediately see the flaw in such measurement procedure since each command, to either set or get a parameter, requires a communication time τ_com between the controlling unit and the instrument. In the case of our measurement setup, τ_com differs from an instrument to another but it is in any case no less than 30 ms.

In order to evaluate a minimal measurement time $t_\mathrm{meas}^\mathrm{min}$ for a N by M points map, used as a reference size in this chapter, while omitting any processing time on the controlling unit, we multiply the smallest communication time $\tau_\mathrm{com}^\mathrm{min}$ by the number of operations communicated by the latter unit:

$$t_\mathrm{meas}^\mathrm{min} = N(2M+1)\tau_\mathrm{com}^\mathrm{min}. \tag{5.1}$$

A quick estimation for a 201 by 201 point map, used as a reference size in this chapter, predicts that the measurement will last for at least 40 min if we use 30 ms as a minimal communication time. In real conditions where communication times vary between instruments and depend even on the processor usage of the controlling computer, a similar map takes approximately one hour.

Nevertheless, these measurement times did not present any major drawbacks for the experimenter acquiring a current signal or a conductance through a QPC in the past. This is due to the fact that in these particular dispositions, the exploration of stability diagrams relied on two-dimensional features that did not require a high resolution to be identified by the experienced eye. For example, Fig. 5.2 shows a stability diagram where we could easily see the triangular features associated with interdot tunneling often referred to as bias triangles. Therefore, we could start with a rough quick scan with large spans, and then work our way to the interesting parts of the map by increasing the resolution and lowering the scanned span.

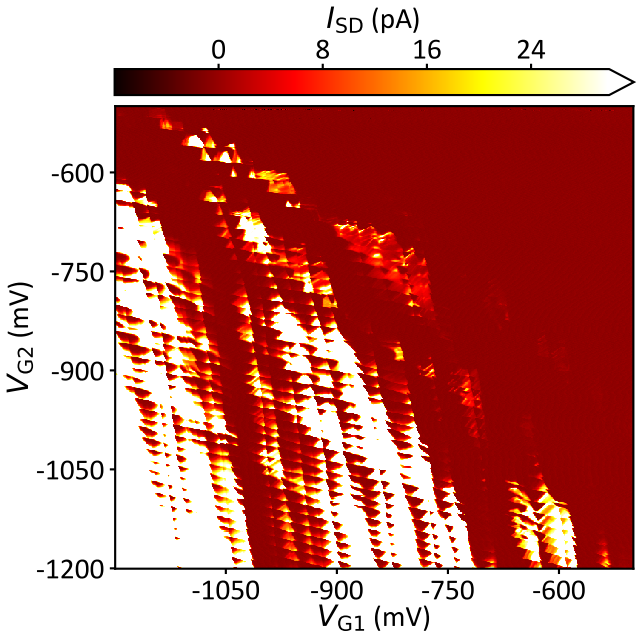

Figure 5.2 – **Example of a stability diagram in current.** Source-drain current as a function of gate voltages V_{G1} and V_{G2}. The applied 10 mV bias results in the opening of bias triangles at the triple points making the search for features easier since the observed objects are two dimensional.

RF gate reflectometry as a readout technique comes with a set of major advantages compared to its transport-based techniques, but also with a major drawback. As explained in Sec. 1.4, the reflectometry features consist of narrow 1D lines (either ICTs or dot-lead transitions). Thus, doing fast scans with a rough precision on both axes is no longer an option since we could totally miss information. An example of a reflectometry measurement is given in Fig. 5.3.

To get an idea on the orders of magnitude needed for a reflectometry based stability diagram, let's consider a 201 point by 201 point map. This map takes 1h15m to be measured using the basic "set voltage, set voltage, get value" sequence. As mentioned before, high resolution is needed for reflectometry, so if we consider a resolution of 50 µV on the gates, our map will be only 10 mV by 10 mV. Thus, to explore a full stability diagram (let's assume 700 mV by 700 mV), it would take nearly a year, and even though there are few tricks to go faster, it remains a very time consuming and unaffordable task.

Considering the reasons listed above, we started developing the so-called video mode (VM) acquisition technique in the interest of reducing the reflectometry measurement times.

5.2 Video Mode implementation

The idea behind this acquisition mode is to get rid of all the communication time with the instruments. In a recent work by the Petta group it was introduced as a real-time tuning tool of the DQD confinement potential [128]. Instead of the basic "set voltage, set voltage, get value" sequence we sweep the gate voltages and acquire continuously the phase between the beginning of the measurement and its end. This is done in our case by applying a saw-tooth pulse to gate 1 and a staircase signal on gate 2. Both signals are commensurate, and each step

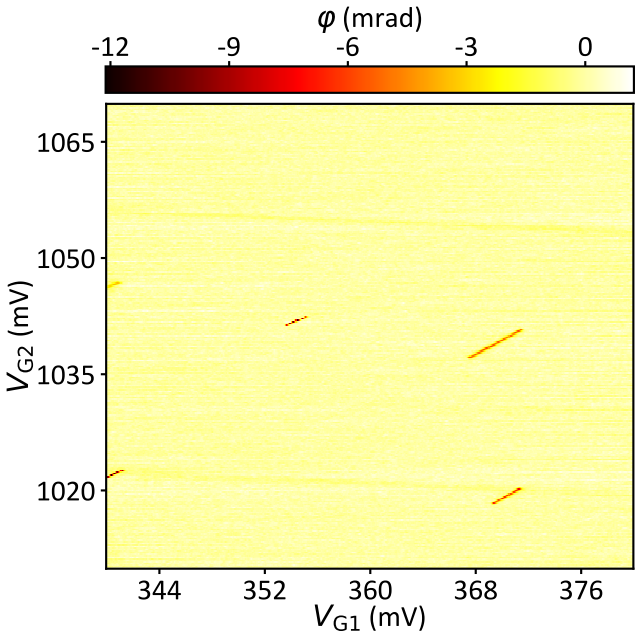

Figure 5.3 – **Example of a gate reflectometry measurement.** Phase response of the resonator as a function of gate voltages V_{G1} and V_{G2}. The visible ICT features are one dimensional lines with sharp signals. A high resolution on at least one of the measurement axes is required in order not to properly detect them.

of V_{G2} corresponds exactly to a V_{G1} sawtooth as illustrated in Fig. 5.4. The generated array of acquired phase values is then transferred as a whole to the python interface.

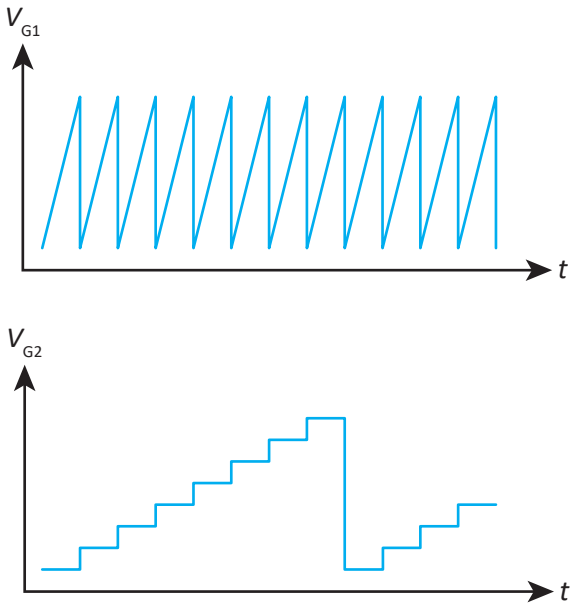

Figure 5.4 – **Pulse sequence used to generate VM maps.** A sawtooth signal is applied to gate 1 while a commensurate stair-shaped signal is applied to gate 2. For each step of V_{G2}, the whole V_{G1} space is swept. In our experiment, the sawtooth signal period is 20 ms

The high sensitivity of the RF gate reflectometry readout makes it possible to rapidly measure charge stability diagrams, but this comes at price: noise. In order to be able to

measure with VM, we need to reduce the demodulator integration time constant τ_c to be at most the sawtooth signal period T_{sawtooth} divided by the number of points N required on gate 1:

$$\tau_c \leq \frac{T_{\text{sawtooth}}}{N}. \tag{5.2}$$

In our case, we set τ_c to be 5 times smaller than the maximal value above which corresponds to the rise time of a second order filter. This results in an integration time of 20 µs and as a consequence in a broad noise distribution. That's why the acquired VM maps need to be averaged in order to reduce noise and pop out the real signals. Fig. 5.5 shows an example of a VM map averaged 10 times.

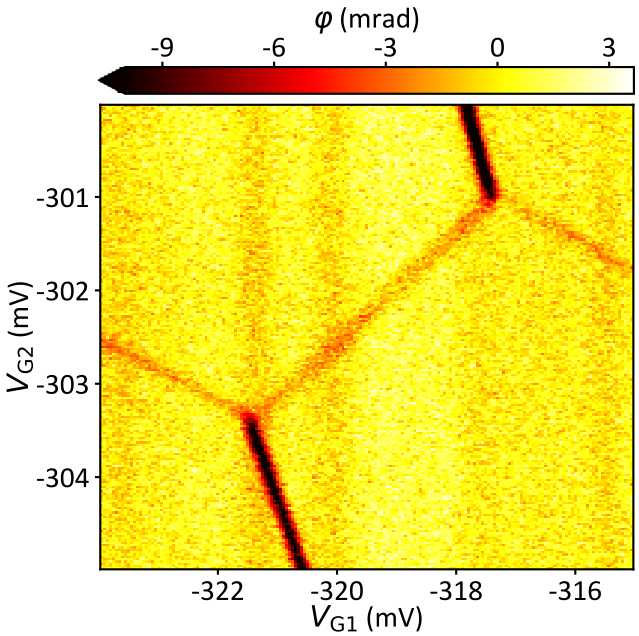

Figure 5.5 – **Example of a reflectometry map generated using VM technique.** Phase response of the resonator as a function of gate voltages V_{G1} and V_{G2} acquired with the VM technique. The measurement shows an ICT and the corresponding dot-lead transitions. This map was averaged 10 times.

By applying this method, the same 201 by 201 point map described above takes only 45 s to be measured with an averaging of 10 maps. This represents a two order of magnitudes gain in acquisition time compared to the basic slow measurement. We note that the noise amplitude is higher in a VM measurement since the time constant used to filter the noise is set to a small value allowing the fast gate sweeping, but nevertheless, the features standout if the map is averaged enough.

Even though the technique described above allowed for fast stability measurements on a window of 10 mV by 10 mV, exploring the full stability diagram using this new meshing still requires a full week of measurements. And it's also quite a heavy task to go through each of the measured maps and searching for the desired interdot features: it requires still a considerable amount of human time. That's why I have further optimized this technique as described in the next section.

5.3 Coarse Video Mode

In order to further reduce the time for the exploration of a stability diagram, we came up with an even faster measurement technique, baptised coarse video mode (CVM). Instead of doing fine scans on both gates, we just maintain a high precision on gate 1 and we step gate 2 coarsely. This way, the maps generated are 201 point by 21 point with a resolution of 50 µV on gate 1 and 500 µV on gate 2. The scanned window remains therefore the same 10 mV by 10 mV. It is worth mentioning that the 500 µV step is not arbitrarily chosen: it represents a resolution yielding at least 2 points for the smallest of ICT features.

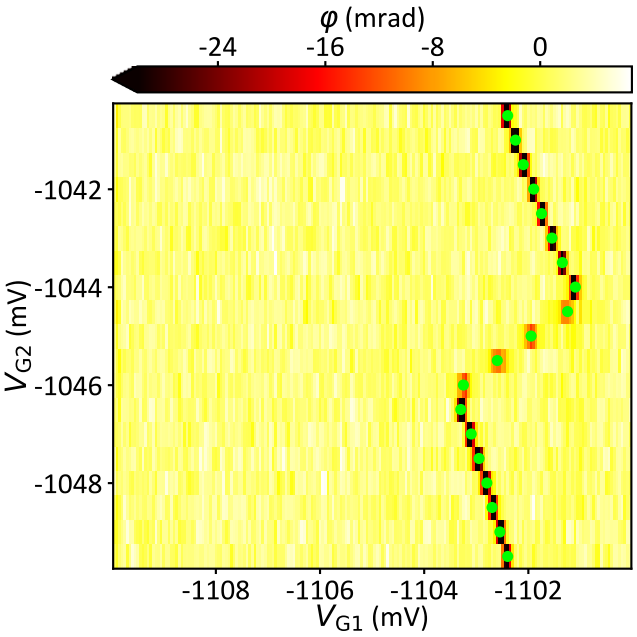

Figure 5.6 – **A CVM map example.** Phase response of the resonator as a function of gate voltages V_{G1} and V_{G2} acquired with the VM technique. The precision on gate 2 is 0.5 mV (coarse) and 50 µV on gate 1 (fine). A peak detection algorithm runs through each line of the map allowing the extraction of all dips marked by green points on the graph. All detected points exhibit signals higher than a certain threshold which is set to 7 mrad in our experience.

Furthermore, we use a peak detection algorithm on each line of a CVM map to extract the signal dips that are greater than a certain threshold in amplitude. We store for each detected dip the coordinates in the (V_{G1}, V_{G2}) plane as well as its height and its FWHM. This allows us afterwards to reconstruct the full stability diagram just by scattering the detected dips instead of concatenating all the smaller scans, the latter option being really heavy on the processing unit and requiring a lot of random access memory (RAM). Fig. 5.6 gives an example of a CVM measurement where the detected peak positions are marked by green dots. This map took only 5 s to be measured, which represents an order of magnitude gain in measurement time as compared to VM and a total of three orders of magnitudes gain as compared to a basic measurement.

As explained, instead of going through each of the measured maps, one could simply scatter all the detected peaks on a plot to get the full stability diagram as shown in Fig. 5.7. This full stability diagram was measured in only 20 hours and it contains all of the relevant information in a stability diagram (except signals below the detection threshold which we consider not interesting anyway).

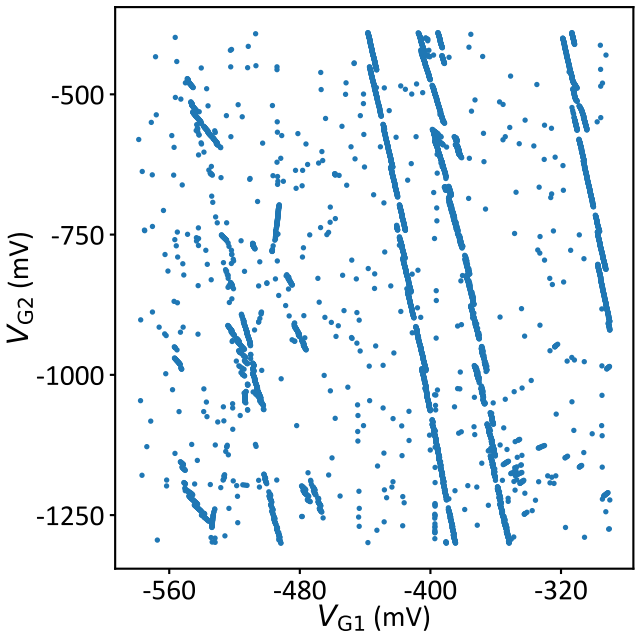

Figure 5.7 – **A full stability diagram obtained by scattering all the detected peaks measured by CVM technique.** Detected dips positions as a function of gate voltages V_{G1} and V_{G2} . The full map is divided into small 10 mV by 10 mV units in which we detect all the dips using the CVM technique.

Even though we were able to reconstruct the full stability diagram in way less time, the obtained result still suffers from noise. A post processing stage is therefore required and will be presented in the next section.

5.4 Post processing and interdot detection

We rely in the post processing stage on the density-based spatial clustering of applications with noise (DBSCAN) algorithm to get rid of all the outlier detected dips that represent noise. Given a maximal distance between the points, based on our knowledge of scan parameters, this unsupervised machine learning algorithm labels all the singular points. This filtering process is shown in Fig. 5.8.

At the same time, the DBSCAN algorithm classifies groups of nearby points. It identifies core samples of high density and extends clusters from them. This allows us to separate the detected dips into groups of continuous features. Fig. 5.9 makes a side by side comparison between a filtered stability map and its corresponding clustered version.

After having a list of clustered points, we apply a linear regression on each group and we look for regressions with positive slopes (only ICTs have positive slopes) and with a good correlation coefficient (aligned points). This allows the identification of simple ICTs with no detectable dot-lead transitions highlighted by red rectangles in Fig. 5.10. The scattered points were plotted using their detected dip height for the color.

Although this ICT detection technique isn't optimal and cannot be applied to Fig. 5.5, it gives us a head start to be able to automate some routine measurement, *e.g.* magnetospectroscopy, on the detected ones. One could also browse the full stability diagram in its final

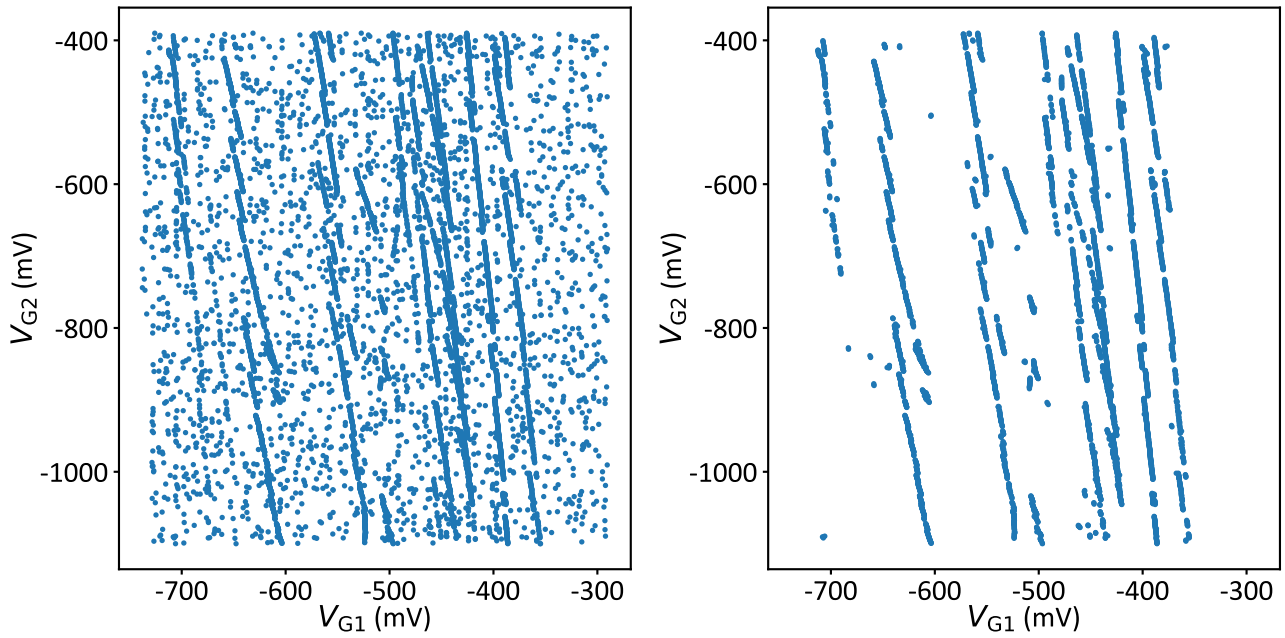

Figure 5.8 – **Filtering detected dips.** Side by side comparison of a raw stability diagram achieved by CVM technique (on the left) and the corresponding filtered version (on the right) using DBSCAN clustering algorithm to detect outlier points emanating from noise and false peak detection. A maximal distance between neighbouring points needs to be provided to the algorithm.

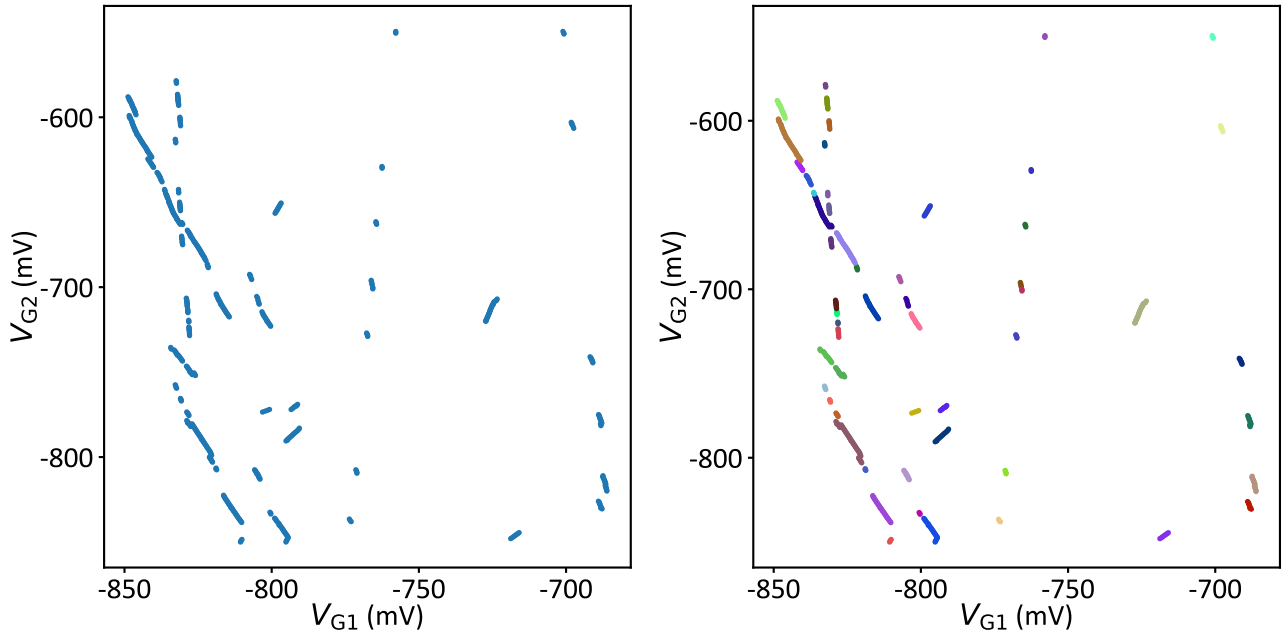

Figure 5.9 – **Clustering detected dips.** Filtered stability diagram (on the left) and the corresponding clustered version (on the right) using DBSCAN clustering algorithm. Each cluster of points is colored distinctively. A maximal distance between neighbouring points needs to be provided to the algorithm.

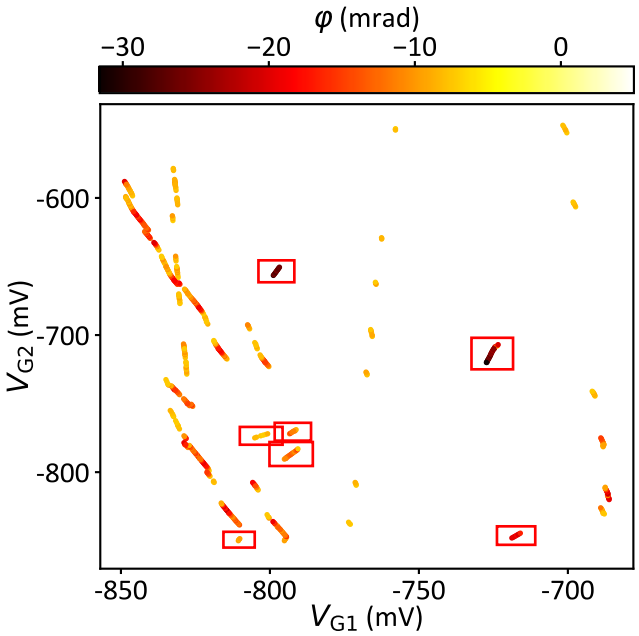

Figure 5.10 – **A full stability diagram after post processing and interdot detection.** Detected dips using CVM technique after being filtered. A clustering process coupled with a simple linear regression detection algorithm allows the discovery of potential ICTs highlighted with red boxes. Each point on the map is plotted with the corresponding detected height.

state as presented in Fig. 5.10 and look for the remaining required features.

Takeaway messages:

- Basic measurements require a lot of time and are nor suited for stability diagram exploration when the searched features are not 2D.
- The VM technique allows for a fast exploration of small windows of a stability diagram. It is well suited when requiring to zoom on particular region of a bigger map and allow a two order of magnitude gain in acquisition time.
- The CVM technique is a derivative of the VM technique where we reduce the precision on one axis and detect the signal dips. It allows a lossless reconstruction of a full big stability diagram by just scattering the detected dips.
- Post processing the results of the CVM technique with the DBSCAN algorithm allows noise filtering and clustering of the features. Coupled with a simple regression algorithm, it allows us to automatically find simple ICTs.

Chapter 6

Dispersively probed microwave spectroscopy of a silicon hole double quantum dot

> Physics does not endeavour to explain nature. In fact, the great success of physics is due to a restriction of its objectives: it only endeavours to explain the regularities in the behavior of objects.
>
> Eugene Paul WIGNER

Contents

Owing to ever increasing gate fidelities and to a potential transferability to industrial CMOS technology, silicon spin qubits have become a compelling option in the strive for quantum computation. In a scalable architecture, each spin qubit will have to be finely tuned and its operating conditions accurately determined. In this prospect, spectroscopic tools compatible with a scalable device layout are of

primary importance.

Despite all the advantages of gate-based dispersive readout, it also has its limitations. One of the main drawbacks is the limited information about the fundamental energy spectrum of each qubit gate-based dispersive readout is able to provide compared to commonly used charge sensing. This includes trivial quantities such as gate lever arms and charge tunnel couplings in general but also quantum dot level spacings and in particular for spin-orbit qubits the g-factor and spin-orbit interaction strength. However, dispersive readout coupled with microwave spectroscopy has been proven to be a powerful tool to access some of these information, among them lever arm [108] and charge tunnel coupling [110, 108].

Here we report on a two-tone spectroscopy technique providing access to the spin-dependent energy-level spectrum of a hole DQD defined in a split-gate silicon device. A first GHz-frequency tone drives electric-dipole spin resonance enabled by the valence-band spin-orbit coupling. A second lower-frequency tone ($\approx 500\,\mathrm{MHz}$) allows for dispersive readout via RF-gate reflectometry. We compare the measured dispersive response to the linear response calculated in an extended Jaynes-Cummings model and we obtain characteristic parameters such as g-factors and tunnel/spin-orbit couplings for both even and odd occupation allowing for the reconstruction of the entire energy spectrum of the DQD necessary for qubit control and readout.

6.1 Methods

The experiment in this chapter is carried out on devices 2 and 3 described in Sec. 2.3. The face-to-face geometry of these devices allows the accumulation of holes DQD in parallel (with source and drain) by applying negative DC voltages V_{G1} and V_{G2} on the gates when the device is operated in a dilution refrigerator at the base temperature $T_{\mathrm{base}} \approx 20\,\mathrm{mK}$. The two dots are formed at the corners of the channel overlapped by the gates [142]. Gate 2 is connected to a broadband high frequency coaxial line that allows to drive spin resonances. Gate 1 is connected to a surface mount inductor, which forms with its parasitic capacitance and device impedance an LC resonator with a resonance frequency $f_{\mathrm{res}} = \omega_{\mathrm{res}}/(2\pi) = 497\,\mathrm{MHz}$ on device 2 (ICT 1 and ICT 2) and $f_{\mathrm{res}} = 560\,\mathrm{MHz}$ on device 3 (ICT 3). The RF power P_{res} applied to the resonator is constant throughout all the spectroscopy measurements and is set to a value low enough to avoid any signal broadening. We estimate $P_{\mathrm{res}} \approx -110\,\mathrm{dBm}$. The full measurement circuit is reported in Sec. 3.1.

The hole DQD acts as a variable load for the LC resonator and the resonance frequency undergoes a dispersive shift depending on the DQD state (see Sec. 1.4). This can be readily understood if one considers a (M+1,N) $\leftrightarrow$ (M,N+1) ICT with M (N) the charge number in the left (right) dot. The two-state Hamiltonian of this system writes $\mathcal{H}_{\mathrm{DQD}} = -\varepsilon\,\sigma_z/2 - \Delta\,\sigma_{\mathrm{x}}/2$, where the Pauli matrices act in the space of the charge configuration. σ_{x} describes the tunneling between the dots that opens a gap Δ in the energy spectrum. The difference in energy of the two states reads $E = \sqrt{\varepsilon^2 + \Delta^2}$ and is a function of the detuning ε. In the adiabatic limit, when the resonator angular frequency $\omega_{\mathrm{res}} \ll E/\hbar$, the interaction between a charge qubit and a resonator has often been treated semi-classically with the introduction of quantum capacitances [32, 127, 93]. However, when the frequency of the readout oscillator is comparable to the characteristic frequency of the measured system ($\omega_{\mathrm{res}} \simeq E/\hbar$), a quantum mechanical treatment of the interaction with an extended Jaynes-Cummings Hamiltonian is convenient in order to take into account the finite frequency of the readout apparatus.

Recently, it was shown that for a charge qubit, such a model captures the interaction also in the adiabatic limit [107]. Here, we therefore model all the interactions within the framework of the Jaynes-Cummings Hamiltonian. This quantum approach provides complementary physical insights and proves useful in describing more complex situations. In particular, we extend the Jaynes-Cummings model to the driven case (with microwaves at frequency f_{exc}), where we also capture dispersive shifts due to resonantly driven transitions between states in the DQD (a complete discussion of the underlying theory can be found in Appendix B).

The coupling between the DQD and the read-out resonator, described by the Hamiltonian $\mathcal{H}_{\mathrm{r}} = \hbar\omega_{\mathrm{res}}\left(a^{\dagger}a + 1/2\right)$, is expressed in the basis of the charge configurations as $\mathcal{H}_{\mathrm{int}} = \hbar g_{\mathrm{c}}\sigma_z\left(a + a^{\dagger}\right)$, with a the annihilation operator of the oscillator, $g_{\mathrm{c}} = (\alpha_1 - \alpha_2)eV_{\mathrm{rms}}/(2\hbar)$ the coupling strength between the charge and the microwave photons, $V_{\mathrm{rms}} = \sqrt{\hbar\omega_{\mathrm{res}}/(2C_{\mathrm{r}})}$ the zero-point voltage fluctuation of the LC oscillator, and C_{r} is the capacitance of the LC circuit (which includes the geometric capacitance of the DQD). The coupling between gate 1 and the DQD charge leads to a phase shift between the incoming and the reflected microwaves. In the linear regime discussed in Appendix B, the phase shift can be expressed as

$$\delta\phi = \frac{4Q_{\mathrm{loaded}}\mathrm{Re}\chi(\omega_{\mathrm{res}})}{\omega_{\mathrm{res}}}, \tag{6.1}$$

where $\chi(\omega_{\mathrm{res}})$ is the charge response function whose real part represents the linear shift in the resonant angular frequency of the LC circuit and Q_{loaded} is the resonator loaded Q-factor. For a pair of states near charge degeneracy with the readout oscillator in the adiabatic limit, the response function is real and equals

$$\chi = -\frac{2\hbar g_{\mathrm{c}}^2\Delta^2}{\left(\varepsilon^2 + \Delta^2\right)^{3/2}};\ k_{\mathrm{B}}T,\ \hbar\omega_{\mathrm{res}},\ \hbar\Gamma_2 \ll \Delta, \tag{6.2}$$

where k_{B} is the Boltzmann constant, T is the equilibrium temperature of the DQD environment and Γ_2 is the decoherence rate of the DQD charge. Eq. (6.2) is equivalent to the standard oscillator shift $\delta\omega_{\mathrm{res}} = -C_{\mathrm{Q}}\omega_{\mathrm{res}}/(2C_{\mathrm{r}})$, with C_{Q} the quantum capacitance of the DQD [110, 23, 93].

6.2 Stability diagrams and magnetospectroscopy

When measuring the phase response of the resonator at its resonance frequency while sweeping the gate voltages V_{G1} and V_{G2}, we obtain the charge stability diagram of the DQD system. Diagonal features with positive slope in this diagram mark ICTs. This work is focused on three interdot transitions ICT 1 and ICT 2 on device 1 and ICT 3 on device 2, all chosen to have an estimated hole number below 20 in each dot. Figs. 6.1 to 6.3 show the stability diagrams around ICT 1, ICT 2 and ICT 3 respectively. Using the model introduced above and fitting the phase response as a function of detuning at each ICT we find a charge-photon coupling $g_{\mathrm{c}}/(2\pi) \simeq 35\,\mathrm{MHz}$ for all three interdot transitions (see Sec. 6.4.3).

Any given ICT is characterized by either an even or an odd parity of the total occupation number in the DQD. Without knowing this number, different parities can still be discriminated through the magnetic field evolution (magnetospectroscopy) of the corresponding ICT phase response [25, 123, 131].

For holes in silicon, the presence of spin-orbit interaction is changing the magnetic field dependence of the ICT as spin-flip tunneling is allowed and couples different spin states. However,

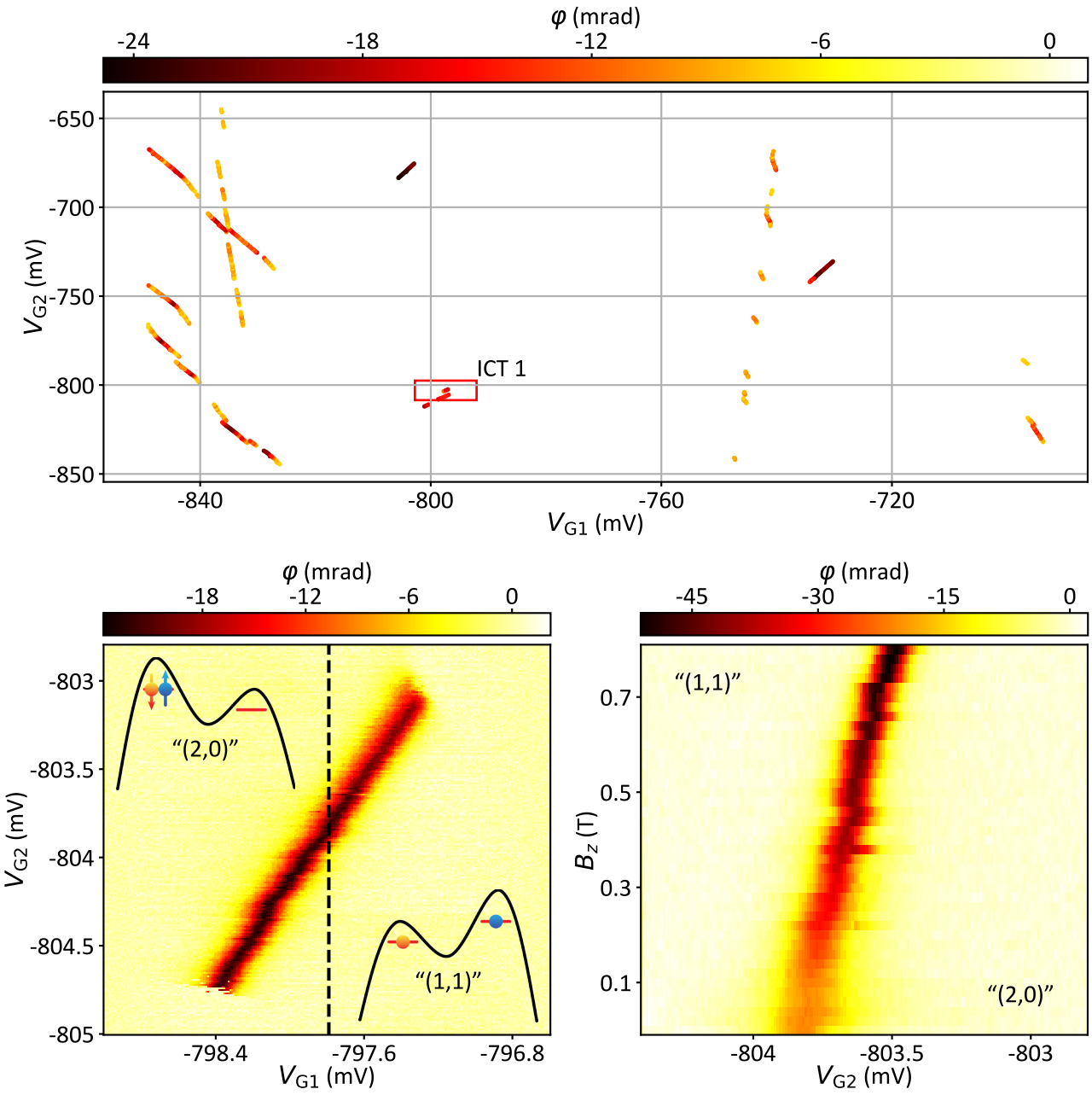

Figure 6.1 – **Interdot 1 stability diagram and magnetospectroscopy. (Top panel)** Phase response of the LC resonator as a function of V_{G1} and V_{G2} around ICT 1 highlighted with a red rectangle. The map was acquired using the VM technique. Each scattered point represents a detected peak in the scan. **(Bottom left panel)** Phase response of the LC resonator as a function of V_{G1} and V_{G2} showing a zoom on ICT 1 of even parity. The insets show the equivalent one- and two-electron charge configurations just above and below ICT 1. The first (second) number represents the equivalent hole occupation in the dot under gate 1 (gate 2). **(Bottom right panel)** Phase response as a function of V_{G2} and B_z at fixed V_{G1} (see dashed line in bottom left figure) revealing the ground-state evolution in magnetic field.

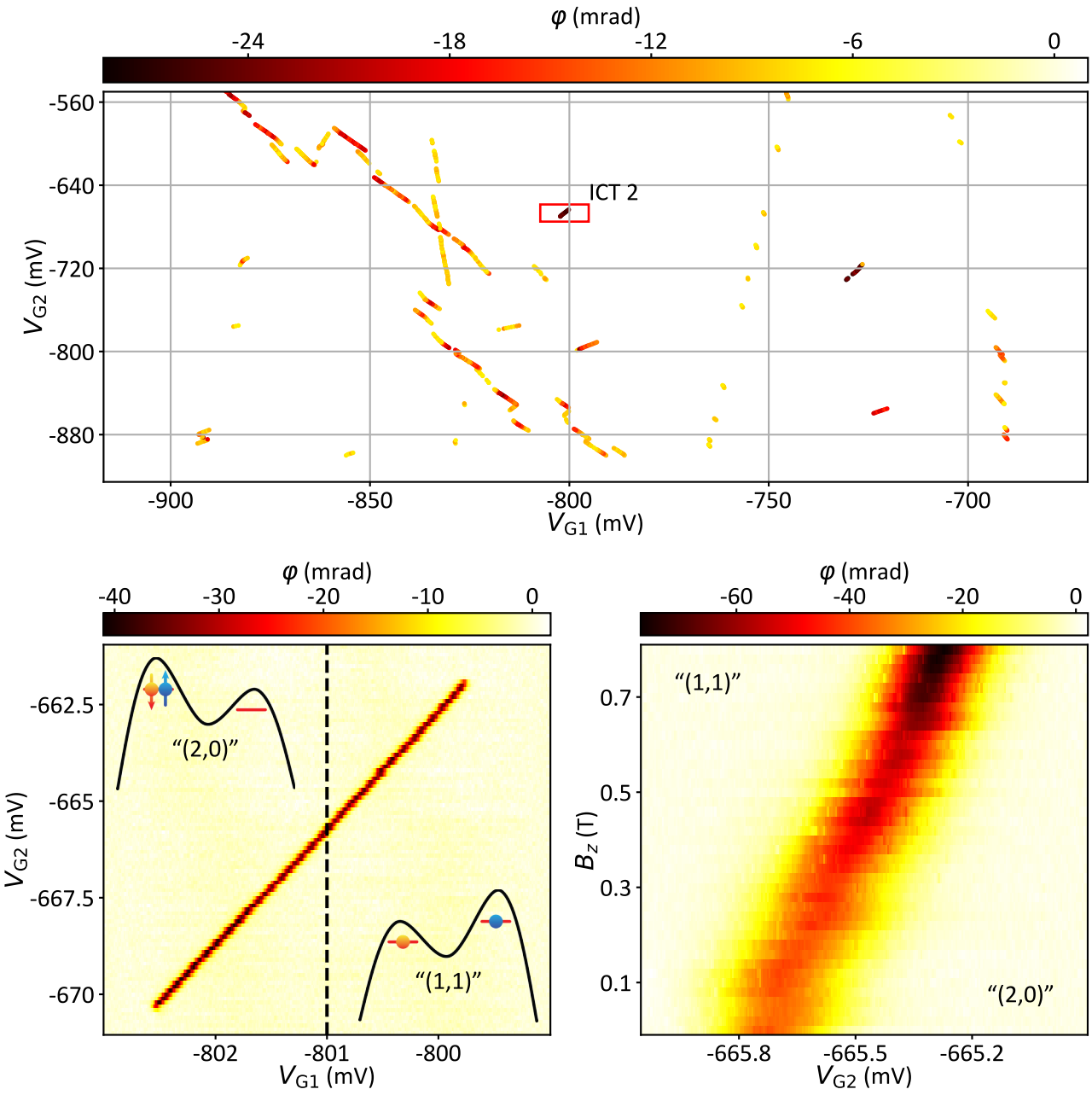

Figure 6.2 – **Interdot 2 stability diagram and magnetospectroscopy (Top panel)** Phase response of the LC resonator as a function of V_{G1} and V_{G2} around ICT 2 highlighted with a red rectangle. The map was acquired using the VM technique. Each scattered point represents a detected peak in the scan. **(Bottom left panel)** Phase response of the LC resonator as a function of V_{G1} and V_{G2} showing a zoom on ICT 2 of even parity. The insets show the equivalent one- and two-electron charge configurations just above and below ICT 2. The first (second) number represents the equivalent hole occupation in the dot under gate 1 (gate 2). **(Bottom right panel)** Phase response as a function of V_{G2} and B_z at fixed V_{G1} (see dashed line in bottom left figure) revealing the ground-state evolution in magnetic field.

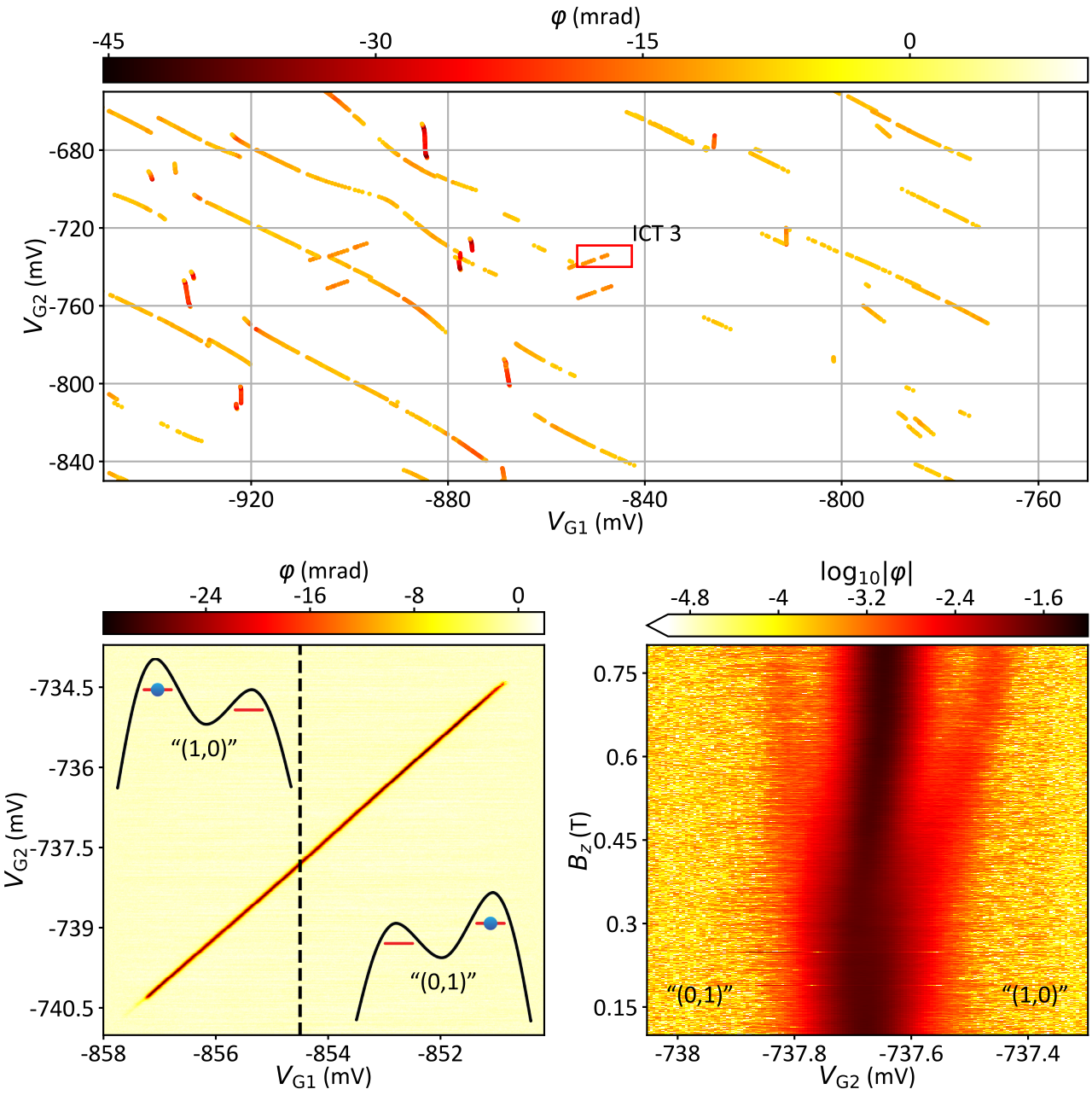

Figure 6.3 – **Interdot 3 stability diagram and magnetospectroscopy (Top panel)** Phase response of the LC resonator as a function of V_{G1} and V_{G2} around ICT 3 highlighted with a red rectangle. The map was acquired using the VM technique. Each scattered point represents a detected peak in the scan. **(Bottom left panel)** Phase response of the LC resonator as a function of V_{G1} and V_{G2} showing a zoom on ICT 3 of odd parity. The insets show the equivalent one- and two-electron charge configurations just above and below ICT 3. The first (second) number represents the equivalent hole occupation in the dot under gate 1 (gate 2). **(Bottom right panel)** Phase response as a function of V_{G2} and B_z at fixed V_{G1} (see dashed line in bottom left figure) revealing the ground-state evolution in magnetic field.

we show in the next paragraph that it is still possible to infer the interdot charge parity from the dispersive response in magnetic field. The phase response of the LC resonator is measured as a function of V_{G2} and magnetic field, keeping V_{G1} constant. Measurements are shown in the bottom right panels of Figs. 6.1 to 6.3.

In the even case, Figs. 6.1 and 6.2, the dip in phase at zero detuning and zero magnetic field arising from the avoided crossing of the S(1,1) $\leftrightarrow$ S(2,0) remains unchanged as long as the Zeeman energy of the polarized triplet state $E_Z < \Delta$. Once E_Z becomes larger than Δ, the state $|\downarrow\downarrow\rangle$ becomes the ground state in the (1,1) configuration and a new avoided-crossing mediated by spin-orbit interaction between $|\downarrow\downarrow\rangle$ and S(2,0) emerges, which we characterize by an energy gap Δ_{SO}, see Fig. 6.7 for an energy diagram at finite magnetic field. With increasing magnetic field, this avoided crossing moves towards higher detuning, which explains why the dips in phase in Figs. 6.1 and 6.2 move towards larger V_{G2} as the magnetic field is increased. Moreover, the increase in phase shift is due to $\Delta_{SO} < \Delta$, which gives rise to a higher dispersive shift χ at higher field following Eq. (6.2). We would like to stress out that the situation described here is different from a previously reported situation in Chap. 4 of a hole DQD in silicon [26]. There, the negligible Δ_{SO} paired with a Δ comparable to temperature, led to the thermal population of higher laying states, which themselves led to a dispersive shift of the resonator.

In the odd case, see Fig. 6.3, the central dip in phase does not vary much with increasing magnetic field indicating that the nature of the ground state is unchanged. However Fig. 6.3 shows two additional phase signals appearing on either side of the central phase dip. These originate from higher-lying avoided crossings in the DQD level spectrum that lead to nonzero electric susceptibility, see Fig. 6.8 for an energy diagram at finite magnetic field. Their origin is the spin-orbit mediated coupling of states with opposite spins in the two dots. With increasing magnetic field, these dips in phase move away from the central feature and fade out. The dispersion is again linked to a change in E_Z, whereas the reduced phase signal is explained by a lower occupation probability of the excited state by thermal activation. The slight dispersion of the central dip arises from a difference in the Landé g-factors of the two QDs. The dispersive detection of higher-lying avoided crossings due to spin-orbit interaction is similar to the recently reported observation of valley splittings in cavity-coupled electron quantum dots in silicon [92].

6.3 Spectroscopy measurements

Having established the parity of each ICT, we proceed to microwave spectroscopy to explore the full DQD level spectrum as a function of magnetic field, B_z, along the z-axis, *i.e.* perpendicular to the substrate. Both even and odd charge configurations have two anti-crossing states, with single and doublet spin character, respectively.

The even configurations are characterized by the additional presence of spin-triplet states, which can be neglected at zero magnetic field because of their negligible dispersive shift. As a result, in both even and odd cases, a single charge tunnels between the two QDs giving rise to a nonzero electric susceptibility at the ICT, see Eq. (6.2). We can extend this model to capture microwave photon induced tunnel events by adding a fast electrical drive $A_{exc}\cos(\omega_{exc}t)/2$ to gate 2. The Hamiltonian describing the full system includes now also $\mathcal{H}_{exc} = A_{exc}\cos(\omega_{exc}t)\,\sigma_z/2$, where A_{exc} is the amplitude of the fast drive signal. By solving the

complete Hamiltonian $\mathcal{H} = \mathcal{H}_{\mathrm{DQD}} + \mathcal{H}_{\mathrm{exc}} + \mathcal{H}_{\mathrm{r}} + \mathcal{H}_{\mathrm{int}}$, we find a linear response function:

$$\chi(\omega_{\mathrm{res}}) = -\left[-\frac{2\hbar g_c^2 \Delta^2}{E^3}\frac{\delta\omega}{\omega_{\mathrm{R}}} + \left(g_c \frac{\varepsilon}{E}\frac{\omega_{\mathrm{R0}}}{\omega_{\mathrm{R}}}\right)^2 \frac{1}{\omega_{\mathrm{R}} - \omega_{\mathrm{res}} - i\tilde{\Gamma}_2}\right] D, \tag{6.3}$$

where $\delta\omega = \omega_{\mathrm{exc}} - E/\hbar$ is the detuning of the drive frequency ω_d from the DQD transition energy E, $\omega_{\mathrm{R}} = \sqrt{\delta\omega^2 + \omega_{\mathrm{R0}}^2}$ is the Rabi frequency due to the resonant drive with $\omega_{\mathrm{R0}} = A_{\mathrm{exc}}\Delta/(2\hbar E)$, $\tilde{\Gamma}_2$ is the decoherence rate of the driven system and D is the difference of the occupation probability of the ground and excited state in the dressed basis. The first term is the adiabatic response already described in Eq. (6.2), whereas the second term includes now the dispersive shift due to resonantly driven charge transitions in the DQD. Let us note that in Eq. (6.3) we have only retained the rotating wave approximation (RWA) contribution of the resonant term which is relevant to our regime of operations and accounts for the damping of the signal when increasing dot detuning. The region of accuracy of the RWA is quite extended, over a dot detuning range at least the gap Δ, and matches the important region of the resonant signal. In other conditions where $\omega_r \ll \omega_R$ the non-RWA contribution may also be included straightforwardly. A detailed derivation of Eq. (6.3) is given in Appendix B.

6.3.1 Excitation power calibration

When applying a constant room temperature microwave power through the spectroscopy line, the corresponding spectroscopy maps clearly indicate that the delivered power at the device level varies with f_{exc}. In order to ensure a constant power seen by the sample, we search, for each applied frequency, the spectroscopy power P_{limit} that will decrease the interdot signal by 5 %. But doing so, P_{limit} values would be affected by the physics of the DQD. Therefore, we perform this calibration procedure on different ICTs and then average all the curves to minimize the individual physics related contributions of each interdot.

Fig. 6.4 presents an average of four calibration curves measured on four different ICTs. In the case of ICT 1 (Sec. 6.3.3), the power of the microwave signal at frequency f_{exc} is held constant at room temperature, while in the case of ICT 2 (6.3.2) and ICT 3 (Sec. 6.3.4), the power is adapted at each frequency in order to ensure that the power delivered to the sample is quasi-constant. In doing so, frequency dependent attenuation as well as standing wave interferences leading to large power variations are mostly corrected for.

6.3.2 Spectroscopy at zero magnetic field

Fig. 6.5 shows the phase response of the even-parity ICT 2 as a function of V_{G2} and $f_{\mathrm{exc}} = \omega_{\mathrm{exc}}/(2\pi)$ for fixed V_{G1}. Qualitatively similar results can be found for odd parity cases, such as ICT 3 (not shown). To analyze the data in the top panels of Fig. 6.5 we refer to the corresponding energy diagram at zero magnetic field, shown in the bottom plot of Fig. 6.5. Resonant microwave induced transitions are highlighted by double arrows at positive and negative detuning.

The vertical ridge at $V_{\mathrm{G2}} \simeq -669.1\,\mathrm{mV}$ corresponds to the dispersive shift arising from the charge qubit associated to the S(1,1) $\leftrightarrow$ S(2,0) anticrossing as described by the first term in

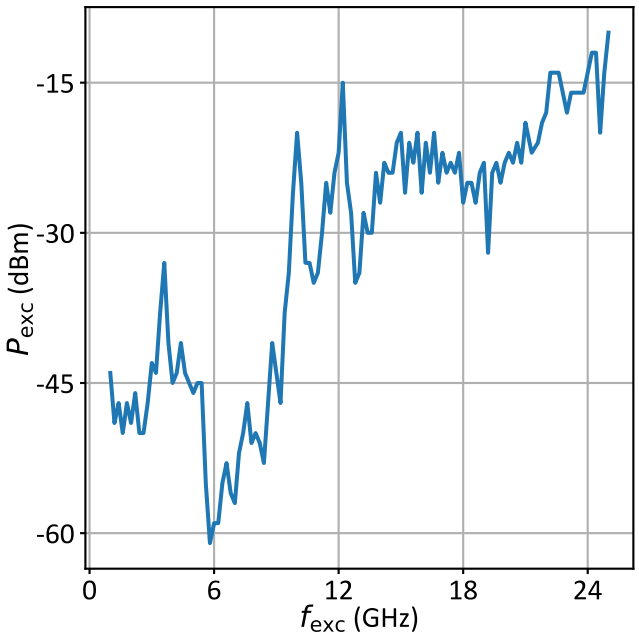

Figure 6.4 – **Excitation power calibration.** Room temperature microwave source power P_{exc} as a function of excitation frequency f_{exc} such as the delivered power at the sample level is quasi-constant.

Eq. (6.3). The phase dip along this line vanishes when the microwave excitation energy matches the energy gap Δ due to tunnel coupling, *i.e.* when $\delta\omega \to 0$ [110, 108, 131]. From this we find $\Delta/h = 5.72 \pm 0.04\,\text{GHz}$ (see Sec. 6.4.1 for the detailed extraction).

Two side branches can be seen in the the same figure. They consist of dip-peak features due to microwave-assisted excitation away from the charge degeneracy point at $\epsilon = 0$. They occur when the microwave tone is in resonance with the charge qubit energy E, once again when $\delta\omega \to 0$, and they are accounted for by the second term in Eq. (6.3).

At large detuning ($\varepsilon \gg \Delta$), the side branch turn into straight lines whose slope can be used to extract the lever-arm parameter $\alpha_2 = 0.160 \pm 0.001$ relating detuning energy to gate 2 voltage, see Sec. 6.4.2. From the slope of the ICT 2 line in the bottom left panel of Fig. 6.2, we can further infer the lever-arm parameter for gate 1, $\alpha_1 = 0.50 \pm 0.02$.

The data in Fig. 6.5 shows a clear asymmetry between the two branches, with the branch at positive detuning being more pronounced. This asymmetry may be ascribed to the presence of the triplet states, which affects the population of the anti-crossing singlet states. At negative detuning, the S(1,1) ground state is partially depopulated due the thermal population of the closely lying triplet excited states. This should lead to fainter side branch since the triplets do not contribute any measurable dispersive phase shift and cannot be photon-excited to the S(2,0) state due to time-reversal symmetry at zero magnetic field.

Using the model introduced above, we can qualitatively reproduce the experimental results, as shown in the top right part of Fig. 6.5, where the transition energy, E, is highlighted by a white dashed line. The exact shape of the dip-/peak phase branches that emerge when the charge qubit is driven resonantly at non-zero detuning is a sensitive function of dephasing and relaxation whose complete modelling goes beyond the scope of this work.

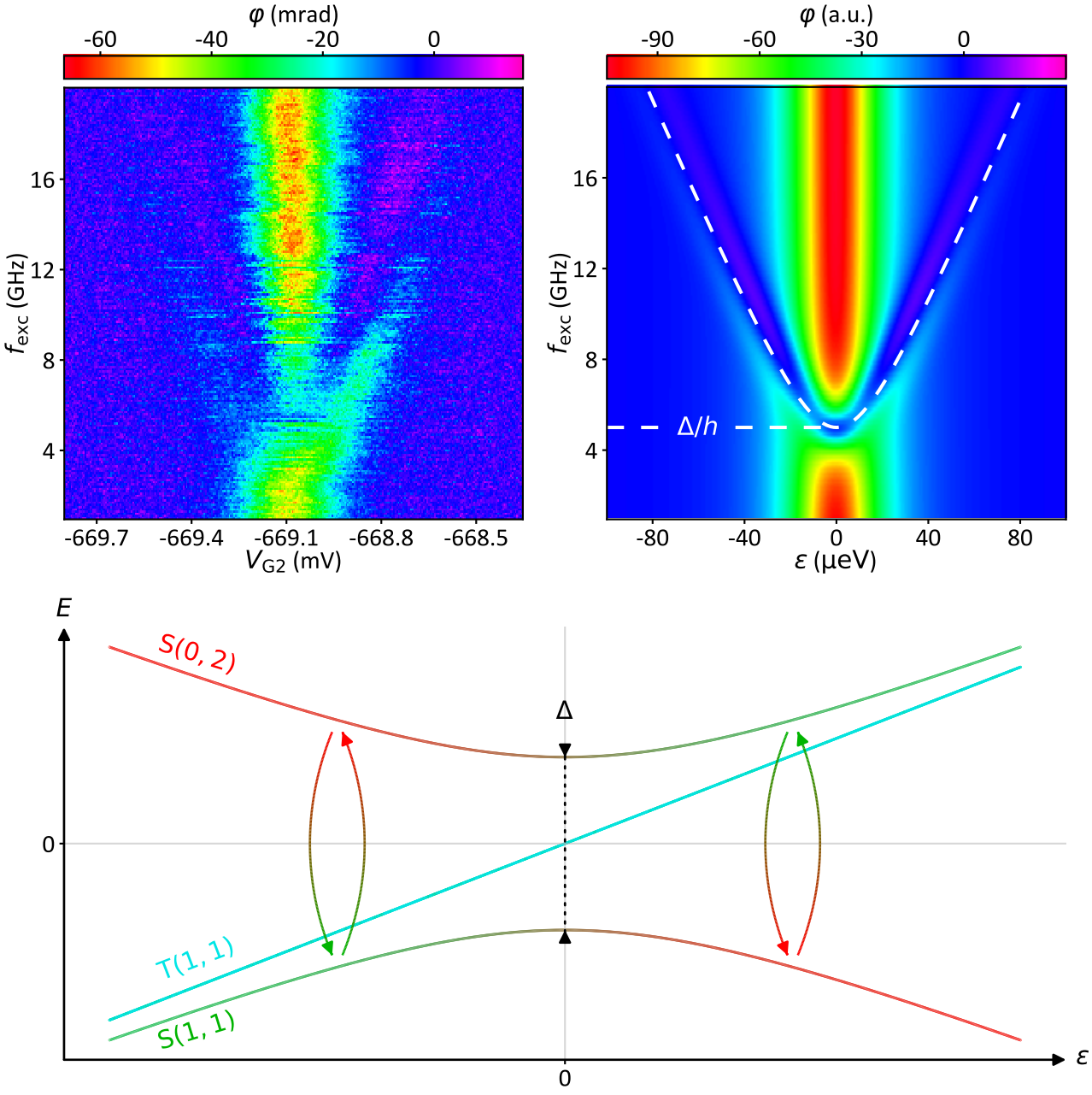

Figure 6.5 – **Photon assisted spectroscopy at zero magnetic field. (Top left panel)** Phase response of the resonator as a function of V_{G2} and microwave frequency f_{exc} at zero magnetic field. The output power of the microwave generator is adjusted for each f_{exc} in order to deliver a constant power at the device level. We estimate the power at the device level to be around $-70\,\mathrm{dBm}$. In addition to the central interdot transition signal vanishing at $5.72 \pm 0.04\,\mathrm{GHz}$, two side branches mark photon-assisted charge transitions between the quantum dots. **(Top right panel)** Theoretical simulation of the driven DQD phase response. The central dip at $\varepsilon = 0$ vanishes when the excitation energy matches Δ. **(Bottom panel)** Energy diagram of a DQD near the "(1,1)" $\leftrightarrow$ "(2,0)" transition at zero magnetic field. The double arrows mark the processes giving rise to the branches observed in top figures.

When the system is strongly driven , multi-photon processes can occur ($nhf_{\mathrm{exc}} = E$, where n is an integer). Fig. 6.6 shows the phase response at large microwave power. In addition to the dispersive shift of the driven charge qubit originating from a one photon process, new branches appear at half and one-third the frequencies of the original branches demonstrating two- and three-photon processes, respectively. The theoretical description of the multi-photon case can be found in Appendix B.

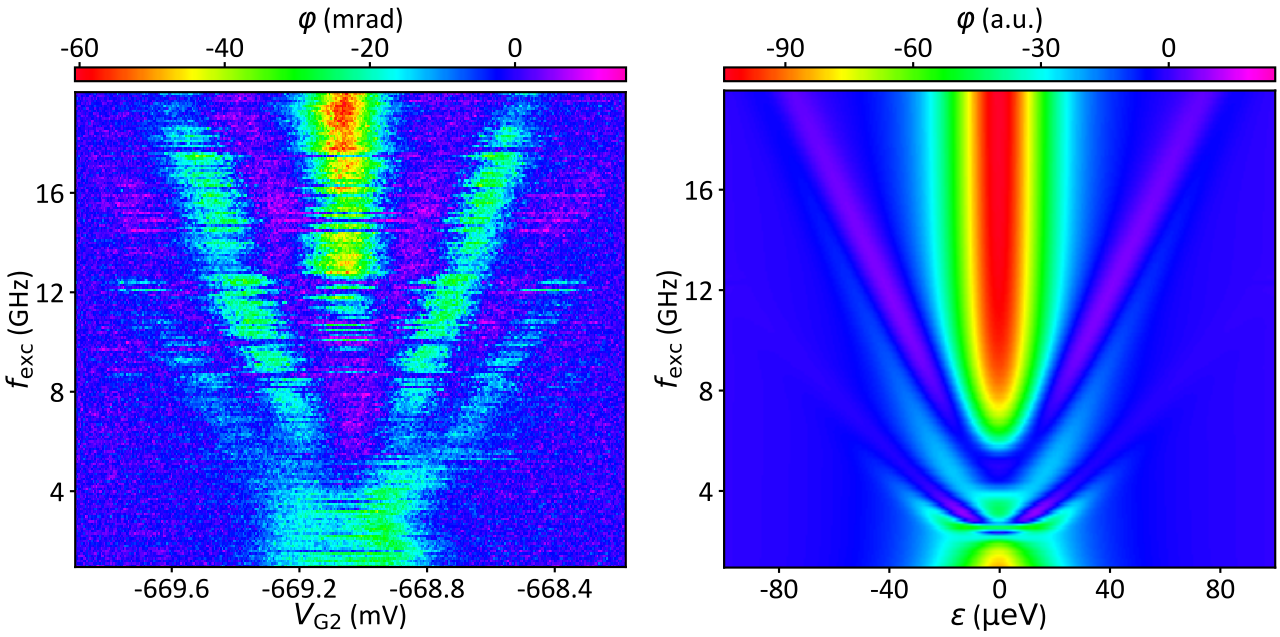

Figure 6.6 – **Multi-photon processes at zero magnetic field.** Phase response of the resonator as a function of V_{G2} and microwave frequency f_{exc} at zero magnetic field at a high driving power P_{exc} giving rise for multi-photon processes. The delivered microwave power is increased by 10 dBm compared to Fig. 6.5. Additional side branches appear at one half and one third of the side-branch frequency in Fig. 6.5 indicating two-photon and three-photon process, respectively.

To sum up, microwave spectroscopy at zero magnetic field is a powerful tool to extract the interdot charge tunnel coupling as well as the lever-arm parameters for both gates allowing the reconstruction of the DQD spectrum at zero magnetic field.

6.3.3 Spectroscopy of a double quantum dot with an even charge configuration at finite magnetic field

We now proceed with microwave spectroscopy at finite magnetic field to explore the spin-split energy levels and the spin-orbit coupling in the DQDs. First, we present results for ICT 1. At an external magnetic field $B_z = 600\,\mathrm{mT}$, the triplet states split leading to a DQD energy spectrum as illustrated in the bottom of Fig. 6.7, where the $|\downarrow\downarrow\rangle$ is the ground state at $\varepsilon = 0$. Due to a difference in g-factors between the two quantum dots, the $\mathrm{T}_0(1,1)$ state mixes with the singlet S(2,0) state around $\varepsilon = 0$ and a new basis for the (1,1) states consisting of four non-degenerate states $|\downarrow\downarrow\rangle$, $|\uparrow\downarrow\rangle$, $|\downarrow\uparrow\rangle$ and $|\uparrow\uparrow\rangle$ needs to be adopted. At positive detuning, $|\downarrow\downarrow\rangle$ and S(2,0) couple due to the intrinsic spin-orbit coupling in the valence band of silicon. At finite magnetic field, This gives rise to an avoided crossing Δ_{SO} with characteristic energy Δ_{SO}

at a magnetic-field-dependent detuning $\varepsilon = \varepsilon_{SO}$.

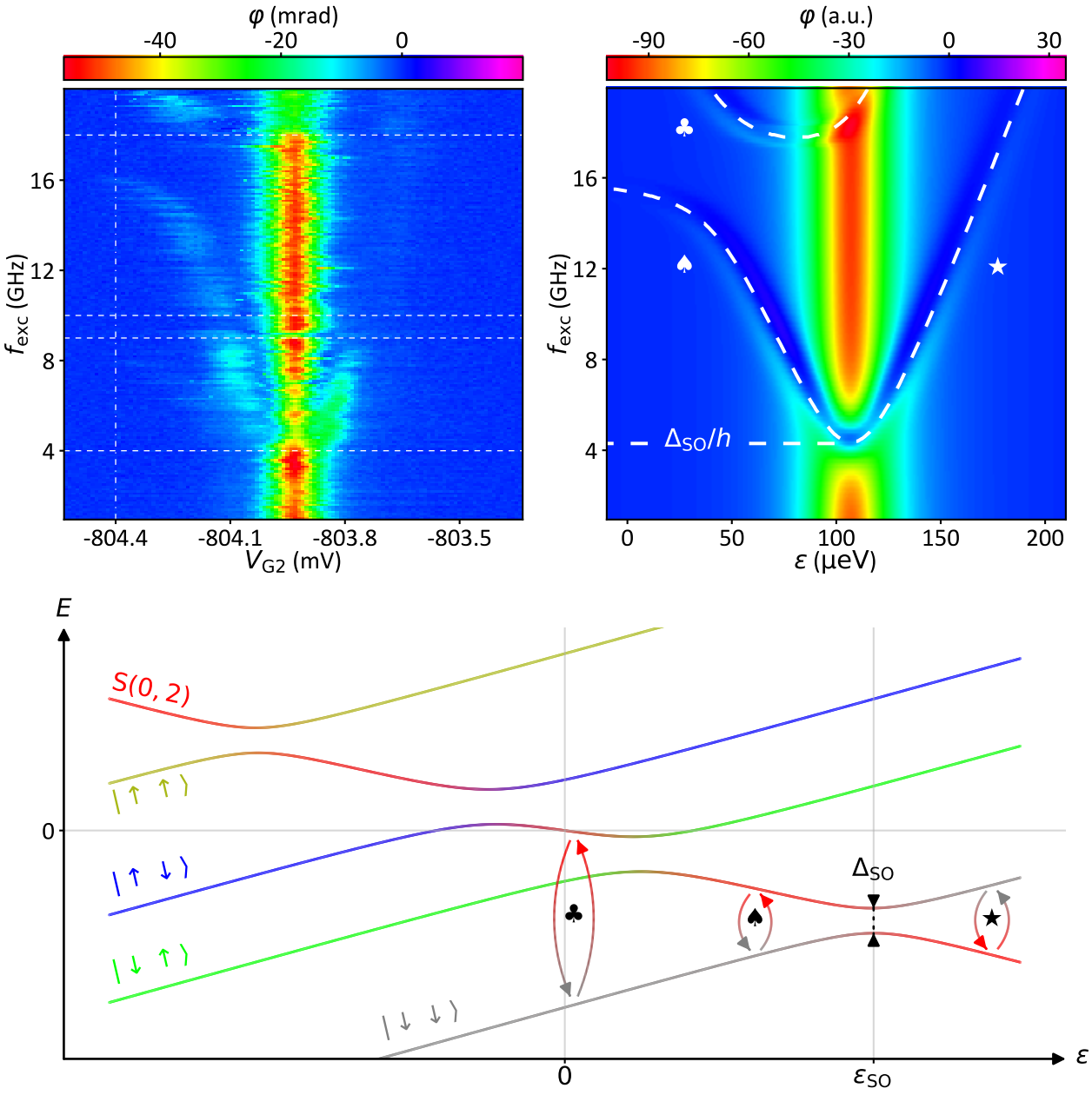

Figure 6.7 – **Photon assisted spectroscopy at finite magnetic field for an even-parity ICT. (Top left panel)** Phase response of the LC resonator around the spin-orbit anticrossing of $|\downarrow\downarrow\rangle$ with S(2,0) as a function of V_{G2} and f_{exc} at $B_z = 600\,\mathrm{mT}$. The dashed horizontal lines delimit regions in which the spectroscopy tone power is held constant at room temperature. The dash-dotted vertical line marks the position of the ICT at zero magnetic field, corresponding to $\varepsilon = 0$. The strong vertical structure is associated with the spin-orbit anticrossing at $\varepsilon = \varepsilon_{SO}$. It vanishes at $f_{exc} = \Delta_{SO}/h = 4.6 \pm 0.1\,\mathrm{GHz}$. The three side branches around the central signal correspond to photon induced charge transitions between the quantum dots, as indicated in the bottom figure. **(Top right panel)** Corresponding simulated phase response of the driven DQD. **(Bottom panel)** Energy diagram of the DQD around a "(1,1)" ↔ "(2,0)" transition at finite magnetic field and with $g_1 \neq g_2$. The photon-induced charge transitions responsible for the side branches in top figures are indicated by arrows and corresponding symbols.

Around ε_{SO}, the hole DQD could be operated as a "spin-flip" charge qubit. In the top left

panel of Fig. 6.7, we show a two-tone spectroscopy around $\varepsilon = \varepsilon_{SO}$. The dispersive interaction of the qubit with the resonator gives rise to the vertical dip structure at $V_{G2} \simeq -803.9\,\text{mV}$. As for the case of a spin-less charge qubit (Fig. 6.5), we observe a local suppression of this dip structure from which we extract a spin-orbit-mediated avoided crossing $\Delta_{SO}/h = 4.6 \pm 0.1\,\text{GHz}$ (see Sec. 6.4.1).

Away from ε_{SO}, the dispersive shift due to the driven "spin-flip" charge qubit arises when the microwave photon energy matches the energy splitting between S(2,0) and $|\downarrow\downarrow\rangle$. Close to $V_{G2} = -804.2\,\text{mV}$, *i.e.* close to zero detuning, the left branch bends towards a horizontal asymptote around 16.1 GHz. This arises from the hybridization of the exited state S(2,0) with the $|\downarrow\uparrow\rangle$ state, as shown in Fig. 6.7. In this regime, the "spin-flip" charge qubit evolves to a single-dot "spin-orbit" qubit for which the electric dipole is largely reduced and cannot be sensed by the LC resonator. From the frequency of the horizontal asymptote we extract the g-factor of the second dot, $g_2 = 1.92 \pm 0.02$. At $V_{G2} = -804.2\,\text{mV}$ and for frequencies close to 20 GHz an additional phase signal is visible in Fig. 6.7. This signal can be associated to the transition between $|\downarrow\downarrow\rangle$ and the hybridized S(2,0) and $|\uparrow\downarrow\rangle$ states. In principle, this branch could allow for the extraction of the g-factor of the first dot. However, due the upper limit of 20 GHz in our microwave generator, we were not able to fully capture this feature and we only infer $g_1 > 2.38$.

Similarly to the zero magnetic field case, the dispersive shift of the resonator can be modeled by also taking into account the spin degree of freedom as well as the spin orbit interaction. Apart from spin-flip tunnel events, the physics remains the same. We again find a qualitative agreement with the measurements, see top right part in Fig. 6.7. The white dashed lines highlight the transition energies as indicated with different arrows in the energy diagram of Fig. 6.7. We again note that the exact shape of the side wings depend on the details of the decoherence of the driven system and therefore exact modeling goes beyond the scope of this work.

6.3.4 Spectroscopy of a double quantum dot with an odd charge configuration at finite magnetic field

We now present in Fig. 6.8 microwave spectroscopy measurements for ICT 3, the odd-parity ICT. At finite magnetic field the basis states $|\text{L}\rangle$ and $|\text{R}\rangle$ of an odd parity ICT are spin split into $|\text{L}\downarrow\rangle$, $|\text{L}\uparrow\rangle$, $|\text{R}\downarrow\rangle$ and $|\text{R}\uparrow\rangle$, resulting in the energy diagram of the bottom plot in Fig. 6.8. Around zero detuning, pure charge tunnel coupling gives rise to avoided crossings between states with the same spin, *i.e.* between $|\text{L}\downarrow\rangle$ and $|\text{R}\downarrow\rangle$ and between $|\text{L}\uparrow\rangle$ and $|\text{R}\uparrow\rangle$. The strong central feature in top panel of Fig. 6.8 is due to the dispersive shift associated with the lowest energy one, involving spin-down states.

Similar to the even-parity case, two side branches arise when hf_{exc} matches the energy difference between ground and excited states, corresponding to transitions from $|\text{L}\downarrow\rangle$ to $|\text{R}\downarrow\rangle$ and vice-versa. They exhibit clear avoided crossings around 12 GHz. The one on the left (right) is due to a spin-orbit-mediated tunnel coupling between $|\text{L}\uparrow\rangle$ and $|\text{R}\downarrow\rangle$ ($|\text{L}\downarrow\rangle$ and $|\text{R}\uparrow\rangle$). As for the previous cases, we model the dispersive shift of the resonator. We again find a qualitative agreement with the measurements, see top right part in Fig. 6.8. We would like to point out that the observed branches, highlighted by white dashed lines, are in fact due to two-photon excitations. As a consequence, transition frequencies in Fig. 6.8 are a factor of two smaller than the actual transition energies. From the amplitude of the measured avoided crossings we find a spin-orbit gap $\Delta_{SO}/h = 2.4\,\text{GHz}$. In addition, the side branch on the left (right) approaches

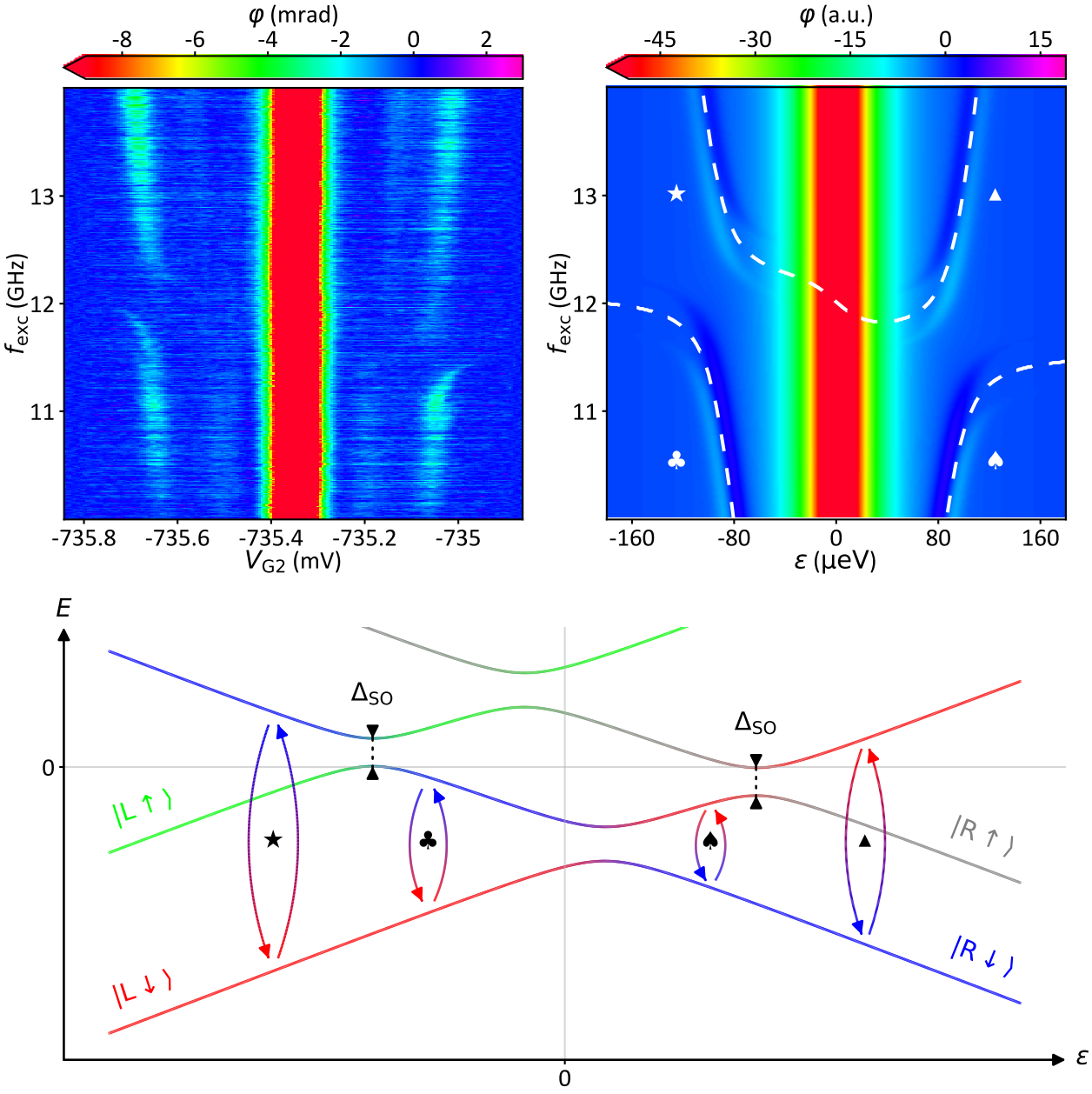

Figure 6.8 – **Photon assisted spectroscopy at finite magnetic field for an odd-parity ICT. (Top left panel)** Phase response of the LC resonator around zero detuning as a function of V_{G2} and f_{exc} at $B_z = 1.3\,\mathrm{T}$. The dispersive response due to the charge qubit is visible as the vertical feature at $V_{G2} \approx -737.35\,\mathrm{mV}$. At resonance, $2hf_{exc} = \Omega$, the resonator undergoes as well a phase shift. Around 12 GHz spin-orbit anticrossings between states with opposite spin localized in different dots are detectable in the driven response. **(Top right panel)** Corresponding simulated phase response of the one hole driven DQD. **(Bottom panel)** Energy diagram of a single hole in a DQD ("(0,1)" ↔ "(1,0)" transition) at finite magnetic field with $g_1 \simeq g_2$. At zero detuning, the down spin states of the left and right dot undergo an anticrossing due to tunneling t. A small anticrossing due to the spin-orbit interaction appears between the down spin states of one dot and the up spin states of the other dot. Microwave induced transitions that give rise to the two branches are highlighted with arrows and corresponding symbols.

asymptotically a constant frequency set by the Zeeman energy in the left (right) quantum dot. This allows us to determine the two g-factors of the DQD, which happen to be differ slightly from each other, *i.e.* $g_{\mathrm{L}} = 1.27$ and $g_{\mathrm{R}} = 1.33$.

6.3.5 Spin-orbit spatial mapping

Since the spectroscopy technique gives access to the spin-orbit coupling Δ_{SO}, a spatial mapping of this interaction strength can be achieved. From Eqs. (6.1) and (6.2), we deduce that for the non excited case (no spectroscopy tone) the phase shift due to the spin-orbit anticrossing $\varphi \propto {\Delta_{\mathrm{SO}}}^{-1}$. Hence, once we link a phase shift value to a spin-orbit gap using the above described spectroscopy measurement, we can access the values of this gap for the rest of magnetic field directions just by measuring the phase signal and making the correspondence.

In Fig. 6.9, we fix the magnetic field module to 0.6 T and cover the upper hemisphere field directions using a Fibonacci sphere sampling. For each direction we fit the ICT signal and extract the phase shift height. We see a clear magnetic field direction dependence of the spin-orbit coupling but we did not further extend the study to investigate this dependence.

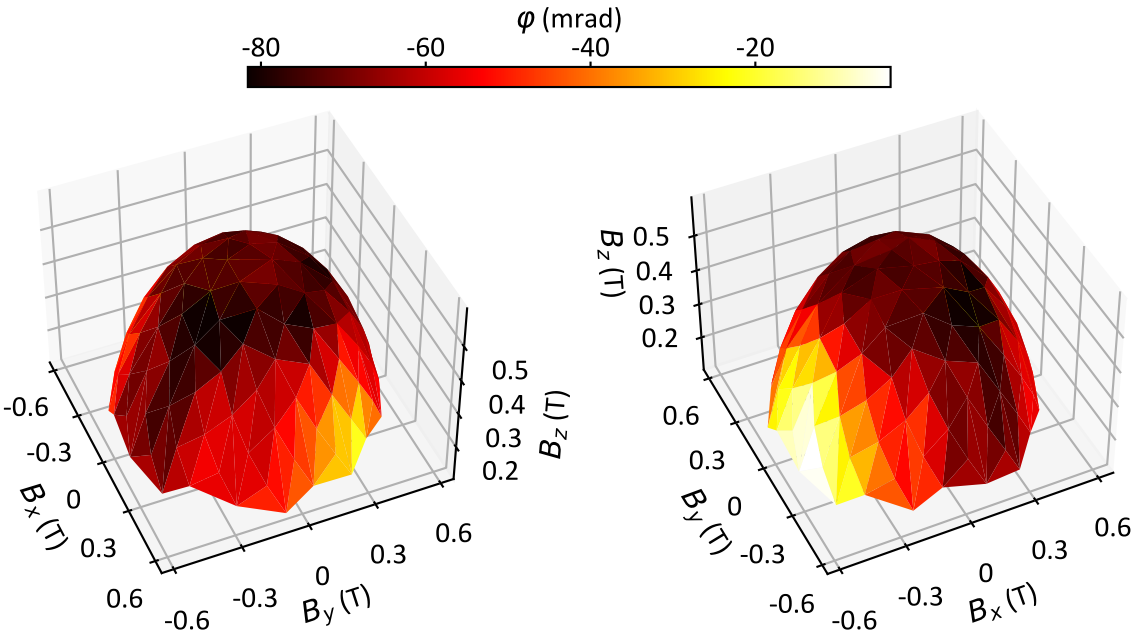

Figure 6.9 – **Spin-orbit coupling spatial mapping.** Spin-orbit phase dip height as a function of B_x (along channel), B_y (in plane perpendicular to channel) and B_z (out of plane) while keeping a constant 0.6 T magnetic field module to cover the upper field hemisphere using a Fibonacci sphere sampling. The two plots show the same data from different view angles. The spin orbit gap Δ_{SO} could be directly linked to the dip height and therefore this measurement maps spatially the spin-orbit coupling.

In conclusion, we have performed microwave magneto-spectroscopy in combination with gate-based dispersive readout of silicon hole DQDs. By modelling the DQD coupled to the LC resonator and microwave spectroscopic tone by a driven Jaynes-Cummings Hamiltonian, we derive the linear response function of the system, which qualitatively explains our experimental data. Due to the spin-orbit interaction present in the valence band of silicon, all spin-orbit

states have been revealed by two-tone spectroscopy enabling a precise reconstruction of the DQD energy diagram in both even- and odd-parity ICTs. Consequently, we were able to extract all of necessary physical parameters of a DQD, *i.e.* gate lever arms, tunnel couplings, g-factors and spin-orbit strength. The demonstrated two-tone spectroscopy and frequency multiplexed gate dispersive readout could enable parameter characterization in dense arrays of spin-orbit qubits without the need for local charge detectors and reservoirs whose integration is technically challenging. Moreover, the use of superconducting LC resonators with higher resonance frequency, Q-factor and impedance, either off-chip [59] or on-chip [156], would result in larger dispersive shifts and hence improved signal-to-noise ratios.

6.4 Extractions

6.4.1 Tunnel coupling & spin-orbit interaction

In order to get a more precise and correct extraction of the tunnel coupling and the spin-orbit interaction, we need to take into account the charge noise fluctuations impact into our fitting model.

The transition frequency (f) of a charge qubit as a function of detuning (ε) is:

$$f = \frac{\sqrt{\varepsilon^2 + \Delta^2}}{h}, \tag{6.4}$$

where h is the Planck constant and t is the tunnel coupling giving rise to an anticrossing gap Δ.

Low frequency charge noise will lead to fluctuations of the qubit transition frequency. Assuming that the noise on the detunig axis is Gaussian, its probability density function can be written as:

$$\rho_\varepsilon(\varepsilon) = \frac{1}{\sigma_\varepsilon\sqrt{2\pi}} \cdot e^{-\frac{1}{2}(\frac{\varepsilon}{\sigma_\varepsilon})^2}, \tag{6.5}$$

where σ_ε is the standard deviation of the distribution of detuning noise. To transform the probability density function of the detuning noise into the probability density function for the transition frequency, we use the following relation:

$$\rho_y(y) = \rho_x(x(y)) \cdot \frac{dx(y)}{dy}, \tag{6.6}$$

where $\rho_y(y)$ is the probability density function of y and $y(x)$ is a function of x, whose probability density function is given by $\rho_x(x)$.

Therefore, we find the following probability density function for the transition frequency:

$$\rho_f(f) = \begin{cases} 0 & , f \leq \Delta/h \\ \frac{2h^2 f}{\sigma_\varepsilon\sqrt{2\pi}} \cdot \frac{e^{-\frac{1}{2}(\frac{(hf)^2-\Delta^2}{\sigma_\varepsilon^2})}}{\sqrt{(hf)^2-\Delta^2}} & , f > \Delta/h \end{cases} \tag{6.7}$$

The factor of 2 in $\rho_f(f)$ comes from the fact that there are two solutions to Eq. (6.4) for $\varepsilon(f)$.

The linewidth of the qubit transition is given by the lifetime of the excited state (assuming that the ground state cannot decay and has infinite lifetime). From Heisenberg uncertainty principle, we know that $\Delta E \Delta t \geq \hbar$ [29]. This directly translates into a spectral width $\Delta f =$

$1/(2\pi T_1)$, where T_1 is the lifetime of the excited state. Then, the full linewidth is described by a Lorentzian centered around frequency f_0:

$$\mathcal{L}(f) = A \cdot \frac{(\frac{\Gamma}{2})^2}{(f - f_0)^2 + (\frac{\Gamma}{2})^2}, \tag{6.8}$$

where A is the amplitude of the spectral ray at $f = f_0$ and $\Gamma = \frac{1}{T_1}$ is the full width at half maximum and the lifetime of the excited state.

The final lineshape of the phase response as a function of drive frequency at an anticrossing is given by the convolution of the intrinsic lineshape of the qubit (Lorentztian characterized by T_1) and the probability density function of the transition frequencies [108]:

$$\varphi(f) = \int_{-\infty}^{+\infty} \mathcal{L}(\nu) \cdot \rho_f(f - \nu) \cdot d\nu + \varphi_0, \tag{6.9}$$

where φ_0 is a phase offset. We compute Eq. (6.9) numerically and pass it as the fitting model in order to extract the tunnel coupling at the anticrossing.

The fittings that allowed the extraction of Δ (in the case of ICT 2) and Δ_{SO} (in the case of ICT 1) are presented in Fig. 6.10. The dashed line cuts along the anticrossing detuning were taken from spectroscopy maps measured at the lowest constant room temperature power.

6.4.2 Alpha factor

By following the center of the dip-peak structure of the wings, we get the energy gap value between the ground state and the excited state for each detuning value. Fig. 6.11 illustrates the extraction of the α-factor. Starting from the calibrated spectroscopy map at zero magnetic field, we mark both the position of the central dip and the center of wing dip-peak. We align afterwards the positions corresponding to zero detuning around their mean value V_0. We can then fit alpha to the obtained wing positions with:

$$hf_{\mathrm{exc}} = \sqrt{\alpha^2(V_{\mathrm{G2}} - V_0)^2 + \Delta^2}, \tag{6.10}$$

where Δ is the anticrossing gap extracted as in Sec. 6.4.1 and input in the model as a fixed parameter.

6.4.3 Charge photon coupling

The charge photon coupling is extracted using Eq. (6.1) and Eq. (6.2) as a model. Each experimental dip in Fig. 6.12 is a 40 time average of the same measurement at zero magnetic field with no spectroscopy drive. We then fit these data while introducing the already extracted entities (α, Δ, Δ_{SO}, Q_{loaded} ...) as fixed parameters. The decoherence rate Γ is neglected here since we assume that it is small compared to the tunnelling.

6.4.4 g-factors

Due to g-factor difference between the two quantum dots, the Zeeman splitting induced by the applied magnetic field is not the same for both spins. The energies E_{f1} and E_{f2} illustrated in Fig. 6.13 represent the energies necessary to flip respectively the spin of QD 1 and the spin of QD 2. These energies give access to the g-factors knowing the applied magnetic field B since:

$$E_{\mathrm{f1}} = g_1 \mu_{\mathrm{B}} B \tag{6.11}$$

$$E_{\mathrm{f2}} = g_2 \mu_{\mathrm{B}} B \tag{6.12}$$

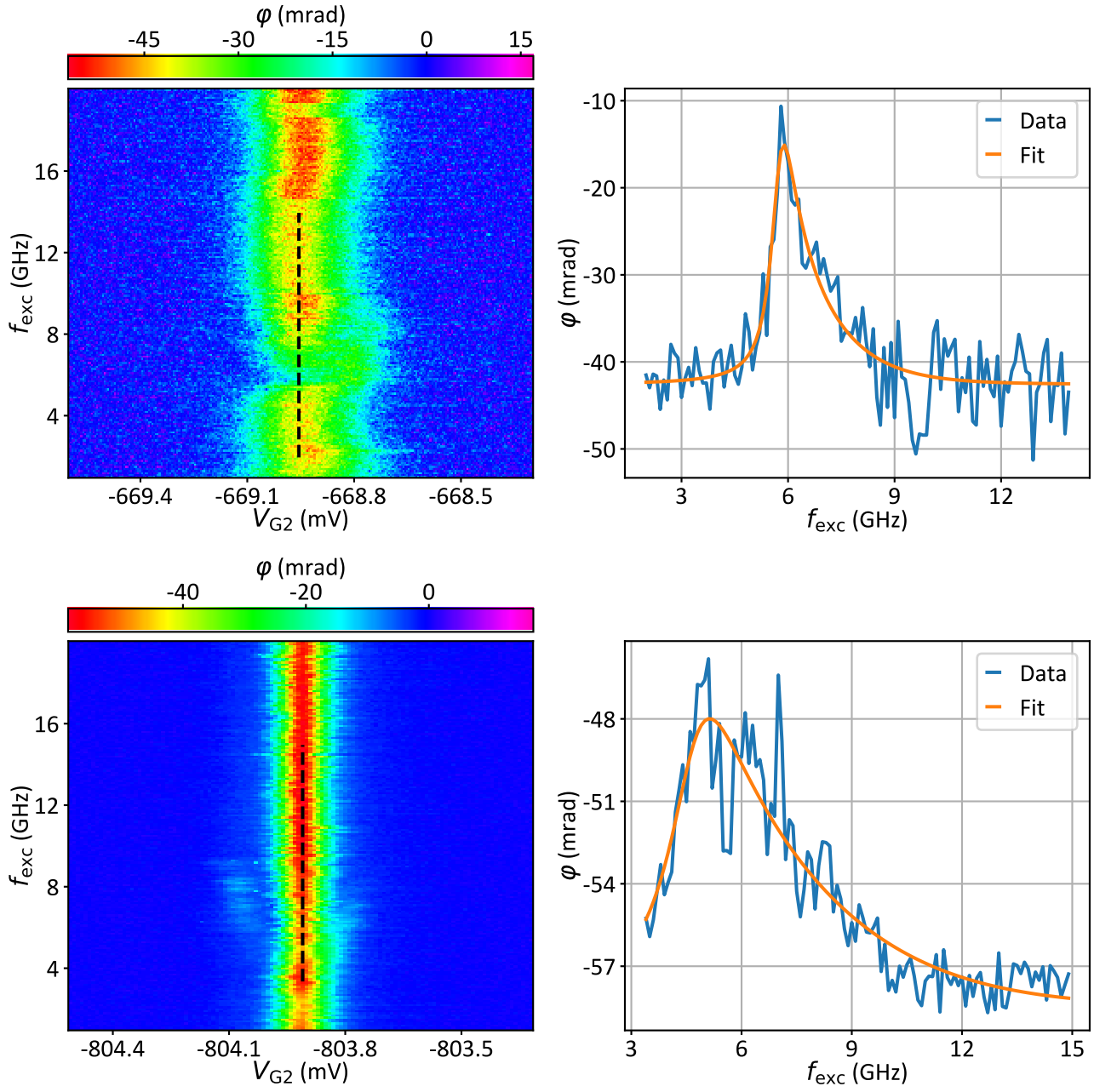

Figure 6.10 – **Tunnel coupling and spin-orbit coupling extractions.** Phase response of the LC resonator as a function of V_{G2} and f_{exc} is shown on the left in the case of ICT 1 (bottom) and ICT 2 (top) and line-cuts (black dashed lines) are shown on the right. The line-cuts are fitted with Eq. (6.9) in order to extract $\Delta = 5.72 \pm 0.04\,\text{GHz}$ (top) and $\Delta_{SO}/h = 4.6 \pm 0.1\,\text{GHz}$ (bottom).

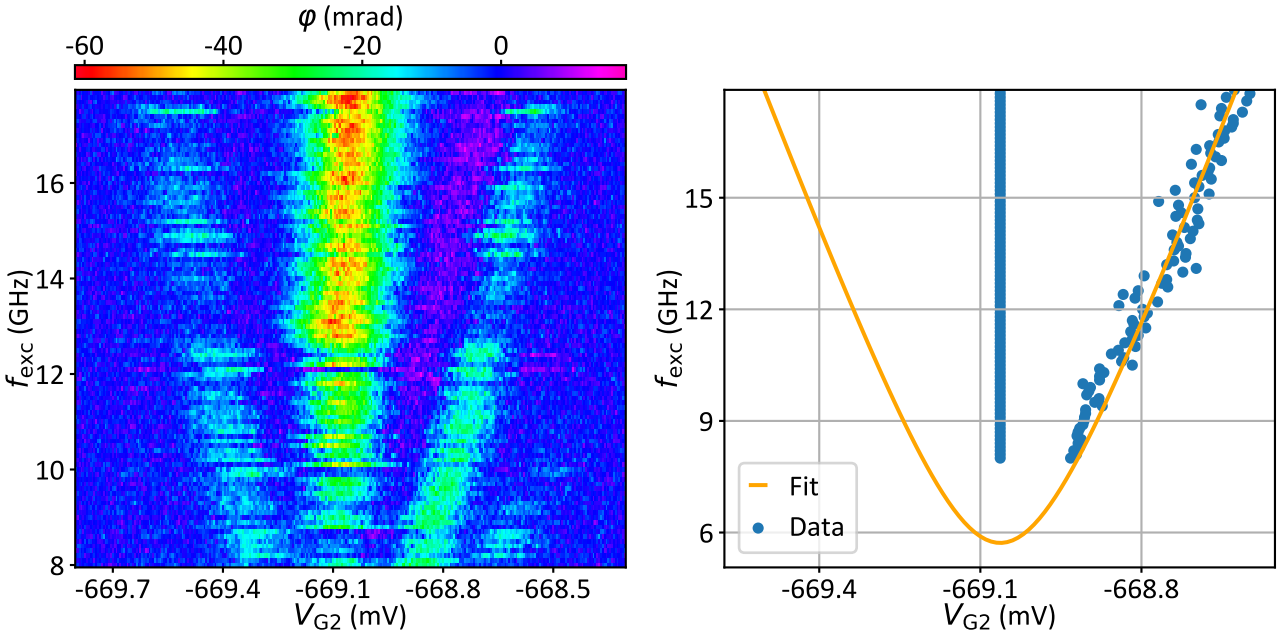

Figure 6.11 – **Alpha factor extraction.** Phase response of the LC resonator as a function of V_{G2} and f_{exc} (with power calibration) for ICT 2 is shown on the left. The scatter plot on the right retraces the positions of the central line as ell as the right dip-peak structure from the left graph. The orange curve is a fit using Eq. (6.10) and the already extracted Δ value which yields $\alpha = 0.160 \pm 0.001\,\mathrm{eV/V}$.

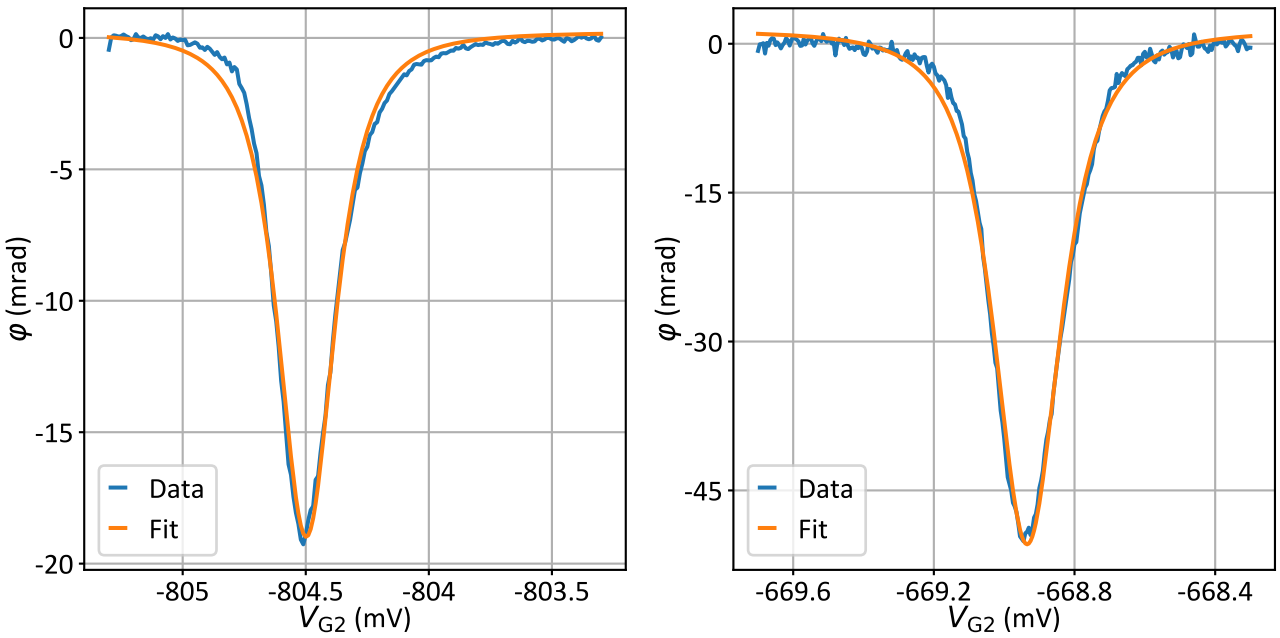

Figure 6.12 – **Charge photon coupling extraction.** The experimental data (blue) for ICT 1 (left) and ICT 2 (right) are fitted (orange) with Eq. (6.1) and Eq. (6.2) to extract $g_c = 35.2 \pm 0.1\,\mathrm{MHz}$ and $g_c = 37.4 \pm 0.1\,\mathrm{MHz}$ respectively.

E_{f1} and E_{f2} are marked on a theoretical spectroscopy map on the top panel of Fig. 6.13.

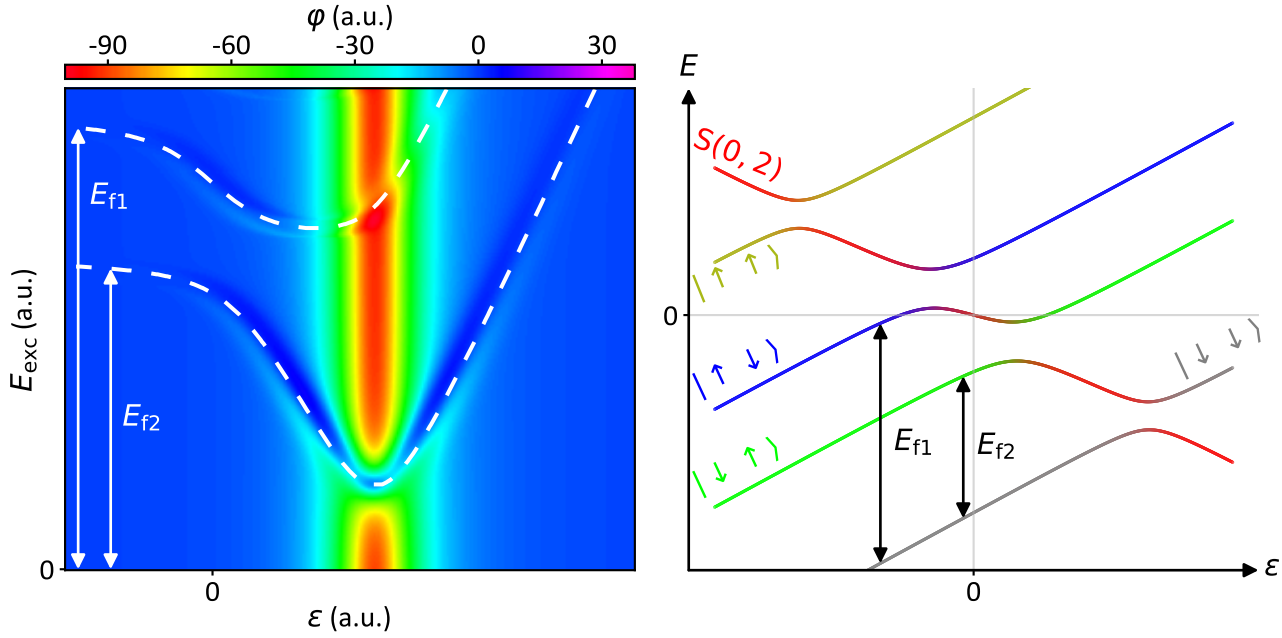

Figure 6.13 – **g-factors extraction.** Simulated response of the driven DQD system at finite magnetic field in the case of an even charge parity (left panel) and the corresponding schematic of the energy diagram (right panel) highlighting the transition energies E_{f1} and E_{f2} necessary for g-factors extraction.

Takeaway messages:

- The devices used for this experiment are p-type face-to-face.
- We achieved microwave spectroscopy in combination of gate-based dispersive readout.
- The dispersive signal is modeled using a quantum mechanical approach based on driven Jaynes-Cumming Hamiltonian.
- We obtained characteristic parameters such as g-factors, tunnel/spin-orbit couplings and α-factors enabling the reconstruction of the entire energy spectrum of the DQD necessary for qubit control and readout.
- The adopted model gives also access to the charge-photon coupling.

Conclusion

> The great art consists in devising decisive experiments, leaving no place to the imagination of the observer. Imagination is needed to give wings to thought at the beginning of experimental investigations on any given subject. When, however, the time has come to conclude, and to interpret the facts derived from observations, imagination must submit to the factual results of the experiments.
>
> Louis PASTEUR

Companies and governments are racing to be the first to own a quantum processor capable of performing useful calculations. While the global effort is to increase the number of qubits in such a processor, leading for example to the latest 53 qubit prototype developed by Google [6], this thesis takes a step back to the departure square by adopting a physical qubit implementation based on industrial-scale manufacturing, shows that such an approach has a promising potential, and introduces some tools needed for its future development.

The well known silicon properties as well as the maturity of the CMOS technology make electrostatically defined quantum dots in a silicon nanostructure a suitable host for quantum information. We presented in this thesis foundry-compatible silicon qubit devices with a relatively simple geometry. The simplicity of the investigated device layouts (face-to-face and pump geometries) led us to conclude that both control and readout are possible with a minimal number of gates and prepare the path to the operation of quantum dot arrays.

We studied p-doped devices knowing that holes in silicon offer a set of attracting properties. The possibility of an all electrical control of the qubit by taking advantage of the spin-orbit coupling, the insensitivity to the surrounding nuclear spin bath, as well as the absence of a valley-degeneracy issue as in the case of electrons make holes a compelling choice.

Combining the electrically mediated spin control with the RF gate reflectometry dispersive readout and a Pauli spin blockade based spin to charge conversion scheme, we demonstrated (Chap. 4) a fully functional hole qubit [26] which does not require any local charge sensor nor a micromagnet. The pseudospin state, mixed with the orbital component due to spin-orbit interaction, is driven coherently via EDSR using only an alternating voltage on one of the

gates. Unlike in the very first demonstration of a silicon hole spin qubit [89] where readout was performed by current transport through source and drain electrodes, here, the newly adopted readout scheme requires no current flow through the leads, which are there only to provide a reservoir of holes to populate the QDs under the gates. This simplifies the device design and operation.

The RF gate reflectometry readout technique grants higher readout speeds and good sensitivities when compared to other methods, but this comes at a price. The precision of gate electrodes when scanning for signals needs to be high in order to be able to capture the desired features in a stability diagram. For the sake of minimising measurement times that could become excessive when taking in consideration the required voltage steps, a measurement method known as video mode (VM) has been developed during this thesis and explained in Chap. 5. Its concept relies on cutting off on the communication times for each data point by acquiring continuously while sweeping the gate voltages.

Albeit the gain in device layout thanks to the electrical manipulation of hole spin state, an important difficulty arises when dealing with hole based qubits. Holes typically exhibit a large variability in their g-factors, which makes it harder to find the proper operation regime. This is particularly true in the case of dispersively probed hole qubits. The reconstruction of the energy diagram becomes then more and more difficult in contrast to the electron case where the g-factor is always bordering on 2. To address this issue, a dispersively probed microwave spectroscopy technique has been established [35] and as discussed in Chap. 6. By inducing charge transitions in a DQD system using a microwave excitation, one can access various parameters, enabling the full reconstruction of the energy diagram which will in turn pinpoint the necessary frequencies for qubit manipulation.

This thesis paves the way for a more in depth study of hole qubits in silicon. The demonstrated gate-reflectometry readout opens access to the implementation of long spin manipulation sequences, overcoming an important limitation of transport-based detection. This should enable the implementation of long echo sequences (*e.g.* CPMG) and a more accurate measurement of the characteristic spin relaxation and dephasing times. Moreover, it should enable randomized benchmarking protocols for fidelity characterization. On the devices side, reducing the size of the channel will be of a certain advantage because of the higher energy level quantization (which makes life easier) offered by stronger hole confinement. Coupling remote hole spins can also be an interesting track to pursue since long-distance quantum information transfer may open the way to new opportunities for scalable quantum architectures. Furthermore, the realisation of two-qubit gates (with our LETI devices) is yet a step to be acheived.

Optimizations on the technical level could also follow this work. By relying on a superconducting LC resonators with higher resonance frequency, Q-factor and impedance, either off-chip [59] or on-chip [156], larger dispersive shifts could be acheived leading to improved signal-to-noise ratios. Frequency multiplexing might additionally become a necessity in the near future if more than a resonator is deployed for dispersive readout. On the level of EDSR signature search, frequency chirping [114] could be deployed at the microwave signal generator so that the EDSR lines in the maps become larger and more pronounced enabling larger scanning steps and faster measurements. Moreover, knowing that the spin-orbit interaction of holes may be a source of decoherence when uncontrolled electric fields act on the DQD, chopping the reflectometry excitation and triggering the readout only for specific time lapses could help extending qubit coherence and relaxation times.

In the quest of more scalable complex structures, in the very last part of my thesis I began to investigate devices with more than two gates. In particular, I eventually focused on a pump-type device with five gates (see Fig. C.1). The LC resonator is connected to the middle gate (gate 3). We can therefore create two DQD systems, either under gate 2 and gate 3 or under gate 3 and gate 4.

By loading a small number of holes in the dots under the inner gates and then raising the voltages on the outer gates we succeeded to create a long-lasting, meta-stable regime characterized by a fixed total number of holes in the inner DQD. In practice, we start the initialization by accumulating a few holes under gate 2 and gate 3. This is achieved by setting their respective gate voltages near threshold voltage for the first hole while keeping the other gates at high filling potentials and the leads grounded. The channel is successively pinched-off by creating high tunnel barriers using positive voltages on gates 1 and 4. Doing so, we trap the holes in the DQD as they cannot escape to the leads. Fig. C.1 shows the stability diagram of such a system when the total occupation number of the DQD is four holes and five holes.

The lines with positive slopes denote ICTs extending over a very large voltage ranges in the stability diagrams of Fig. C.1. The trapped holes cannot escape to source or drain electrodes, but they can tunnel from one QD to the other. As a result, one can observe as many lines as the number of holes in the DQD. In other words, we can determine the number of holes in the DQD system simply by counting the ICTs. Such isolation protocol opens the possibility to study very few holes, or even single holes, in a DQD using RF gate reflectometry, which may lead to better coherence times and better hole qubits in general.

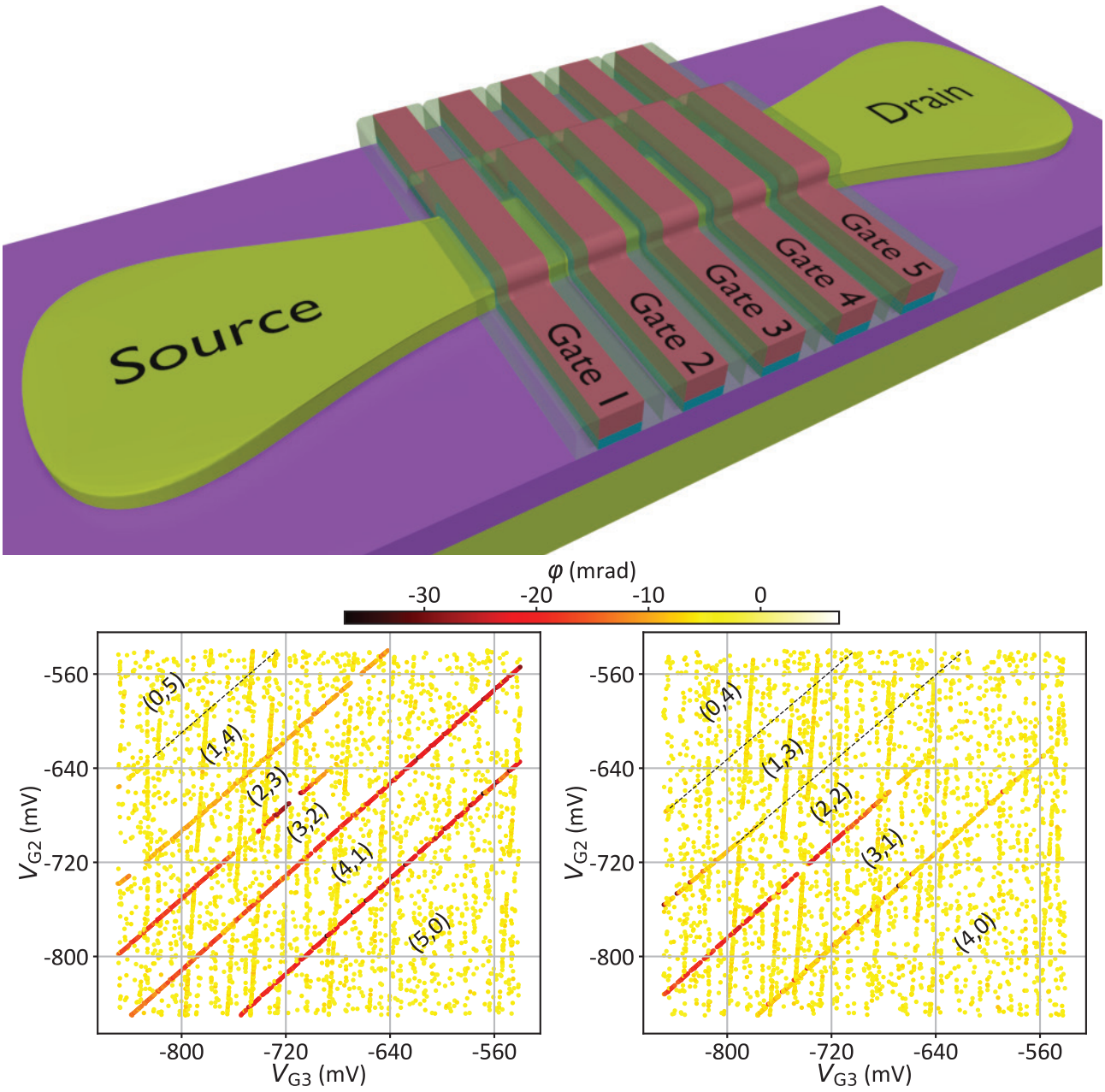

Figure C.1 – **Few holes in an isolated DQD. (Top)** Schematic illustration of a five-gate pump sample. The readout tank circuit is connected to gate 3. **(Bottom)** Phase response of the LC resonator as a function of V_{G2} and V_{G3} for two different total occupation numbers, five (left) and four (right) holes in the DQD. The maps were acquired using the VM technique. Each scattered point represents a detected peak in the scan. The ICT lines stretch over a large range of gate 2/gate 3 voltages since the holes cannot escape to the leads due to the high barriers induced by gate 1 and gate 4. (M,N) denotes the hole filling of the DQD where M (N) is the number of holes present under gate 2 (3). The dashed lines serve as eye guides for weak ICT signals.

Appendix A

Energy diagram simulation Python codes

Contents

A.1 Odd charge configuration

```
# -*- coding: utf-8 -*-
"""
Created on Wed Jan 13 18:44:52 2021

@author: Rami EZZOUCH
"""

import numpy as np
import scipy.linalg as la
import matplotlib.pyplot as plt
from matplotlib.widgets import Slider, Button

# Basis: |right up>
#        |right down>
#        |left up>
#        |left down>
Ld = [[1,0,0,0], (0,255,0)]       # green
Lu = [[0,1,0,0], (255,0,0)]       # red
Rd = [[0,0,1,0], (128,128,128)]   # gray
Ru = [[0,0,0,1], (0,0,255)]       # blue

statesNColors = [Ld,Lu,Rd,Ru]

xMultiplier = 1e6
yMultiplier = 1e6

h = 4.135667662e-15 # in eV.s
```

```
muB = 5.778381e-5 # in eV/T
kB = 8.61733e-5 # in eV/K
gr = 2
gl = 1.5
t = 12e-6 # in eV       NB: 1GHz = 4ueV
tso = 5e-6 # in eV
sgn = 1
B = 0.6

def update(val):
    global gr, gl, t, tso, sgn, fig, e0, e1, e2, e3
    B = sB.val
    gr = sGr.val
    gl = sGl.val
    t = sT.val * 1e-6
    tso = sTso.val * 1e-6
    solveEnergies(sgn, gr, gl, t, tso, B)
    plt.sca(axs[0])
    for i in range(4):
            exec("e%d.remove()" % i)
    e0 = plt.scatter(epsilonRange * xMultiplier, diagram[0] * yMultiplier,
    ↪  marker='.', s=s, linewidth=linewidth,
    ↪  c=colors[:,0,:].transpose()/255)
    e1 = plt.scatter(epsilonRange * xMultiplier, diagram[1] * yMultiplier,
    ↪  marker='.', s=s, linewidth=linewidth,
    ↪  c=colors[:,1,:].transpose()/255)
    e2 = plt.scatter(epsilonRange * xMultiplier, diagram[2] * yMultiplier,
    ↪  marker='.', s=s, linewidth=linewidth,
    ↪  c=colors[:,2,:].transpose()/255)
    e3 = plt.scatter(epsilonRange * xMultiplier, diagram[3] * yMultiplier,
    ↪  marker='.', s=s, linewidth=linewidth,
    ↪  c=colors[:,3,:].transpose()/255)

    (fig.axes[0]).set_ylim(bottom=diagram.min() * yMultiplier,
    ↪  top=diagram.max() * yMultiplier)
    fig.canvas.draw_idle()

numPointsE = 1001
epsilonRange = np.linspace(-1e-4, 1e-4, numPointsE)

def flip(event):
    global sgn
    sgn = -sgn
    update(1)

def solveEnergies(sgn, gr, gl, t, tso, B):
    global cq, diagram, colors, energies
    energies = []
    colors = []
    cq = []
```

```
69      for epsilon in epsilonRange:
70          H = np.matrix([[sgn/2*epsilon + 1/2*gr*muB*B, 0, t, -tso],
71                         [0, sgn/2*epsilon - 1/2*gr*muB*B, tso, t],
72                         [t, tso, -sgn/2*epsilon + 1/2*gl*muB*B, 0],
73                         [-tso, t, 0, -sgn/2*epsilon - 1/2*gl*muB*B]])
74          eigvals = la.eigh(H)[0]
75          eigvecs = la.eigh(H)[1].transpose()
76          energies.append(eigvals)
77          colorVect = []
78          for eigvec in eigvecs:
79              color = np.array([0,0,0])
80              for basisState in statesNColors:
81                  color = np.add(color, np.multiply(basisState[1], (eigvec @
                        ↪  basisState[0])**2))
82              colorVect.append(color)
83          colors.append(colorVect)
84      diagram = ((np.array(energies)).reshape(numPointsE, 4)).transpose()
85      colors = ((np.array(colors)).reshape(numPointsE, 4, 3)).transpose()
86
87      for i in range(4):
88          cq.append(-np.diff(np.diff(diagram[i]) / np.diff(epsilonRange)) /
             ↪  np.diff(epsilonRange)[:-1])
89      cq = ((np.array(cq)).reshape(4, numPointsE-2))
90
91  solveEnergies(sgn, gr, gl, t, tso, B)
92
93  xLabel = r'$\varepsilon$ ($\rm{\mu eV}$)'
94  yLabel = r'$E$ ($\rm{\mu eV}$)'
95
96  fig, axs = plt.subplots(2,1, constrained_layout=True)
97
98  plt.sca(axs[0])
99  axs[0].set_axisbelow(True)
100 plt.grid()
101 s = 0.2
102 linewidth = 1
103 e0 = plt.scatter(epsilonRange * xMultiplier, diagram[0] * yMultiplier,
    ↪  marker='.', s=s, linewidth=linewidth, c=colors[:,0,:].transpose()/255)
104 e1 = plt.scatter(epsilonRange * xMultiplier, diagram[1] * yMultiplier,
    ↪  marker='.', s=s, linewidth=linewidth, c=colors[:,1,:].transpose()/255)
105 e2 = plt.scatter(epsilonRange * xMultiplier, diagram[2] * yMultiplier,
    ↪  marker='.', s=s, linewidth=linewidth, c=colors[:,2,:].transpose()/255)
106 e3 = plt.scatter(epsilonRange * xMultiplier, diagram[3] * yMultiplier,
    ↪  marker='.', s=s, linewidth=linewidth, c=colors[:,3,:].transpose()/255)
107
108 plt.xlabel(xLabel)
109 plt.ylabel(yLabel)
110
111 slider_left_pad = 0.3
112 slider_lenght = 0.6
```

```
slider_height = 0.05
bottom_offsset = 0.02
factor = 0.7

plt.sca(axs[1])
plt.axis('off')

signax = plt.axes([0.7, bottom_offsset, 0.2, slider_height])
signButton = Button(signax, 'Flip', hovercolor='0.975')
signButton.on_clicked(flip)

axB = plt.axes([slider_left_pad, bottom_offsset+2*factor*slider_height,
↪  slider_lenght, slider_height])
sB = Slider(axB, r'$B$ (T)', 0, 1, valinit=B, valfmt='%g',valstep=0.01)
sB.on_changed(update)

axgl = plt.axes([slider_left_pad, bottom_offsset+4*factor*slider_height,
↪  slider_lenght, slider_height])
sGl = Slider(axgl, r'$g_{\rm{R}}$', 0, 3, valinit=gl,
↪  valfmt='%g',valstep=0.01)
sGl.on_changed(update)

axgr = plt.axes([slider_left_pad, bottom_offsset+6*factor*slider_height,
↪  slider_lenght, slider_height])
sGr = Slider(axgr, r'$g_{\rm{L}}$', 0, 3, valinit=gr,
↪  valfmt='%g',valstep=0.01)
sGr.on_changed(update)

axT = plt.axes([slider_left_pad, bottom_offsset+8*factor*slider_height,
↪  slider_lenght, slider_height])
sT = Slider(axT, r'$t$ ($\rm{\mu eV}$)', 0, 50, valinit=t*1e6,
↪  valfmt='%g',valstep=1)
sT.on_changed(update)

axTso = plt.axes([0.3, bottom_offsset+10*factor*slider_height, slider_lenght,
↪  slider_height])
sTso = Slider(axTso, r'$t_{\rm{SO}}$ ($\rm{\mu eV}$)', 0, 50,
↪  valinit=tso*1e6, valfmt='%g',valstep=1)
sTso.on_changed(update)
```

A.2 Even charge configuration

```
# -*- coding: utf-8 -*-
"""
Created on Wed Jan 13 18:44:52 2021

@author: Rami EZZOUCH
"""
import numpy as np
```

```
8  import scipy.linalg as la
9  import matplotlib.pyplot as plt
10 from matplotlib.widgets import Slider, Button
11
12 # Basis1:   S(1,1)=|UpDown - DownUp>/sqrt(2),
13 #           T-(1,1)=|DownDown>
14 #           T0(1,1)=|UpDown + DownUp>/sqrt(2)
15 #           T+(1,1)=|UpUp>
16 #           S(0,2)
17
18 # Basis2:   |down, down>
19 #           |down,up>
20 #           |up, down>
21 #           |up, up>
22 #           S(0,2)
23
24 dd = [[1,0,0,0,0], (169,185,24)] # darkesh yellow
25 du = [[0,1,0,0,0], (0,255,0)]       # green
26 ud = [[0,0,1,0,0], (0,0,255)]       # blue
27 uu = [[0,0,0,1,0], (128,128,128)]    # gray
28 s02 = [[0,0,0,0,1], (255,0,0)]       # red
29
30 # statesNColors = [s02, s11, tp11, t011, tm11]
31 statesNColors = [s02, du, uu, ud, dd]
32
33 e = 1.60217662e-19
34 h = 4.135667662e-15 # in eV.s
35 muB = 5.778381e-5 # in eV/T
36 kB = 8.61733e-5 # in eV/K
37 g1 = 1.5
38 g2 = 2.5
39 t = 10e-6 # in eV       NB: 1GHz = 4ueV
40 tso = 4e-6 # in eV
41 sgn = 1
42 B = 0.6
43
44 numPointsE = 1001
45 epsilonRange = np.linspace(-1e-4, 1e-4, numPointsE)
46
47 def update(val):
48     global gr, gl, t, tso, sgn, fig, e0, e1, e2, e3, e4
49     B = sB.val
50     gr = sGr.val
51     gl = sGl.val
52     t = sT.val * 1e-6
53     tso = sTso.val * 1e-6
54     solveEnergies(sgn, gr, gl, t, tso, B)
55     plt.sca(axs[0])
56     for i in range(5):
57             exec("e%d.remove()" % i)
```

```
58      e0 = plt.scatter(epsilonRange * xMultiplier, diagram[0] * yMultiplier,
        ↪  marker='.', s=s, linewidth=linewidth,
        ↪  c=colors[:,0,:].transpose()/255)
59      e1 = plt.scatter(epsilonRange * xMultiplier, diagram[1] * yMultiplier,
        ↪  marker='.', s=s, linewidth=linewidth,
        ↪  c=colors[:,1,:].transpose()/255)
60      e2 = plt.scatter(epsilonRange * xMultiplier, diagram[2] * yMultiplier,
        ↪  marker='.', s=s, linewidth=linewidth,
        ↪  c=colors[:,2,:].transpose()/255)
61      e3 = plt.scatter(epsilonRange * xMultiplier, diagram[3] * yMultiplier,
        ↪  marker='.', s=s, linewidth=linewidth,
        ↪  c=colors[:,3,:].transpose()/255)
62      e4 = plt.scatter(epsilonRange * xMultiplier, diagram[4] * yMultiplier,
        ↪  marker='.', s=s, linewidth=linewidth,
        ↪  c=colors[:,4,:].transpose()/255)
63
64      (fig.axes[0]).set_ylim(bottom=diagram.min() * yMultiplier,
        ↪  top=diagram.max() * yMultiplier)
65      fig.canvas.draw_idle()
66
67  numPointsE = 1001
68  epsilonRange = np.linspace(-1e-4, 1e-4, numPointsE)
69
70  def flip(event):
71      global sgn
72      sgn = -sgn
73      update(1)
74
75  def solveEnergies(sgn, g1, g2, t, tso, B):
76      global energies, cq, diagram, ct, colors
77      energies = []
78      colors = []
79      cq = []
80      ct = []
81      for epsilon in epsilonRange:
82          H = np.matrix([[sgn/2*epsilon-1/2*(g1+g2)*muB*B, 0, 0, 0, tso],
83                         [0, sgn/2*epsilon-1/2*(g1-g2)*muB*B, 0, 0, t],
84                         [0, 0, sgn/2*epsilon+1/2*(g1-g2)*muB*B, 0, t],
85                         [0, 0, 0, sgn/2*epsilon+1/2*(g1+g2)*muB*B, tso],
86                         [tso, t, t, tso, -sgn/2*epsilon]])
87          eigvals = la.eigh(H)[0]
88          eigvecs = la.eigh(H)[1].transpose()
89          energies.append(eigvals)
90          colorVect = []
91          for eigvec in eigvecs:
92              color = np.array([0,0,0])
93              for basisState in statesNColors:
94                  color = np.add(color, np.multiply(basisState[1], (eigvec @
                    ↪  basisState[0])**2))
95              colorVect.append(color)
```

```
96          colors.append(colorVect)
97      diagram = ((np.array(energies)).reshape(numPointsE, 5)).transpose()
98      colors = ((np.array(colors)).reshape(numPointsE, 5, 3)).transpose()
99      for i in range(5):
100         cq.append(-np.diff(np.diff(diagram[i]) / np.diff(epsilonRange)) /
            ↪  np.diff(epsilonRange)[:-1])
101         ct.append(np.diff(diagram[i])/np.diff(epsilonRange))
102     cq = ((np.array(cq)).reshape(5, numPointsE-2))
103     ct = ((np.array(ct)).reshape(5, numPointsE-1))
104
105 xMultiplier = 1e6
106 yMultiplier = 1e6
107
108 solveEnergies(sgn, g1, g2, t, tso, B)
109
110 xLabel = r'$\varepsilon$ ($\rm{\mu eV}$)'
111 yLabel = r'$E$ ($\rm{\mu eV}$)'
112
113 fig, axs = plt.subplots(2,1, constrained_layout=True)
114
115 plt.sca(axs[0])
116 axs[0].set_axisbelow(True)
117 plt.grid()
118
119
120 s = 0.2
121 linewidth = 1
122 e0 = plt.scatter(epsilonRange * xMultiplier, diagram[0] * yMultiplier,
    ↪  marker='.', s=s, linewidth=linewidth, c=colors[:,0,:].transpose()/255)
123 e1 = plt.scatter(epsilonRange * xMultiplier, diagram[1] * yMultiplier,
    ↪  marker='.', s=s, linewidth=linewidth, c=colors[:,1,:].transpose()/255)
124 e2 = plt.scatter(epsilonRange * xMultiplier, diagram[2] * yMultiplier,
    ↪  marker='.', s=s, linewidth=linewidth, c=colors[:,2,:].transpose()/255)
125 e3 = plt.scatter(epsilonRange * xMultiplier, diagram[3] * yMultiplier,
    ↪  marker='.', s=s, linewidth=linewidth, c=colors[:,3,:].transpose()/255)
126 e4 = plt.scatter(epsilonRange * xMultiplier, diagram[4] * yMultiplier,
    ↪  marker='.', s=s, linewidth=linewidth, c=colors[:,4,:].transpose()/255)
127
128 plt.xlabel(xLabel)
129 plt.ylabel(yLabel)
130
131 slider_left_pad = 0.3
132 slider_lenght = 0.6
133 slider_height = 0.05
134 bottom_offsset = 0.02
135 factor = 0.7
136
137 plt.sca(axs[1])
138 plt.axis('off')
139
```

```
140 signax = plt.axes([0.7, bottom_offsset, 0.2, slider_height])
141 signButton = Button(signax, 'Flip', hovercolor='0.975')
142 signButton.on_clicked(flip)
143
144 axB = plt.axes([slider_left_pad, bottom_offsset+2*factor*slider_height,
    ↪  slider_lenght, slider_height])
145 sB = Slider(axB, r'$B$ (T)', 0, 1, valinit=B, valfmt='%g',valstep=0.01)
146 sB.on_changed(update)
147
148 axgl = plt.axes([slider_left_pad, bottom_offsset+4*factor*slider_height,
    ↪  slider_lenght, slider_height])
149 sGl = Slider(axgl, r'$g_{\rm{R}}$', 0, 3, valinit=gl,
    ↪  valfmt='%g',valstep=0.01)
150 sGl.on_changed(update)
151
152 axgr = plt.axes([slider_left_pad, bottom_offsset+6*factor*slider_height,
    ↪  slider_lenght, slider_height])
153 sGr = Slider(axgr, r'$g_{\rm{L}}$', 0, 3, valinit=gr,
    ↪  valfmt='%g',valstep=0.01)
154 sGr.on_changed(update)
155
156 axT = plt.axes([slider_left_pad, bottom_offsset+8*factor*slider_height,
    ↪  slider_lenght, slider_height])
157 sT = Slider(axT, r'$t$ ($\rm{\mu eV}$)', 0, 50, valinit=t*1e6,
    ↪  valfmt='%g',valstep=1)
158 sT.on_changed(update)
159
160 axTso = plt.axes([0.3, bottom_offsset+10*factor*slider_height, slider_lenght,
    ↪  slider_height])
161 sTso = Slider(axTso, r'$t_{\rm{SO}}$ ($\rm{\mu eV}$)', 0, 50,
    ↪  valinit=tso*1e6, valfmt='%g',valstep=1)
162 sTso.on_changed(update)
```

Appendix B

Driven double quantum dot probed with a resonant electrical circuit

Contents

In this Appendix we give the details of the theoretical analysis developed by Vincent Michal relevant to Chap. 6. In Appendix B.1 we formulate the model of the driven double and in Appendix B.2 we reduce it to an effective two-state effective model that we explicitly analyze. In Appendix B.3 we express the model of the environment and compute the rates of relaxation and dephasing that enter into the master equations of Appendix B.4. Then in Appendix B.5 we compute the linear response function and the phase shift of the resonant circuit. In Appendix B.6 we extend the model to the multi-level system at arbitrary magnetic field and we include the resonant multi-photon processes in Appendix B.7.

B.1 Model of the driven double quantum dot

The DQD system is resonantly driven by a fast electrical circuit with angular frequency $\omega_{\rm exc}$ and probed by an LC circuit that is comparatively slow. The dynamics of the DQD is described by the Hamiltonian:

$$\begin{aligned}\mathcal{H} &= \hbar\omega_{\rm res}(a^\dagger a + \frac{1}{2}) \\ &+ \sum_{i=1,2}\Big[\hbar g_{ci} n_i(a+a^\dagger) + \varepsilon_i(t) n_i + \frac{U_i}{2} n_i(n_i-1)\Big] \\ &+ U_m n_1 n_2 - \sum_{\langle ij\rangle\sigma\sigma'} t_{i\sigma j\sigma'} c^\dagger_{i\sigma} c_{j\sigma'} \\ &+ \sum_{i=1,2}\frac{\mu_B}{2}(g_i \mathbf{B}_i)\cdot\sigma_i + \mathcal{H}_\kappa + \mathcal{H}_\Gamma.\end{aligned} \tag{B.1}$$

a is the microwave photon operator. $c_{i\sigma}$ is the fermion operator for dot i and effective spin projection σ, $n_i = n_{i\downarrow} + n_{i\uparrow}$ is the occupation number of dot i, and σ_i is the vector whose components are the operators $\sum_{\sigma\sigma'} c^\dagger_{i\sigma}\sigma_{\alpha\sigma\sigma'}c_{i\sigma'}$, with σ_α ($\alpha = x, y,$ and z) the Pauli matrices. The parameters of the model are:

- the time-dependent energy potential on dot i, $\varepsilon_i(t) = e\alpha_{i1}V_{\rm G1} + e\alpha_{i2}(V_{\rm G2} + V_{\rm exc}(t))$, with $V_{\rm G1}$, $V_{\rm G2}$ and $V_{\rm exc}(t) = V_{\rm exc}\cos(\omega_{\rm exc}t)$ the static and time-dependent voltages applied to gates 1 and 2. $\alpha_{ij} > 0$ is the lever arm parameter between gate j and dot i, and $e > 0$ the elementary charge.
- the spin-dependent charge tunneling matrix elements $t_{i\sigma j\sigma'}$ between the dots.
- the g-tensor g_i and the magnetic field $\mathbf{B}_i$ on dot i (μ_B being the Bohr magneton).
- the intra-dot Coulomb energies U_i and the inter-dot Coulomb energy U_m.
- the natural frequency of the probe LC circuit $\omega_{\rm res} = 1/\sqrt{L_{\rm r}C_{\rm r}}$, and the parameter of coupling between the dot charge and the quantum of the resonant circuit $\hbar g_{ci} = eV_{\rm rms}\alpha_{i1}$, with $V_{\rm rms} = \sqrt{\hbar\omega_{\rm res}/(2C_{\rm r})}$ the zero-point voltage of the LC circuit [25].

The Hamiltonians H_κ and H_Γ describe the interaction of the environment with the LC circuit and double quantum dot, respectively.

B.2 Two-state model

Let us first analyze a two-state model that describes the dynamics of the DQD in the vicinity of a single avoided crossing due to tunneling of a charge. We generalize to the multi-level DQD in Appendix B.6. Tunneling couples states with dot occupations (M, N) and $(M+1, N-1)$ that are detuned by the electrostatic energy $\varepsilon = \varepsilon_0 + (\alpha_{21} - \alpha_{11})eV_{\rm G1} + (\alpha_{22} - \alpha_{12})eV_{\rm G2} \equiv \varepsilon_0 - \alpha_1 eV_{\rm G1} + \alpha_2 eV_{\rm G2}$, where ε_0 is a constant (the detuning at zero gate voltages). Under driving, the time-dependent component of this detuning is $A_{\rm exc}\cos(\omega_{\rm exc}t)$, with $A_{\rm exc} = (\alpha_{22} - \alpha_{12})eV_{\rm exc}$. Thus the two-state Hamiltonian reads:

$$\begin{aligned}\mathcal{H} = &-\frac{\varepsilon}{2}\sigma_z - \frac{\Delta}{2}\sigma_{\rm x} - \frac{A_{\rm exc}}{2}\cos(\omega_{\rm exc}t)\sigma_z \\ &+ \hbar\omega_{\rm res}(a^\dagger a + \frac{1}{2}) + \hbar g_{\rm c}\sigma_z(a + a^\dagger) + \mathcal{H}_\kappa + \mathcal{H}_\Gamma.\end{aligned} \tag{B.2}$$

Here we use the Pauli matrix representation in the space of the charge configurations so that $\sigma_z \equiv n_1 - n_2$, $\sigma_{\rm x}$ describes tunneling (which opens an energy gap Δ), and the coupling parameter between the DQD charge and the microwave photon is:

$$\hbar g_{\rm c} = \frac{1}{2}(\alpha_{11} - \alpha_{21})eV_{\rm rms} \equiv \frac{1}{2}\alpha_1 eV_{\rm rms}. \tag{B.3}$$

The Hamiltonian Eq. (B.2) is formally equivalent to the theory of Ref. [49]. Our purpose is to adapt the model to the dispersive readout in our specific regime (Appendix B.5) and to apply it to the spectroscopy of the multi-level system (Appendix B.6). In the rotating frame of the driven system Eq. (B.2) can be transformed [49] to:

$$\begin{aligned}\tilde{\mathcal{H}} = &\frac{\hbar\omega_{\rm R}}{2}\sigma_z + \hbar\omega_{\rm res}(a^\dagger a + \frac{1}{2}) + \hbar\tilde{\chi}\sigma_z(a^\dagger a + \frac{1}{2}) \\ &+ \hbar\tilde{g}(\sigma_+ a + \sigma_- a^\dagger) + \mathcal{H}_\kappa + \tilde{\mathcal{H}}_\Gamma.\end{aligned} \tag{B.4}$$

Here the effective coupling parameter writes:

$$\tilde{g} = g_{\rm c}\cos\theta\frac{\omega_{\rm R0}}{\omega_{\rm R}}, \tag{B.5}$$

and the off-resonance frequency shift is:

$$\tilde{\chi} = -\frac{2\hbar g_c^2 \sin^2\theta}{E}\frac{\delta\omega}{\omega_R},\ \hbar\omega_{res} \ll E. \tag{B.6}$$

The above equations include the mixing factors $\cos\theta = \varepsilon/E$ and $\sin\theta = \Delta/E$, where $E = \sqrt{\varepsilon^2+\Delta^2}$ is the energy spacing of the levels near the avoided crossing. Furthermore $\omega_R = \sqrt{\delta\omega^2+\omega_{R0}^2}$ is the full Rabi angular frequency, with $\delta\omega = \omega_{exc} - E/\hbar$, $\omega_{R0} = A_{exc}\Delta/(2\hbar E)$, and $\tilde{\mathcal{H}}_\Gamma$ represents the coupling of the system to the environment in the rotating frame. We note that the off-resonance shift $\tilde{\chi}$ is taken in the adiabatic limit, which requires going beyond the rotating wave approximation [49, 157, 73, 107]. In our regime of parameters the interaction between the resonantly driven system and the probe circuit is well described by the rotating wave approximation (which is formally justified when $\omega_R - \omega_{res} \ll \omega_R + \omega_{res}$). The dot detuning range where this approximation is accurate is $\delta\varepsilon \approx A_{exc}\Delta/(4\hbar\omega_r) > \Delta$.

B.3 Coupling to the environment

As a model of dissipation we consider the coupling between the active charge in the DQD and bosonic modes that can be phonons or other modes of the environment with regular noise spectra that couple to the charge. In the charge basis the coupling between the system and its environment is described by the Hamiltonian:

$$\mathcal{H}_\Gamma = \sum_\alpha \hbar\omega_\alpha b_\alpha^\dagger b_\alpha + A\sigma_z, \tag{B.7}$$

with $A = \sum_\alpha \lambda_\alpha(b_\alpha + b_\alpha^\dagger)$, α being the index of the mode of the environment. Then the standard free evolution relaxation ($\Gamma_\downarrow$, $\Gamma_\uparrow$) and pure dephasing (Γ_φ) rates are:

$$\Gamma_\downarrow = \frac{\sin^2\theta}{\hbar^2}S_{AA}(E/\hbar), \tag{B.8a}$$

$$\Gamma_\uparrow = \frac{\sin^2\theta}{\hbar^2}S_{AA}(-E/\hbar), \tag{B.8b}$$

$$\Gamma_\varphi = \frac{2\cos^2\theta}{\hbar^2}S_{AA}(0), \tag{B.8c}$$

with $S_{AA}(\omega)$ the noise correlation function [22].

B.4 Master equations

We describe the dynamics of the probed system semi-classically with Bloch master equations. In the same dressed basis set as Eq. (B.4),

$$\begin{aligned}\langle\dot{\sigma}_-\rangle = &-i\omega_R\langle\sigma_-\rangle - 2i\tilde{\chi}\langle\sigma_-(a^\dagger a + 1/2)\rangle \\ &+ i\tilde{g}\langle\sigma_z a\rangle - \tilde{\Gamma}_2\langle\sigma_-\rangle,\end{aligned} \tag{B.9a}$$

$$\langle\dot{\sigma}_z\rangle = -2i\tilde{g}(\langle a\sigma_+\rangle - \langle a^\dagger\sigma_-\rangle) - \tilde{\Gamma}_1\langle\sigma_z\rangle + \tilde{\Gamma}_\uparrow - \tilde{\Gamma}_\downarrow. \tag{B.9b}$$

Here $\tilde{\Gamma}_2 = \tilde{\Gamma}_1/2 + \tilde{\Gamma}_\varphi$ is the total decoherence rate of the driven two-level system that includes the relaxation rate $\tilde{\Gamma}_1 = \tilde{\Gamma}_\downarrow + \tilde{\Gamma}_\uparrow$ and the pure dephasing rate $\tilde{\Gamma}_\varphi$. These rates differ from those

relevant for free evolution (Eq. (B.8)) and are found [62, 48] to be:

$$\tilde{\Gamma}_{\downarrow/\uparrow} = \frac{(1 \mp \cos\eta)^2}{4}\Gamma_\downarrow + \frac{(1 \pm \cos\eta)^2}{4}\Gamma_\uparrow + \frac{1}{2}\sin^2\eta\Gamma_\nu, \tag{B.10a}$$

$$\tilde{\Gamma}_2 = \frac{3 - \cos^2\eta}{4}\Gamma_1 + \cos^2\eta\Gamma_\varphi + \frac{1}{2}\sin^2\eta\Gamma_\nu, \tag{B.10b}$$

where $\cos\eta = \delta\omega/\omega_\mathrm{R}$ and $\sin\eta = \omega_{\mathrm{R}0}/\omega_\mathrm{R}$, $\Gamma_1 = \Gamma_\downarrow + \Gamma_\uparrow$ is the energy relaxation rate and Γ_ν is proportional to the spectral function of the noise at the Rabi frequency [62]. Within the environment model taken here the rate Γ_ν evaluates to:

$$\Gamma_\nu = \frac{2\cos^2\theta}{\hbar^2}S_{AA}(\omega_\mathrm{R}). \tag{B.11}$$

As derived in [62, 48], these expressions for the rates assume that the environment temperature T is not too small (namely, $k_B T > \hbar\omega_R$).

In fact, the photon number dependent term in Eq. (B.9a) is negligible in the linear regime and is already included in Eq. (B.4) as an oscillator shift. Moreover, for a relatively weak coupling g_c the first term on the right-hand side of Eq. (B.9b) can be neglected and the slow probe resonator does not significantly change the average population of the states. We note $D = -\langle\sigma_z\rangle = \tilde{P}_- - \tilde{P}_+$ the difference of the stationary occupation probabilities of the dressed ground and excited states, which becomes:

$$D = \frac{\tilde{\Gamma}_\downarrow - \tilde{\Gamma}_\uparrow}{\tilde{\Gamma}_1};\ 4g_\mathrm{c}^2 n_\mathrm{ph} \ll \tilde{\Gamma}_1\tilde{\Gamma}_2, \tag{B.12}$$

where n_ph is the average number of photons in the LC circuit. In this regime, with the relaxation rates defined above, we find:

$$D = \frac{-\cos\eta(\Gamma_\downarrow - \Gamma_\uparrow)}{(1 + \cos^2\eta)\Gamma_1/2 + \sin^2\eta\Gamma_\nu}. \tag{B.13}$$

This manifests population inversion in the dressed basis for $\cos\eta > 0$ ($\delta\omega > 0$) [49].

B.5 Circuit phase response

We use input-output theory [41, 22, 123, 73] in order to calculate the phase shift of the signal due to its interaction with the DQD. In the input-output approach the dynamics of the circuit mode is given by the quantum Langevin equation [41]. With the Hamiltonian of Eq. (B.4), the equation reads in the rotating frame of the incoming microwave photon of angular frequency ω_p (which is close to the natural angular frequency of the resonant circuit ω_res):

$$\dot{a} = -i(\omega_\mathrm{res} - \omega_p)a - i\tilde{\chi}\sigma_z a - i\tilde{g}\sigma_- - \frac{\kappa}{2}a - \sqrt{\kappa}b_\mathrm{in}, \tag{B.14}$$

where κ is the rate of escape of the photons and b_in is the incoming microwave photon field.

By solving Eq. (B.9a) at the frequency ω_p together with Eq. (B.13), and using the input-output relations, we obtain the coefficient of reflection between the incoming and the outgoing microwave signals:

$$r(\omega_p) = 1 + \frac{i\kappa}{\omega_\mathrm{res} - \omega_p - i\frac{\kappa}{2} + \chi(\omega_p)}, \tag{B.15}$$

where $\chi(\omega_p)$ is the charge response function obtained at second order in the oscillator-DQD coupling:

$$\chi(\omega_p) = -\Big(\tilde{\chi} + \frac{\tilde{g}^2}{\omega_\mathrm{R} - \omega_p - i\tilde{\Gamma}_2}\Big) D. \tag{B.16}$$

The real part of Eq. (B.16) yields the linear shift of the resonator frequency. When $\omega_p = \omega_\mathrm{res}$ and at linear order in the response function we get the phase shift $\delta\phi = 4\,\mathrm{Re}\,\chi(\omega_\mathrm{res})/\kappa = 4Q\,\mathrm{Re}\,\chi(\omega_\mathrm{res})/\omega_\mathrm{res}$, with $Q = \omega_\mathrm{res}/\kappa$ the quality factor of the LC resonator.

B.6 Double quantum dot spectroscopy

The above model naturally generalizes to multi-level systems, and we apply it to the spectroscopy of the DQD. We diagonalize the part of the Hamiltonian of Eq. (B.1) that does not include the drives and thus we obtain the energy levels and the corresponding states of the DQD exactly. To calculate the response of the multi-level system we sum Eq. (B.16) over all excited states. The mixing angles relevant for excited state $|\epsilon\rangle$ with energy E_ϵ are:

$$\sin\theta = \langle\gamma|(n_1 - n_2)|\epsilon\rangle = 2\langle\gamma|n_1|\epsilon\rangle = -2\langle\gamma|n_2|\epsilon\rangle, \tag{B.17a}$$
$$\cos\theta = \langle\gamma|n_1|\gamma\rangle - \langle\epsilon|n_1|\epsilon\rangle = -\langle\gamma|n_2|\gamma\rangle + \langle\epsilon|n_2|\epsilon\rangle, \tag{B.17b}$$

where $|\gamma\rangle$ is the ground state of the DQD with energy E_γ.

B.7 Multi-photon processes

The above analysis generalizes to multi-photon resonant processes. For the n-photon transition between the levels γ and ϵ we stitute [105]:

$$\begin{aligned}
\delta\omega \to \delta\omega^{(n)} &= n\omega_\mathrm{exc} - (E_\epsilon - E_\gamma)/\hbar, \\
\omega_\mathrm{R0} \to \omega_\mathrm{R0}^{(n)} &= n\omega_\mathrm{exc}|\tan\theta| J_n\Big(\frac{A_\mathrm{exc}|\cos\theta|}{\hbar\omega_\mathrm{exc}}\Big), \\
\omega_R \to \omega_R^{(n)} &= \sqrt{(\delta\omega^{(n)})^2 + (\omega_\mathrm{R0}^{(n)})^2},
\end{aligned} \tag{B.18}$$

where J_n is the n$^\mathrm{th}$ Bessel function of the first kind. For small argument it approximates as $J_n(z) \approx (z/2)^n/n!$ ($z \ll 1$). The total response is obtained by summing over all resonant photon processes $n = 1, 2, \ldots$.

Publications

1. Crippa, A., Ezzouch, R., Aprá, A., Amisse, A., Laviéville, R., Hutin, L., Bertrand, B., Vinet, M., Urdampilleta, M., Meunier, T., Sanquer, M., Jehl, X., Maurand, R., and De Franceschi, S. Gate-reflectometry dispersive readout and coherent control of a spin qubit in silicon. *Nature Communications 10*, 1 (dec 2019), 2776

2. Meunier, T., Urdampilleta, M., Niegemann, D., Jadot, B., Charion, E., Mortemousque, P.-A., Spence, C., Bertrand, B., Billiot, G., Casse, M., Hutin, L., Jacquinot, H., Pillonet, G., Rambal, N., Thonnart, Y., Amisse, A., Apra, A., Bourdet, L., Crippa, A., Ezzouch, R., Jehl, X., Maurand, R., Niquet, Y.-M., Sanquer, M., Venitucci, B., De Franceschi, S., and Vinet, M. Qubit read-out in Semiconductor quantum processors: challenges and perspectives. In *2019 IEEE International Electron Devices Meeting (IEDM)* (dec 2019), vol. 2019-Decem, IEEE, pp. 31.6.1–31.6.4

3. Niquet, Y. M., Hutin, L., Diaz, B. M., Venitucci, B., Li, J., Michal, V., Fernandez-Bada, G. T., Jacquinot, H., Amisse, A., Apra, A., Ezzouch, R., Piot, N., Vincent, E., Yu, C., Zihlmann, S., Brun-Barriere, B., Schmitt, V., Dumur, E., Maurand, R., Jehl, X., Sanquer, M., Bertrand, B., Rambal, N., Niebojewski, H., Bedecarrats, T., Casse, M., Catapano, E., Mortemousque, P. A., Thomas, C., Thonnart, Y., Billiot, G., Morel, A., Charbonnier, J., Pallegoix, L., Niegemann, D., Klemt, B., Urdampilleta, M., El Homsy, V., Nurizzo, M., Chanrion, E., Jadot, B., Spence, C., Thiney, V., Paz, B., de Franceschi, S., Vinet, M., and Meunier, T. Challenges and perspectives in the modeling of spin qubits. In *2020 IEEE International Electron Devices Meeting (IEDM)* (dec 2020), vol. 2019-Septe, IEEE, pp. 30.1.1–30.1.4

4. Apra, A., Crippa, A., Tagliaferri, M. L. V., Li, J., Ezzouch, R., Bertrand, B., Hutin, L., Rambal, N., Catapano, E., Niebojewsky, H., Bedecarrats, T., Vinet, M., Urdampilleta, M., Meunier, T., Niquet, Y. M., Dumur, E., Sanquer, M., Jehl, X., Maurand, R., and De Franceschi, S. Dispersive vs charge-sensing readout for linear quantum registers. In *2020 IEEE International Electron Devices Meeting (IEDM)* (dec 2020), IEEE, pp. 38.4.1–38.4.4

5. Ezzouch, R., Zihlmann, S., Michal, V. P., Li, J., Aprá, A., Bertrand, B., Hutin, L., Vinet, M., Urdampilleta, M., Meunier, T., Jehl, X., Niquet, Y.-M., Sanquer, M., De Franceschi, S., and Maurand, R. Dispersively probed microwave spectroscopy of a silicon hole double quantum dot. *arXiv* (dec 2020), 1–13

Bibliography

[1] Ahmed, I., Haigh, J. A., Schaal, S., Barraud, S., Zhu, Y., Lee, C.-m., Amado, M., Robinson, J. W. A., Rossi, A., Morton, J. J. L., and Gonzalez-Zalba, M. F. Radio-Frequency Capacitive Gate-Based Sensing. *Physical Review Applied 10*, 1 (jul 2018), 014018. 22, 44, 46

[2] Amasha, S., MacLean, K., Radu, I. P., Zumbühl, D. M., Kastner, M. A., Hanson, M. P., and Gossard, A. C. Electrical Control of Spin Relaxation in a Quantum Dot. *Physical Review Letters 100*, 4 (jan 2008), 046803. 23

[3] Andersen, C. K., Remm, A., Lazar, S., Krinner, S., Lacroix, N., Norris, G. J., Gabureac, M., Eichler, C., and Wallraff, A. Repeated quantum error detection in a surface code. *Nature Physics 16*, 8 (aug 2020), 875–880. 2

[4] Apra, A., Crippa, A., Tagliaferri, M. L. V., Li, J., Ezzouch, R., Bertrand, B., Hutin, L., Rambal, N., Catapano, E., Niebojewsky, H., Bedecarrats, T., Vinet, M., Urdampilleta, M., Meunier, T., Niquet, Y. M., Dumur, E., Sanquer, M., Jehl, X., Maurand, R., and De Franceschi, S. Dispersive vs charge-sensing readout for linear quantum registers. In *2020 IEEE International Electron Devices Meeting (IEDM)* (dec 2020), IEEE, pp. 38.4.1–38.4.4.

[5] Ares, N., Katsaros, G., Golovach, V. N., Zhang, J. J., Prager, A., Glazman, L. I., Schmidt, O. G., and De Franceschi, S. SiGe quantum dots for fast hole spin Rabi oscillations. *Applied Physics Letters 103*, 26 (dec 2013), 263113. 21

[6] Arute, F., Arya, K., Babbush, R., Bacon, D., Bardin, J. C., Barends, R., Biswas, R., Boixo, S., Brandao, F. G. S. L., Buell, D. A., Burkett, B., Chen, Y., Chen, Z., Chiaro, B., Collins, R., Courtney, W., Dunsworth, A., Farhi, E., Foxen, B., Fowler, A., Gidney, C., Giustina, M., Graff, R., Guerin, K., Habegger, S., Harrigan, M. P., Hartmann, M. J., Ho, A., Hoffmann, M., Huang, T., Humble, T. S., Isakov, S. V., Jeffrey, E., Jiang, Z., Kafri, D., Kechedzhi, K., Kelly, J., Klimov, P. V., Knysh, S., Korotkov, A., Kostritsa, F., Landhuis, D., Lindmark, M., Lucero, E., Lyakh, D., Mandrà, S., McClean, J. R., McEwen, M., Megrant, A., Mi, X., Michielsen, K., Mohseni, M., Mutus, J., Naaman, O., Neeley, M., Neill, C., Niu, M. Y., Ostby, E., Petukhov, A., Platt, J. C., Quintana, C., Rieffel, E. G., Roushan, P., Rubin, N. C., Sank, D., Satzinger, K. J., Smelyanskiy, V., Sung, K. J., Trevithick, M. D., Vainsencher, A., Villalonga, B., White, T., Yao, Z. J., Yeh, P., Zalcman, A., Neven, H., and Martinis, J. M. Quantum supremacy using a programmable superconducting processor. *Nature 574*, 7779 (oct 2019), 505–510. 101

[7] Barraud, S., Coquand, R., Casse, M., Koyama, M., Hartmann, J.-M., Maffini-Alvaro, V., Comboroure, C., Vizioz, C., Aussenac, F., Faynot, O., and Poiroux, T. Performance of Omega-Shaped-Gate Silicon Nanowire MOSFET With

Diameter Down to 8 nm. *IEEE Electron Device Letters 33*, 11 (nov 2012), 1526–1528. 27, 28

[8] Barthel, C., Reilly, D. J., Marcus, C. M., Hanson, M. P., and Gossard, A. C. Rapid Single-Shot Measurement of a Singlet-Triplet Qubit. *Physical Review Letters 103*, 16 (oct 2009), 160503. 50

[9] Betz, A. C., Wacquez, R., Vinet, M., Jehl, X., Saraiva, A. L., Sanquer, M., Ferguson, A. J., and Gonzalez-Zalba, M. F. Dispersively Detected Pauli Spin-Blockade in a Silicon Nanowire Field-Effect Transistor. *Nano Letters 15*, 7 (jul 2015), 4622–4627. 20, 24

[10] Blatt, R., and Wineland, D. Entangled states of trapped atomic ions. *Nature 453*, 7198 (jun 2008), 1008–1015. 4

[11] Borselli, M. G., Eng, K., Croke, E. T., Maune, B. M., Huang, B., Ross, R. S., Kiselev, A. A., Deelman, P. W., Alvarado-Rodriguez, I., Schmitz, A. E., Sokolich, M., Holabird, K. S., Hazard, T. M., Gyure, M. F., and Hunter, A. T. Pauli spin blockade in undoped Si/SiGe two-electron double quantum dots. *Applied Physics Letters 99*, 6 (aug 2011), 063109. 20

[12] Brenning, H., Kafanov, S., Duty, T., Kubatkin, S., and Delsing, P. An ultrasensitive radio-frequency single-electron transistor working up to 4.2 K. *Journal of Applied Physics 100*, 11 (2006), 114321. 23

[13] Buitelaar, M. R., Fransson, J., Cantone, A. L., Smith, C. G., Anderson, D., Jones, G. A. C., Ardavan, A., Khlobystov, A. N., Watt, A. A. R., Porfyrakis, K., and Briggs, G. A. D. Pauli spin blockade in carbon nanotube double quantum dots. *Physical Review B 77*, 24 (jun 2008), 245439. 20

[14] Bulaev, D. V., and Loss, D. Spin Relaxation and Decoherence of Holes in Quantum Dots. *Physical Review Letters 95*, 7 (aug 2005), 076805. 20

[15] Camenzind, L. C., Geyer, S., Fuhrer, A., Warburton, R. J., Zumbühl, D. M., and Kuhlmann, A. V. A spin qubit in a fin field-effect transistor. *arXiv* (mar 2021), 1–14. 20

[16] Cassidy, M. C., Dzurak, A. S., Clark, R. G., Petersson, K. D., Farrer, I., Ritchie, D. A., and Smith, C. G. Single shot charge detection using a radio-frequency quantum point contact. *Applied Physics Letters 91*, 22 (nov 2007), 222104. 23

[17] Celler, G. K., and Cristoloveanu, S. Frontiers of silicon-on-insulator. *Journal of Applied Physics 93*, 9 (may 2003), 4955–4978. 28

[18] Chatterjee, A., Stevenson, P., De Franceschi, S., Morello, A., de Leon, N., and Kuemmeth, F. Semiconductor Qubits In Practice. *arXiv* (may 2020), 1–27. 4

[19] Cheong, H. D., Fujisawa, T., Hayashi, T., Hirayama, Y., and Jeong, Y. H. Impedance analysis of a radio-frequency single-electron transistor. *Applied Physics Letters 81*, 17 (oct 2002), 3257–3259. 22, 23

[20] Ciccarelli, C., and Ferguson, A. J. Impedance of the single-electron transistor at radio-frequencies. *New Journal of Physics 13*, 9 (sep 2011), 093015. 23

[21] Clarke, J., and Wilhelm, F. K. Superconducting quantum bits. *Nature 453*, 7198 (jun 2008), 1031–1042. 4

[22] Clerk, A. A., Devoret, M. H., Girvin, S. M., Marquardt, F., and Schoelkopf, R. J. Introduction to quantum noise, measurement, and amplification. *Reviews of Modern Physics 82*, 2 (apr 2010), 1155–1208. 115, 116

[23] Colless, J. I., Mahoney, A. C., Hornibrook, J. M., Doherty, A. C., Lu, H., Gossard, A. C., and Reilly, D. J. Dispersive Readout of a Few-Electron Double Quantum Dot with Fast rf Gate Sensors. *Physical Review Letters 110*, 4 (jan 2013), 046805. 23, 81

[24] Consortium, E. Quantum Manifesto, may 2016. 3

[25] Cottet, A., Mora, C., and Kontos, T. Mesoscopic admittance of a double quantum dot. *Physical Review B 83*, 12 (mar 2011), 121311. 81, 114

[26] Crippa, A., Ezzouch, R., Aprá, A., Amisse, A., Laviéville, R., Hutin, L., Bertrand, B., Vinet, M., Urdampilleta, M., Meunier, T., Sanquer, M., Jehl, X., Maurand, R., and De Franceschi, S. Gate-reflectometry dispersive readout and coherent control of a spin qubit in silicon. *Nature Communications 10*, 1 (dec 2019), 2776. 5, 6, 20, 22, 53, 85, 101

[27] Crippa, A., Maurand, R., Bourdet, L., Kotekar-Patil, D., Amisse, A., Jehl, X., Sanquer, M., Laviéville, R., Bohuslavskyi, H., Hutin, L., Barraud, S., Vinet, M., Niquet, Y.-M., and De Franceschi, S. Electrical Spin Driving by g-Matrix Modulation in Spin-Orbit Qubits. *Physical Review Letters 120*, 13 (mar 2018), 137702. 5, 21, 54, 58, 59, 63

[28] Crippa, A., Maurand, R., Kotekar-Patil, D., Corna, A., Bohuslavskyi, H., Orlov, A. O., Fay, P., Laviéville, R., Barraud, S., Vinet, M., Sanquer, M., De Franceschi, S., and Jehl, X. Level Spectrum and Charge Relaxation in a Silicon Double Quantum Dot Probed by Dual-Gate Reflectometry. *Nano Letters 17*, 2 (feb 2017), 1001–1006. 23, 24, 54

[29] Demtröder, W. *Experimentalphysik 3: Atome, Moleküle und Festkörper*. Springer-Lehrbuch. Springer Berlin Heidelberg, 2016. 94

[30] DiVincenzo, D. P. The Physical Implementation of Quantum Computation. *Fortschritte der Physik 48*, 9-11 (sep 2000), 771–783. 4

[31] Dutt, M. V. G., Childress, L., Jiang, L., Togan, E., Maze, J., Jelezko, F., Zibrov, A. S., Hemmer, P. R., and Lukin, M. D. Quantum Register Based on Individual Electronic and Nuclear Spin Qubits in Diamond. *Science 316*, 5829 (jun 2007), 1312–1316. 4

[32] Duty, T., Johansson, G., Bladh, K., Gunnarsson, D., Wilson, C., and Delsing, P. Observation of Quantum Capacitance in the Cooper-Pair Transistor. *Physical Review Letters 95*, 20 (nov 2005), 206807. 24, 80

[33] Elzerman, J. M., Hanson, R., Willems van Beveren, L. H., Witkamp, B., Vandersypen, L. M. K., and Kouwenhoven, L. P. Single-shot read-out of an individual electron spin in a quantum dot. *Nature 430*, 6998 (jul 2004), 431–435. 17, 18

[34] Engel, H.-A., Golovach, V. N., Loss, D., Vandersypen, L. M. K., Elzerman, J. M., Hanson, R., and Kouwenhoven, L. P. Measurement Efficiency and n-Shot Readout of Spin Qubits. *Physical Review Letters 93*, 10 (sep 2004), 106804. 17

[35] Ezzouch, R., Zihlmann, S., Michal, V. P., Li, J., Aprá, A., Bertrand, B., Hutin, L., Vinet, M., Urdampilleta, M., Meunier, T., Jehl, X., Niquet, Y.-M., Sanquer, M., De Franceschi, S., and Maurand, R. Dispersively probed microwave spectroscopy of a silicon hole double quantum dot. *arXiv* (dec 2020), 1–13. 6, 22, 102

[36] Feynman, R. P. Simulating physics with computers. *International Journal of Theoretical Physics 21*, 6-7 (jun 1982), 467–488. 1

[37] Fischer, J., Coish, W. A., Bulaev, D. V., and Loss, D. Spin decoherence of a heavy hole coupled to nuclear spins in a quantum dot. *Physical Review B 78*, 15 (oct 2008), 155329. 5

[38] Fowler, A. G., Mariantoni, M., Martinis, J. M., and Cleland, A. N. Surface codes: Towards practical large-scale quantum computation. *Physical Review A 86*, 3 (sep 2012), 032324. 2

[39] Friesen, M., Tahan, C., Joynt, R., and Eriksson, M. A. Spin Readout and Initialization in a Semiconductor Quantum Dot. *Physical Review Letters 92*, 3 (jan 2004), 037901. 17

[40] Froning, F. N. M., Camenzind, L. C., van der Molen, O. A. H., Li, A., Bakkers, E. P. A. M., Zumbühl, D. M., and Braakman, F. R. Ultrafast hole spin qubit with gate-tunable spin–orbit switch functionality. *Nature Nanotechnology* (jan 2021). 5

[41] Gardiner, C., and Zoller, P. *Quantum noise : a handbook of Markovian and non-Markovian quantum stochastic methods with applications to quantum optics*, 3 ed. Springer, Berlin, 2004. 116

[42] Golovach, V. N., Borhani, M., and Loss, D. Electric-dipole-induced spin resonance in quantum dots. *Physical Review B 74*, 16 (oct 2006), 165319. 20

[43] Golovach, V. N., Khaetskii, A., and Loss, D. Phonon-Induced Decay of the Electron Spin in Quantum Dots. *Physical Review Letters 93*, 1 (jun 2004), 016601. 20

[44] Gonzalez-Zalba, M. F., Barraud, S., Ferguson, a. J., and Betz, a. C. Probing the limits of gate-based charge sensing. *Nature Communications 6*, 1 (may 2015), 6084. 23, 24

[45] Gonzalez-Zalba, M. F., de Franceschi, S., Charbon, E., Meunier, T., Vinet, M., and Dzurak, A. S. Scaling silicon-based quantum computing using CMOS technology: State-of-the-art, Challenges and Perspectives. *arXiv* (nov 2020), 1–16. 5

[46] Greentree, A. D., Hamilton, A. R., Hollenberg, L. C. L., and Clark, R. G. Electrical readout of a spin qubit without double occupancy. *Physical Review B 71*, 11 (mar 2005), 113310. 17

[47] Hanson, R., Kouwenhoven, L. P., Petta, J. R., Tarucha, S., and Vandersypen, L. M. K. Spins in few-electron quantum dots. *Reviews of Modern Physics 79*, 4 (oct 2007), 1217–1265. 9, 11, 15

[48] Hauss, J., Fedorov, A., André, S., Brosco, V., Hutter, C., Kothari, R., Yeshwanth, S., Shnirman, A., and Schön, G. Dissipation in circuit quantum electrodynamics: lasing and cooling of a low-frequency oscillator. *New Journal of Physics 10*, 9 (sep 2008), 095018. 116

[49] Hauss, J., Fedorov, A., Hutter, C., Shnirman, A., and Schön, G. Single-Qubit Lasing and Cooling at the Rabi Frequency. *Physical Review Letters 100*, 3 (jan 2008), 037003. 114, 115, 116

[50] Hendrickx, N. W., Franke, D. P., Sammak, A., Scappucci, G., and Veldhorst, M. Fast two-qubit logic with holes in germanium. *Nature 577*, 7791 (jan 2020), 487–491. 5

[51] Hendrickx, N. W., Lawrie, W. I. L., Petit, L., Sammak, A., Scappucci, G., and Veldhorst, M. A single-hole spin qubit. *Nature Communications 11*, 1 (dec 2020), 3478. 5, 23

[52] Hendrickx, N. W., Lawrie, W. I. L., Russ, M., van Riggelen, F., de Snoo, S. L., Schouten, R. N., Sammak, A., Scappucci, G., and Veldhorst, M. A four-qubit germanium quantum processor. *Nature 591*, 7851 (mar 2021), 580–585. 5, 20, 23

[53] Higginbotham, A. P., Larsen, T. W., Yao, J., Yan, H., Lieber, C. M., Marcus, C. M., and Kuemmeth, F. Hole Spin Coherence in a Ge/Si Heterostructure Nanowire. *Nano Letters 14*, 6 (jun 2014), 3582–3586. 66

[54] Hornibrook, J. M., Colless, J. I., Mahoney, A. C., Croot, X. G., Blanvillain, S., Lu, H., Gossard, A. C., and Reilly, D. J. Frequency multiplexing for readout of spin qubits. *Applied Physics Letters 104*, 10 (mar 2014), 103108. 22

[55] House, M. G., Kobayashi, T., Weber, B., Hile, S. J., Watson, T. F., van der Heijden, J., Rogge, S., and Simmons, M. Y. Radio frequency measurements of tunnel couplings and singlet–triplet spin states in Si:P quantum dots. *Nature Communications 6*, 1 (dec 2015), 8848. 43

[56] Hu, Y., Kuemmeth, F., Lieber, C. M., and Marcus, C. M. Hole spin relaxation in Ge–Si core–shell nanowire qubits. *Nature Nanotechnology 7*, 1 (jan 2012), 47–50. 66

[57] Huang, W., Yang, C. H., Chan, K. W., Tanttu, T., Hensen, B., Leon, R. C. C., Fogarty, M. A., Hwang, J. C. C., Hudson, F. E., Itoh, K. M., Morello, A., Laucht, A., and Dzurak, A. S. Fidelity benchmarks for two-qubit gates in silicon. *Nature 569*, 7757 (may 2019), 532–536. 5

[58] Hutin, L., Bertrand, B., Maurand, R., Crippa, A., Urdampilleta, M., Kim, Y., Amisse, A., Bohuslavskyi, H., Bourdet, L., Barraud, S., Jeh, X., Niquet, Y.-M., Sanquer, M., Bauerle, C., Meunier, T., De Franceschi, S., and Vinet, M. Si MOS technology for spin-based quantum computing. In *2018 48th European Solid-State Device Research Conference (ESSDERC)* (sep 2018), IEEE, pp. 12–17. 5

[59] Ibberson, D. J., Lundberg, T., Haigh, J. A., Hutin, L., Bertrand, B., Barraud, S., Lee, C.-M., Stelmashenko, N. A., Robinson, J. W. A., Vinet, M., Gonzalez-Zalba, M. F., and Ibberson, L. A. Large dispersive interaction between a CMOS double quantum dot and microwave photons. *arXiv* (apr 2020), 1–9. 94, 102

[60] Ilani, S., Donev, L. a. K., Kindermann, M., and McEuen, P. L. Measurement of the quantum capacitance of interacting electrons in carbon nanotubes. *Nature Physics 2*, 10 (oct 2006), 687–691. 22

[61] Ionicioiu, R., and Popescu, A. E. Single-spin measurement using spin–orbital entanglement. *New Journal of Physics 7* (may 2005), 120–120. 17

[62] Ithier, G., Collin, E., Joyez, P., Meeson, P. J., Vion, D., Esteve, D., Chiarello, F., Shnirman, A., Makhlin, Y., Schriefl, J., and Schön, G. Decoherence in a superconducting quantum bit circuit. *Physical Review B 72*, 13 (oct 2005), 134519. 116

[63] Jelezko, F., and Wrachtrup, J. Single defect centres in diamond: A review. *physica status solidi (a) 203*, 13 (oct 2006), 3207–3225. 4

[64] Johnson, A. C., Petta, J. R., Marcus, C. M., Hanson, M. P., and Gossard, A. C. Singlet-triplet spin blockade and charge sensing in a few-electron double quantum dot. *Physical Review B 72*, 16 (oct 2005), 165308. 20

[65] Jones, C., Fogarty, M. A., Morello, A., Gyure, M. F., Dzurak, A. S., and Ladd, T. D. Logical Qubit in a Linear Array of Semiconductor Quantum Dots. *Physical Review X 8*, 2 (jun 2018), 021058. 5

[66] Jung, M., Schroer, M. D., Petersson, K. D., and Petta, J. R. Radio frequency charge sensing in InAs nanowire double quantum dots. *Applied Physics Letters 100*, 25 (jun 2012), 253508. 24

[67] Kane, B. E. A silicon-based nuclear spin quantum computer. *Nature 393*, 6681 (may 1998), 133–137. 5, 17

[68] Kato, Y., Myers, R. C., Driscoll, D. C., Gossard, A. C., Levy, J., and Awschalom, D. D. Gigahertz Electron Spin Manipulation Using Voltage-Controlled g-Tensor Modulation. *Science 299*, 5610 (feb 2003), 1201–1204. 21

[69] Kawakami, E., Scarlino, P., Ward, D. R., Braakman, F. R., Savage, D. E., Lagally, M. G., Friesen, M., Coppersmith, S. N., Eriksson, M. A., and Vandersypen, L. M. K. Electrical control of a long-lived spin qubit in a Si/SiGe quantum dot. *Nature Nanotechnology 9*, 9 (sep 2014), 666–670. 4, 5

[70] Keith, D., Gorman, S. K., Kranz, L., He, Y., Keizer, J. G., Broome, M. A., and Simmons, M. Y. Benchmarking high fidelity single-shot readout of semiconductor qubits. *New Journal of Physics 21*, 6 (jun 2019), 063011. 50

[71] Keith, D., House, M. G., Donnelly, M. B., Watson, T. F., Weber, B., and Simmons, M. Y. Single-Shot Spin Readout in Semiconductors Near the Shot-Noise Sensitivity Limit. *Physical Review X 9*, 4 (oct 2019), 041003. 23, 45

[72] Khaetskii, A. V., and Nazarov, Y. V. Spin relaxation in semiconductor quantum dots. *Physical Review B 61*, 19 (may 2000), 12639–12642. 20

[73] Kohler, S. Dispersive readout: Universal theory beyond the rotating-wave approximation. *Physical Review A 98*, 2 (aug 2018), 023849. 115, 116

[74] Kok, P., Munro, W. J., Nemoto, K., Ralph, T. C., Dowling, J. P., and Milburn, G. J. Linear optical quantum computing with photonic qubits. *Reviews of Modern Physics 79*, 1 (jan 2007), 135–174. 4

[75] Koppens, F. H. L., Buizert, C., Tielrooij, K. J., Vink, I. T., Nowack, K. C., Meunier, T., Kouwenhoven, L. P., and Vandersypen, L. M. K. Driven coherent oscillations of a single electron spin in a quantum dot. *Nature 442*, 7104 (aug 2006), 766–771. 5, 21

[76] Kotekar-Patil, D., Corna, A., Maurand, R., Crippa, A., Orlov, A., Barraud, S., Hutin, L., Vinet, M., Jehl, X., De Franceschi, S., and Sanquer, M. Pauli spin blockade in CMOS double quantum dot devices. *physica status solidi (b) 254*, 3 (mar 2017), 1600581. 20

[77] Kouwenhoven, L. P., Austing, D. G., and Tarucha, S. Few-electron quantum dots. *Reports on Progress in Physics 64*, 6 (jun 2001), 701–736. 10

[78] Lai, N. S., Lim, W. H., Yang, C. H., Zwanenburg, F. A., Coish, W. A., Qassemi, F., Morello, A., and Dzurak, A. S. Pauli Spin Blockade in a Highly Tunable Silicon Double Quantum Dot. *Scientific Reports 1*, 1 (dec 2011), 110. 20

[79] Laird, E. A., Pei, F., and Kouwenhoven, L. P. A valley–spin qubit in a carbon nanotube. *Nature Nanotechnology 8*, 8 (aug 2013), 565–568. 4

[80] Lasky, J. B. Wafer bonding for silicon-on-insulator technologies. *Applied Physics Letters 48*, 1 (jan 1986), 78–80. 28

[81] Lawrie, W. I. L., Hendrickx, N. W., van Riggelen, F., Russ, M., Petit, L., Sammak, A., Scappucci, G., and Veldhorst, M. Spin Relaxation Benchmarks and Individual Qubit Addressability for Holes in Quantum Dots. *Nano Letters 20*, 10 (oct 2020), 7237–7242. 5

[82] Li, R., Hudson, F. E., Dzurak, A. S., and Hamilton, A. R. Pauli Spin Blockade of Heavy Holes in a Silicon Double Quantum Dot. *Nano Letters 15*, 11 (nov 2015), 7314–7318. 20

[83] Li, R., Petit, L., Franke, D. P., Dehollain, J. P., Helsen, J., Steudtner, M., Thomas, N. K., Yoscovits, Z. R., Singh, K. J., Wehner, S., Vandersypen, L. M. K., Clarke, J. S., and Veldhorst, M. A crossbar network for silicon quantum dot qubits. *Science Advances 4*, 7 (jul 2018), eaar3960. 5, 66

[84] Loss, D., and DiVincenzo, D. P. Quantum computation with quantum dots. *Physical Review A 57*, 1 (jan 1998), 120–126. 4, 17

[85] Lu, W., Ji, Z., Pfeiffer, L., West, K. W., and Rimberg, a. J. Real-time detection of electron tunnelling in a quantum dot. *Nature 423*, 6938 (may 2003), 422–425. 23

[86] Lundberg, T., Li, J., Hutin, L., Bertrand, B., Ibberson, D. J., Lee, C.-M., Niegemann, D. J., Urdampilleta, M., Stelmashenko, N., Meunier, T., Robinson, J. W., Ibberson, L., Vinet, M., Niquet, Y.-M., and Gonzalez-Zalba, M. F. Spin Quintet in a Silicon Double Quantum Dot: Spin Blockade and Relaxation. *Physical Review X 10*, 4 (oct 2020), 041010. 20

[87] Marquardt, F., and Abalmassov, V. A. Spin relaxation in a quantum dot due to Nyquist noise. *Physical Review B 71*, 16 (apr 2005), 165325. 20

[88] Maune, B. M., Borselli, M. G., Huang, B., Ladd, T. D., Deelman, P. W., Holabird, K. S., Kiselev, A. A., Alvarado-Rodriguez, I., Ross, R. S., Schmitz, A. E., Sokolich, M., Watson, C. A., Gyure, M. F., and Hunter, A. T. Coherent singlet-triplet oscillations in a silicon-based double quantum dot. *Nature 481*, 7381 (jan 2012), 344–347. 23

[89] Maurand, R., Jehl, X., Kotekar-Patil, D., Corna, A., Bohuslavskyi, H., Laviéville, R., Hutin, L., Barraud, S., Vinet, M., Sanquer, M., and De Franceschi, S. A CMOS silicon spin qubit. *Nature Communications 7*, 1 (dec 2016), 13575. 5, 20, 30, 54, 58, 63, 102

[90] Meunier, T., Urdampilleta, M., Niegemann, D., Jadot, B., Charion, E., Mortemousque, P.-A., Spence, C., Bertrand, B., Billiot, G., Casse, M., Hutin, L., Jacquinot, H., Pillonet, G., Rambal, N., Thonnart, Y., Amisse, A., Apra, A., Bourdet, L., Crippa, A., Ezzouch, R., Jehl, X., Maurand, R., Niquet, Y.-M., Sanquer, M., Venitucci, B., De Franceschi, S., and Vinet, M. Qubit read-out in Semiconductor quantum processors: challenges and perspectives. In *2019 IEEE International Electron Devices Meeting (IEDM)* (dec 2019), vol. 2019-Decem, IEEE, pp. 31.6.1–31.6.4.

[91] Mi, X., Kohler, S., and Petta, J. R. Landau-Zener interferometry of valley-orbit states in Si/SiGe double quantum dots. *Physical Review B 98*, 16 (oct 2018), 161404. 61

[92] Mi, X., Péterfalvi, C. G., Burkard, G., and Petta, J. R. High-Resolution Valley Spectroscopy of Si Quantum Dots. *Physical Review Letters 119*, 17 (oct 2017), 176803. 85

[93] Mizuta, R., Otxoa, R. M., Betz, A. C., and Gonzalez-Zalba, M. F. Quantum and tunneling capacitance in charge and spin qubits. *Physical Review B 95*, 4 (jan 2017), 045414. 24, 55, 57, 80, 81

[94] Morello, A., Pla, J. J., Zwanenburg, F. A., Chan, K. W., Tan, K. Y., Huebl, H., Möttönen, M., Nugroho, C. D., Yang, C., van Donkelaar, J. A., Alves, A. D. C., Jamieson, D. N., Escott, C. C., Hollenberg, L. C. L., Clark, R. G., and Dzurak, A. S. Single-shot readout of an electron spin in silicon. *Nature 467*, 7316 (oct 2010), 687–691. 18

[95] Mortemousque, P.-A., Chanrion, E., Jadot, B., Flentje, H., Ludwig, A., Wieck, A. D., Urdampilleta, M., Bäuerle, C., and Meunier, T. Coherent control of individual electron spins in a two-dimensional quantum dot array. *Nature Nanotechnology* (dec 2020). 23

[96] Muhonen, J. T., Dehollain, J. P., Laucht, A., Hudson, F. E., Kalra, R., Sekiguchi, T., Itoh, K. M., Jamieson, D. N., McCallum, J. C., Dzurak, A. S., and Morello, A. Storing quantum information for 30 seconds in a nanoelectronic device. *Nature Nanotechnology 9*, 12 (dec 2014), 986–991. 5

[97] Mutter, P. M., and Burkard, G. A natural heavy-hole flopping mode qubit in germanium. *arXiv* (dec 2020). 14

[98] Nadj-Perge, S., Frolov, S. M., Bakkers, E. P. A. M., and Kouwenhoven, L. P. Spin–orbit qubit in a semiconductor nanowire. *Nature 468*, 7327 (dec 2010), 1084–1087. 20, 21, 56

[99] Nadj-Perge, S., Pribiag, V. S., van den Berg, J. W. G., Zuo, K., Plissard, S. R., Bakkers, E. P. A. M., Frolov, S. M., and Kouwenhoven, L. P. Spectroscopy of Spin-Orbit Quantum Bits in Indium Antimonide Nanowires. *Physical Review Letters 108*, 16 (apr 2012), 166801. 56

[100] Nakashima, S., Katayama, T., Miyamura, Y., Matsuzaki, A., Kataoka, M., Ebi, D., Imai, M., Izumi, K., and Ohwada, N. Investigations on High-Temperature Thermal Oxidation Process at Top and Bottom Interfaces of Top Silicon of SIMOX Wafers. *Journal of The Electrochemical Society 143*, 1 (jan 1996), 244–251. 28

[101] Nilsson, H. A., Duty, T., Abay, S., Wilson, C., Wagner, J. B., Thelander, C., Delsing, P., and Samuelson, L. A Radio Frequency Single-Electron Transistor Based on an InAs/InP Heterostructure Nanowire. *Nano Letters 8*, 3 (mar 2008), 872–875. 23

[102] Niquet, Y. M., Hutin, L., Diaz, B. M., Venitucci, B., Li, J., Michal, V., Fernandez-Bada, G. T., Jacquinot, H., Amisse, A., Apra, A., Ezzouch, R., Piot, N., Vincent, E., Yu, C., Zihlmann, S., Brun-Barriere, B., Schmitt, V., Dumur, E., Maurand, R., Jehl, X., Sanquer, M., Bertrand, B., Rambal, N., Niebojewski, H., Bedecarrats, T., Casse, M., Catapano, E., Mortemousque, P. A., Thomas, C., Thonnart, Y., Billiot, G., Morel, A., Charbonnier, J., Pallegoix, L., Niegemann, D., Klemt, B., Urdampilleta, M., El Homsy, V., Nurizzo, M., Chanrion, E., Jadot, B., Spence, C., Thiney, V., Paz, B., de Franceschi, S., Vinet, M., and Meunier, T. Challenges and perspectives in the modeling of spin qubits. In *2020 IEEE International Electron Devices Meeting (IEDM)* (dec 2020), vol. 2019-Septe, IEEE, pp. 30.1.1–30.1.4.

[103] Nowack, K. C., Koppens, F. H. L., Nazarov, Y. V., and Vandersypen, L. M. K. Coherent Control of a Single Electron Spin with Electric Fields. *Science 318*, 5855 (nov 2007), 1430–1433. 5, 20, 21

[104] Ono, K. Current Rectification by Pauli Exclusion in a Weakly Coupled Double Quantum Dot System. *Science 297*, 5585 (aug 2002), 1313–1317. 18

[105] Ono, K., Giavaras, G., Tanamoto, T., Ohguro, T., Hu, X., and Nori, F. Hole Spin Resonance and Spin-Orbit Coupling in a Silicon Metal-Oxide-Semiconductor Field-Effect Transistor. *Physical Review Letters 119*, 15 (oct 2017), 156802. 117

[106] Pakkiam, P., Timofeev, A. V., House, M. G., Hogg, M. R., Kobayashi, T., Koch, M., Rogge, S., and Simmons, M. Y. Single-Shot Single-Gate rf Spin Readout in Silicon. *Physical Review X 8*, 4 (nov 2018), 041032. 23

[107] Park, S., Metzger, C., Tosi, L., Goffman, M. F., Urbina, C., Pothier, H., and Yeyati, A. L. From Adiabatic to Dispersive Readout of Quantum Circuits. *Physical Review Letters 125*, 7 (aug 2020), 077701. 81, 115

[108] Penfold-Fitch, Z. V., Sfigakis, F., and Buitelaar, M. R. Microwave Spectroscopy of a Carbon Nanotube Charge Qubit. *Physical Review Applied 7*, 5 (may 2017), 054017. 80, 87, 95

[109] Petersson, K. D., McFaul, L. W., Schroer, M. D., Jung, M., Taylor, J. M., Houck, A. A., and Petta, J. R. Circuit quantum electrodynamics with a spin qubit. *Nature 490*, 7420 (oct 2012), 380–383. 5, 21, 24, 56

[110] Petersson, K. D., Smith, C. G., Anderson, D., Atkinson, P., Jones, G. A. C., and Ritchie, D. A. Charge and Spin State Readout of a Double Quantum Dot Coupled to a Resonator. *Nano Letters 10*, 8 (aug 2010), 2789–2793. 24, 80, 81, 87

[111] Petit, L., Eenink, H. G. J., Russ, M., Lawrie, W. I. L., Hendrickx, N. W., Philips, S. G. J., Clarke, J. S., Vandersypen, L. M. K., and Veldhorst, M. Universal quantum logic in hot silicon qubits. *Nature 580*, 7803 (apr 2020), 355–359. 67

[112] Petta, J. R., Johnson, A. C., Taylor, J. M., Laird, E. A., Yacoby, A., Lukin, M. D., Marcus, C. M., Hanson, M. P., and Gossard, A. C. Coherent Manipulation of Coupled Electron Spins in Semiconductor Quantum Dots. *Science 309*, 5744 (sep 2005), 2180–2184. 4, 5, 20

[113] Pla, J. J., Tan, K. Y., Dehollain, J. P., Lim, W. H., Morton, J. J. L., Jamieson, D. N., Dzurak, A. S., and Morello, A. A single-atom electron spin qubit in silicon. *Nature 489*, 7417 (sep 2012), 541–545. 5, 21

[114] Pla, J. J., Tan, K. Y., Dehollain, J. P., Lim, W. H., Morton, J. J. L., Zwanenburg, F. A., Jamieson, D. N., Dzurak, A. S., and Morello, A. High-fidelity readout and control of a nuclear spin qubit in silicon. *Nature 496*, 7445 (apr 2013), 334–338. 4, 102

[115] Reed, M. D., Maune, B. M., Andrews, R. W., Borselli, M. G., Eng, K., Jura, M. P., Kiselev, A. A., Ladd, T. D., Merkel, S. T., Milosavljevic, I., Pritchett, E. J., Rakher, M. T., Ross, R. S., Schmitz, A. E., Smith, A., Wright, J. A., Gyure, M. F., and Hunter, A. T. Reduced Sensitivity to Charge Noise in Semiconductor Spin Qubits via Symmetric Operation. *Physical Review Letters 116*, 11 (mar 2016), 110402. 5

[116] Reilly, D. J. Engineering the quantum-classical interface of solid-state qubits. *npj Quantum Information 1*, 1 (dec 2015), 15011. 23, 24

[117] Reilly, D. J., Marcus, C. M., Hanson, M. P., and Gossard, A. C. Fast single-charge sensing with a rf quantum point contact. *Applied Physics Letters 91*, 16 (oct 2007), 162101. 22, 23, 44, 46

[118] Roschier, L., Hakonen, P., Bladh, K., Delsing, P., Lehnert, K. W., Spietz, L., and Schoelkopf, R. J. Noise performance of the radio-frequency single-electron transistor. *Journal of Applied Physics 95*, 3 (feb 2004), 1274–1286. 23

[119] Scappucci, G., Kloeffel, C., Zwanenburg, F. A., Loss, D., Myronov, M., Zhang, J.-J., De Franceschi, S., Katsaros, G., and Veldhorst, M. The germanium quantum information route. *Nature Reviews Materials* (dec 2020). 5

[120] Scarlino, P., Kawakami, E., Ward, D. R., Savage, D. E., Lagally, M. G., Friesen, M., Coppersmith, S. N., Eriksson, M. A., and Vandersypen, L. M. K. Second-Harmonic Coherent Driving of a Spin Qubit in a Si/SiGe Quantum Dot. *Physical Review Letters 115*, 10 (sep 2015), 106802. 58

[121] Schoelkopf, R. J., Wahlgren, P., Kozhevnikov, A. A., Delsing, P., and Prober, D. E. The Radio-Frequency Single-Electron Transistor (RF-SET): A Fast and Ultrasensitive Electrometer. *Science 280*, 5367 (may 1998), 1238–1242. 21, 22, 23

[122] Schoenfield, J. S., Freeman, B. M., and Jiang, H. Coherent manipulation of valley states at multiple charge configurations of a silicon quantum dot device. *Nature Communications 8*, 1 (dec 2017), 64. 61

[123] Schroer, M. D., Jung, M., Petersson, K. D., and Petta, J. R. Radio Frequency Charge Parity Meter. *Physical Review Letters 109*, 16 (oct 2012), 166804. 55, 56, 81, 116

[124] Schroer, M. D., Petersson, K. D., Jung, M., and Petta, J. R. Field Tuning the g Factor in InAs Nanowire Double Quantum Dots. *Physical Review Letters 107*, 17 (oct 2011), 176811. 21

[125] Shaji, N., Simmons, C. B., Thalakulam, M., Klein, L. J., Qin, H., Luo, H., Savage, D. E., Lagally, M. G., Rimberg, A. J., Joynt, R., Friesen, M., Blick, R. H., Coppersmith, S. N., and Eriksson, M. A. Spin blockade and lifetime-enhanced transport in a few-electron Si/SiGe double quantum dot. *Nature Physics 4*, 7 (jul 2008), 540–544. 20

[126] Shor, P. Algorithms for quantum computation: discrete logarithms and factoring. In *Proceedings 35th Annual Symposium on Foundations of Computer Science* (2002), IEEE Comput. Soc. Press, pp. 124–134. 1

[127] Sillanpää, M. A., Lehtinen, T., Paila, A., Makhlin, Y., Roschier, L., and Hakonen, P. J. Direct Observation of Josephson Capacitance. *Physical Review Letters 95*, 20 (nov 2005), 206806. 80

[128] Stehlik, J., Liu, Y.-Y., Quintana, C. M., Eichler, C., Hartke, T. R., and Petta, J. R. Fast Charge Sensing of a Cavity-Coupled Double Quantum Dot Using a Josephson Parametric Amplifier. *Physical Review Applied 4*, 1 (jul 2015), 014018. 71

[129] Takahashi, S., Deacon, R. S., Oiwa, A., Shibata, K., Hirakawa, K., and Tarucha, S. Electrically tunable three-dimensional g-factor anisotropy in single InAs self-assembled quantum dots. *Physical Review B 87*, 16 (apr 2013), 161302. 21

[130] Thorgrimsson, B., Kim, D., Yang, Y.-C., Smith, L. W., Simmons, C. B., Ward, D. R., Foote, R. H., Corrigan, J., Savage, D. E., Lagally, M. G., Friesen, M., Coppersmith, S. N., and Eriksson, M. A. Extending the coherence of a quantum dot hybrid qubit. *npj Quantum Information 3*, 1 (dec 2017), 32. 5, 61

[131] Urdampilleta, M., Chatterjee, A., Lo, C. C., Kobayashi, T., Mansir, J., Barraud, S., Betz, A. C., Rogge, S., Gonzalez-Zalba, M. F., and Morton, J. J. Charge Dynamics and Spin Blockade in a Hybrid Double Quantum Dot in Silicon. *Physical Review X 5*, 3 (aug 2015), 031024. 81, 87

[132] Urdampilleta, M., Niegemann, D. J., Chanrion, E., Jadot, B., Spence, C., Mortemousque, P.-A., Bäuerle, C., Hutin, L., Bertrand, B., Barraud, S., Maurand, R., Sanquer, M., Jehl, X., De Franceschi, S., Vinet, M., and Meunier, T. Gate-based high fidelity spin readout in a CMOS device. *Nature Nanotechnology 14*, 8 (aug 2019), 737–741. 20, 23

[133] van der Heijden, J., Kobayashi, T., House, M. G., Salfi, J., Barraud, S., Laviéville, R., Simmons, M. Y., and Rogge, S. Readout and control of the spin-orbit states of two coupled acceptor atoms in a silicon transistor. *Science Advances 4*, 12 (dec 2018), eaat9199. 66

[134] van der Wiel, W. G., De Franceschi, S., Elzerman, J. M., Fujisawa, T., Tarucha, S., and Kouwenhoven, L. P. Electron transport through double quantum dots. *Reviews of Modern Physics 75*, 1 (dec 2002), 1–22. 9

[135] Vandersypen, L. M. K., Bluhm, H., Clarke, J. S., Dzurak, A. S., Ishihara, R., Morello, A., Reilly, D. J., Schreiber, L. R., and Veldhorst, M. Interfacing spin qubits in quantum dots and donors—hot, dense, and coherent. *npj Quantum Information 3*, 1 (dec 2017), 34. 5, 67

[136] Veldhorst, M., Eenink, H. G. J., Yang, C. H., and Dzurak, A. S. Silicon CMOS architecture for a spin-based quantum computer. *Nature Communications 8*, 1 (dec 2017), 1766. 5

[137] Veldhorst, M., Hwang, J. C. C., Yang, C. H., Leenstra, A. W., de Ronde, B., Dehollain, J. P., Muhonen, J. T., Hudson, F. E., Itoh, K. M., Morello, A., and Dzurak, A. S. An addressable quantum dot qubit with fault-tolerant control-fidelity. *Nature Nanotechnology 9*, 12 (dec 2014), 981–985. 5, 21

[138] Veldhorst, M., Yang, C. H., Hwang, J. C. C., Huang, W., Dehollain, J. P., Muhonen, J. T., Simmons, S., Laucht, A., Hudson, F. E., Itoh, K. M., Morello, A., and Dzurak, A. S. A two-qubit logic gate in silicon. *Nature 526*, 7573 (oct 2015), 410–414. 5

[139] Venitucci, B., Bourdet, L., Pouzada, D., and Niquet, Y.-M. Electrical manipulation of semiconductor spin qubits within the g-matrix formalism. *Physical Review B 98*, 15 (oct 2018), 155319. 58

[140] Versluis, R., Poletto, S., Khammassi, N., Tarasinski, B., Haider, N., Michalak, D. J., Bruno, A., Bertels, K., and DiCarlo, L. Scalable Quantum Circuit and Control for a Superconducting Surface Code. *Physical Review Applied 8*, 3 (2017), 1–7. 2

[141] Voisin, B., Maurand, R., Barraud, S., Vinet, M., Jehl, X., Sanquer, M., Renard, J., and De Franceschi, S. Electrical Control of g -Factor in a Few-Hole Silicon Nanowire MOSFET. *Nano Letters 16*, 1 (jan 2016), 88–92. 21

[142] Voisin, B., Nguyen, V.-H., Renard, J., Jehl, X., Barraud, S., Triozon, F., Vinet, M., Duchemin, I., Niquet, Y.-m., de Franceschi, S., and Sanquer, M. Few-Electron Edge-State Quantum Dots in a Silicon Nanowire Field-Effect Transistor. *Nano Letters 14*, 4 (apr 2014), 2094–2098. 80

[143] Vukušić, L., Kukučka, J., Watzinger, H., and Katsaros, G. Fast Hole Tunneling Times in Germanium Hut Wires Probed by Single-Shot Reflectometry. *Nano Letters 17*, 9 (sep 2017), 5706–5710. 18, 23

[144] Vukušić, L., Kukučka, J., Watzinger, H., Milem, J. M., Schäffler, F., and Katsaros, G. Single-Shot Readout of Hole Spins in Ge. *Nano Letters 18*, 11 (nov 2018), 7141–7145. 18, 23, 66

[145] Watson, T. F., Philips, S. G. J., Kawakami, E., Ward, D. R., Scarlino, P., Veldhorst, M., Savage, D. E., Lagally, M. G., Friesen, M., Coppersmith, S. N., Eriksson, M. A., and Vandersypen, L. M. K. A programmable two-qubit quantum processor in silicon. *Nature 555*, 7698 (mar 2018), 633–637. 5

[146] Watzinger, H., Kukučka, J., Vukušić, L., Gao, F., Wang, T., Schäffler, F., Zhang, J.-J., and Katsaros, G. A germanium hole spin qubit. *Nature Communications 9*, 1 (dec 2018), 3902. 4, 5, 20

[147] Weber, B., Hsueh, Y.-L., Watson, T. F., Li, R., Hamilton, A. R., Hollenberg, L. C. L., Rahman, R., and Simmons, M. Y. Spin–orbit coupling in silicon for electrons bound to donors. *npj Quantum Information 4*, 1 (dec 2018), 61. 66

[148] West, A., Hensen, B., Jouan, A., Tanttu, T., Yang, C.-H., Rossi, A., Gonzalez-Zalba, M. F., Hudson, F., Morello, A., Reilly, D. J., and Dzu-

rak, A. S. Gate-based single-shot readout of spins in silicon. *Nature Nanotechnology 14*, 5 (may 2019), 437–441. 23

[149] Winkler, R. *Spin-Orbit Coupling Effects in Two-Dimensional Electron and Hole Systems*, vol. 191 of *Springer Tracts in Modern Physics*. Springer Berlin Heidelberg, Berlin, Heidelberg, 2003. 20

[150] Yang, C. H., Leon, R. C. C., Hwang, J. C. C., Saraiva, A., Tanttu, T., Huang, W., Camirand Lemyre, J., Chan, K. W., Tan, K. Y., Hudson, F. E., Itoh, K. M., Morello, A., Pioro-Ladrière, M., Laucht, A., and Dzurak, A. S. Operation of a silicon quantum processor unit cell above one kelvin. *Nature 580*, 7803 (apr 2020), 350–354. 67

[151] Yoneda, J., Otsuka, T., Nakajima, T., Takakura, T., Obata, T., Pioro-Ladrière, M., Lu, H., Palmstrøm, C. J., Gossard, A. C., and Tarucha, S. Fast Electrical Control of Single Electron Spins in Quantum Dots with Vanishing Influence from Nuclear Spins. *Physical Review Letters 113*, 26 (dec 2014), 267601. 20

[152] Yoneda, J., Takeda, K., Otsuka, T., Nakajima, T., Delbecq, M. R., Allison, G., Honda, T., Kodera, T., Oda, S., Hoshi, Y., Usami, N., Itoh, K. M., and Tarucha, S. A quantum-dot spin qubit with coherence limited by charge noise and fidelity higher than 99.9%. *Nature Nanotechnology 13*, 2 (feb 2018), 102–106. 5, 20

[153] Yuan, M., Pan, F., Yang, Z., Gilheart, T. J., Chen, F., Savage, D. E., Lagally, M. G., Eriksson, M. A., and Rimberg, A. J. Si/SiGe quantum dot with superconducting single-electron transistor charge sensor. *Applied Physics Letters 98*, 14 (apr 2011), 142104. 23

[154] Zajac, D. M., Hazard, T. M., Mi, X., Nielsen, E., and Petta, J. R. Scalable Gate Architecture for a One-Dimensional Array of Semiconductor Spin Qubits. *Physical Review Applied 6*, 5 (nov 2016), 054013. 5

[155] Zajac, D. M., Sigillito, A. J., Russ, M., Borjans, F., Taylor, J. M., Burkard, G., and Petta, J. R. Resonantly driven CNOT gate for electron spins. *Science 359*, 6374 (jan 2018), 439–442. 5

[156] Zheng, G., Samkharadze, N., Noordam, M. L., Kalhor, N., Brousse, D., Sammak, A., Scappucci, G., and Vandersypen, L. M. K. Rapid gate-based spin read-out in silicon using an on-chip resonator. *Nature Nanotechnology 14*, 8 (aug 2019), 742–746. 23, 66, 94, 102

[157] Zueco, D., Reuther, G. M., Kohler, S., and Hänggi, P. Qubit-oscillator dynamics in the dispersive regime: Analytical theory beyond the rotating-wave approximation. *Physical Review A 80*, 3 (sep 2009), 033846. 115